Mechanistic Electrochemistry: Investigations of Electrocatalytic Mechanisms for H_2S Detection Applications

Hongkai Ma

Homerton College

Department of Chemical Engineering and Biotechnology

University of Cambridge

November / 2016

This dissertation is submitted for the degree of Doctor of Philosophy

Preface

The work presented in this thesis was carried out in the Department of Chemical Engineering and Biotechnology, University of Cambridge between October 2012 and September 2016. The result in this thesis is my own work and includes nothing which is the outcome of work done in collaboration except where specifically indicated in the text. The work has not previously been submitted for any other degree, diploma or qualification. This thesis contains less than 150 figures and 65,000 words including appendices, references, tables and equations.

Summary

Mechanistic Electrochemistry: Investigations of Electrocatalytic Mechanisms for H_2S Detection Applications

Hongkai Ma

This thesis describes the development of electrochemical analytical approaches for the investigation of sulphide detection in stagnant and fluidic environments. The project reports the use of Fourier transform large amplitude alternating current voltammetry (FTACV) as a novel analytical technique for the investigation of sulphide sensing. Novel reactor technology and FTACV measurements carried out using macro and microelectrodes in stagnant and fluidic conditions are reported for the first time. The novel strategy adopts the use of an electrocatalytic (EC′) mechanism by using a redox mediator to facilitate the reaction with sulphide in aqueous solutions. In order to support the analysis of FTACV, other electrochemical analytical techniques, cyclic voltammetry (CV) and linear sweep voltammetry (LSV), were also employed to support the observations from FTACV.

Chapter 3 reports the application of the CV and FTACV for the detection of sulphide in stagnant conditions at a macroscale electrode. A split wave phenomenon, which is related to the reaction with sulphide, was observed both in the CV and FTACV. By measuring the current behaviour of the split wave, sulphide content in aqueous solution can be determined. Importantly, the split wave phenomenon of the FTACV is the first documented observation using macroscale electrodes. These observations highlight the

potential of FTACV to support the detection of sulphide detection. Numerical models of the system are also presented from the calculation to support the experimental interpretation of the voltammetric responses of the CV and FTACV.

In Chapter 4 measurements were focused on the voltammetric response of sulphide containing aqueous solutions using microelectrodes. In conventional CV measurements, the split wave behaviour observed at macroelectode disappears from the DC signal; however, for the FTACV measurements, the split wave can still be observed in the higher harmonics providing a clear and simple strategy for detecting sulphide. The results achieved in the FTACV are the first documented observation under the steady state at microelectrodes. Again numerical simulations are reported for this case to support the experimental results.

Chapter 5 extends the FTACV measurements for sulphide detection to hydrodynamic environments. The design, development and application of a microfluidic electrochemical system are reported. Split wave characteristics were for the first time detected in both dc and FTACV measurements. The results support the possibility of using dc and ac voltammetry to detect sulphide, while also being used as a guide to assess the split-wave behaviour of the EC′ mechanism under fluidic conditions. Numerical models were used to support the analysis of the experimental measurements.

Acknowledgement

Firstly, I would like to express the deepest gratitude to my supervisor Dr Adrian Fisher, who kindly offers me the opportunity to undertake the PhD project in his group. Without his constant guidance and thoughtful encouragement throughout the research, this thesis would not have been possible. I also thank Viet Nguyen for discussions on numerical modelling presented in this work.

I am extremely grateful to Dr Yunfeng Gu, Dr Kamran Yunus and Dr Jize Yan for their support and guidance. My appreciation also extends to my dearest colleagues, Dr Peng Song, Dr Chencheng Dai, Dr Minyu Zeng, Xiangming Gao, Luwen Meng, Feng Zheng and the other members of CREST group. A very special thank to my friends who accompany me during time in Cambridge, especially Kiteny Chen who helps me with thesis write-up, Ailin Li from Brigham Young University and Yajie Shao who lend me a giant shoulder in difficult times.

Finally, I would like to express my sincerest gratitude to my dearest parents and my relatives, especially my uncle, aunt and my grandparents for their continuous support and inspirations. I love you ~

Abbreviations

Abbreviation	Meaning
AC	Alternating current
CNT	Carbon nanotube
CV	Cyclic voltammetry
CVD	Chemical vapour deposition
DEPD	Diethyl-p-phenylenediamine
E-beam	Electron beam
EC	Heterogeneous electron transfer coupled with homogenous chemical reaction
EC′	Electrocatalytic reaction
FAD	Flavin adenine dinucleotide
FCA	Ferrocene carboxylic acid
FFT	Fast Fourier transformation
FTACV	Fourier transform large amplitude alternating current voltammetry
LIGA	Lithographie, Galvanoformun, and Abformung
LSV	Linear sweep voltammetry
MEMS	Microelectromachanical system
MRIM	Micro reaction injection molding
PDMS	Poly(Dimethylsiloxane)

Pe	Pelect number
PMMA	Poly(methyl methacrylate)
RDE	Rotating disc electrode
RIE	Reactive ion etching
SEM	Scanning electron microscopy
UV	Ultraviolet

Common Symbols

Symbol	Definition	Unit
A	Effective area of electrode	cm^2
C_{dl}	Double-layer capacitance	F
C_o	Concentration of oxidized species	mol L^{-1}
C_R	Concentration of reduced species	mol L^{-1}
C_P	Concentration of product in EC′ process	mol L^{-1}
C_Z	Concentration of substrate in EC′ process	mol L^{-1}
D	Diffusion coefficient	$cm^2\ s^{-1}$
D_O	Diffusion coefficient of oxidant	$cm^2\ s^{-1}$
D_R	Diffusion coefficient of reductant	$cm^2\ s^{-1}$
D_S	Diffusion coefficient of substrate	$cm^2\ s^{-1}$
d	Width of the channel	m
E	Electrode potential	V
E^0	Standard electrode potential	V
E_{dc}	DC voltage	V
E_p	Peak potential	V
ΔE	Potential amplitude of the ac component	V
ΔE_p	Pulse height	V
ΔE_s	Staircase height	V

$E_{\frac{1}{2}}$	Half peak potential	V
f	Frequency	Hz
F	Faraday constant	C mol^{-1}
H	Dimensionless distance	
h	Height of the half-cell device	m
I	Net current	A
I_a	Anodic current	A
I_c	Cathodic current	A
I_p	Peak current	A
i_L	Limiting plateau current	A
k	Rate constant of charge transport	cm s^{-1}
k_{red}	Rate constant of reduced reaction	cm s^{-1}
k_{ox}	Rate constant of oxidative reaction	cm s^{-1}
$K_{EC'}$	Rate constant of EC′ processs	Depends on order
l	Characteristic length	m
n	Number of electrons transferred	
R	Universal gas constant	J K^{-1} mol^{-1}
R_e	Reynolds number	
R_u	Uncompensated resistance	Ω
T	(1) Temperature	K
	(2) Dimensionless time	

t	time	s
u	Ionic mobility	$cm^2\ s^{-1}\ V^{-1}$
v	Velocity of fluid	
v_c	Solution velocity at the centre of the channel	$cm\ s^{-1}$
v_f	Stream velocity	$cm\ s^{-1}$
v_s	Scan rate of the potential sweep	$V\ s^{-1}$
v_x	Velocity of the solution	$cm\ s^{-1}$
w	Length of the electrode	m
X	Dimensionless distance	
x_e	Width of the electrode	m
Y	Dimensionless distance	
y	Distance from the electrode on y axis	cm
α	(1) Charge transfer coefficient	
	(2) Coefficient in the equation set appeared in implicit method	
β	Coefficient in the equation set appeared in implicit method	
γ	Coefficient in the equation set appeared in implicit method	
ω	Angular frequency	$rad\ s^{-1}$
η	Overpotential	V

J	Diffusion flux	
ρ	Density of liquid	kg m^{-3}
μ	Dynamic viscosity	Ns m^{-2}
ϵ	Radius of the macrodisc electrode	cm

Contents

Chapter 1 Introduction

1.1 Introduction

This thesis describes design development and applications of a novel analytical approach used to investigate electrocatalytic reactions. The original approach discussed in this thesis uses a combination of rapid prototyping microfabrication techniques to develop optimised reactor and sensor configurations in combination with advanced electrochemical analysis tools such as the method of Fourier transform large amplitude alternating current voltammetry (FTACV). The aim of this developed approach is to focus on the analysis of sulphide containing substrates which are technologically important in industries such as oil extraction and biogas analysis. In the following chapter, a review of the background on electrochemistry will be given. Chapter 2 will follow with an introduction to rapid prototyping microfabrication techniques and methods applied for the development of reactors used to achieve the results presented in later chapters.

1.2 Introduction to electrochemistry

The work described in this thesis dissects advanced microengineering techniques used to develop highly sensitive and mechanistically discriminating tools used for analysis and chemical conversion applications. L. Alting and colleagues presented the view that microengineering can be used to focus on the development and the manufacture of products while enjoying a high level of integration of functional components with sizes, of at least one dimension, in the order of μm[1]. In this context, for these technologies,

microengineering is incorporated into the entire processing chain: material preparation[2], device fabrication[3, 4] and operating procedures[5].

In the electrochemical research field, microengineering is regularly used for design and fabrication of electrode or reactor structures with dimensions on the micron to submicron scale. The high precision and flexibility of fabrication techniques allows for the integration of many different functional components on a single device. The "lab-on-a-chip" or total analysis systems can offer significant benefits over more traditional macroscale reactors or sensors, which is supported by a rapidly growing body of literature studying the development of this technology[6-8].

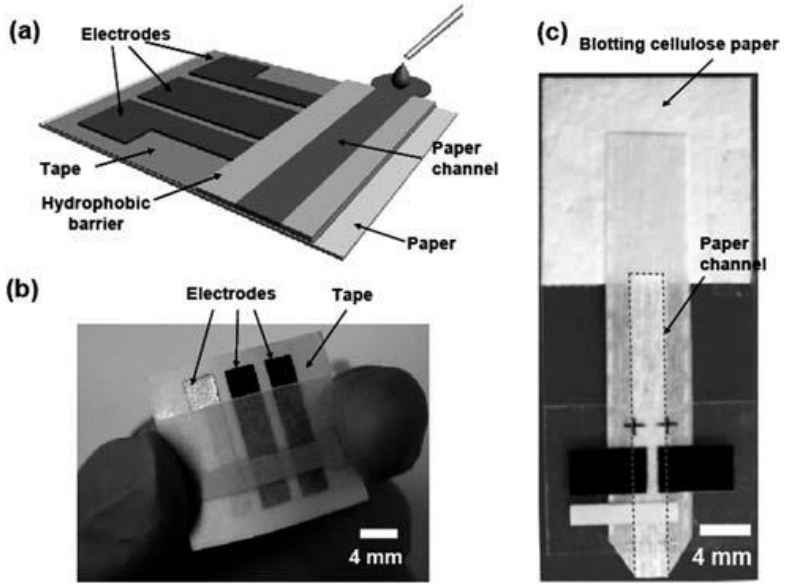

Figure 1.1 Schematic of a electrochemical sensing device[9].

In the area of chemical analysis and chemical conversions, scientific advancements have led to reactors that can be optimised for surface area to volume ratio, rapid acquisition time and reduced sample requirements[10-12]. In the electrochemical field, the adoption of microengineering techniques has led to widespread innovation in

analysis, electrosynthesis and energy storage/conversion technologies. For example, energy harvesters unite a broad range of techniques that can be used to capture energy from light, heat, mechanical processes and even acoustic waves. Captured energy sources can then be transformed into electricity where it can be stored and eventually used as batteries to support low-power devices[13-15]. As such, energy harvesting technology is often integrated within a larger scale network, where microengineered sensors can be used to monitor and control specific aspects of a network. Likewise, these and other microengineered monitoring approaches can also be electrochemical in nature[9]. Therefore, to explore the potential sensitivity and design of an electrochemical monitor, the fundamental aspects of electrochemistry will be reviewed in the following sections.

1.2.1 Electron transfer at an electrode

In electrochemical redox reactions, an electron transfer process occurs at the solid-liquid interface. A single electron transfer process can be described as:

$$O + e^- \rightleftharpoons R \tag{1.1}$$

where O and R are oxidized and reduced forms, respectively, of an electroactive species in the system. Charge transport across the interface between the electrode and electrolyte must overcome an energy barrier. Once at equilibrium the relationship between electrode potential and bulk concentration can be predicted using the Nernst equation:

$$E = E^0 + \frac{RT}{nF} ln(\frac{C_O^*}{C_R^*}) \tag{1.2}$$

where E^0 is the standard potential of the redox couple (V); R is the universal gas constant with value 8.314 $J{\cdot}K^{-1}{\cdot}mol^{-1}$; T is the temperature (K); $C_O{}^*$ and $C_R{}^*$ are concentrations of oxidized and reduced species in bulk solution, respectively. In the

case of a dynamic equilibrium, even though the reduction of O and the oxidation of R are occurring in the electrolyte, no net current flows through the cell and the overall concentration of the chemical species does not vary with time. However, if a potential is applied to the system, which is different from that of the equilibrium value, the concentration ratio of O and R at the electrode surface will attempt to adjust in order to match values predicted by equation (1.2). During this process, an oxidative or reductive current will flow as part of the overall reaction.

Current generated by electron transfer at any potential is related to the kinetics and can be predicted using

$$I = I_c + I_a \tag{1.3}$$

where I_c and I_a are cathodic (forward) and anodic (backward) currents, respectively, which are each only determined by the concentration of the redox couple at the electrode surface and rate constant:

$$I_c = -nFAk_cC_O \tag{1.4}$$

$$I_a = nFAk_aC_R \tag{1.5}$$

where n is the number of electrons transferred; F is the Faraday constant (96485 C/mol); A is the effective area of the electrode (cm^2); k_c and k_a are rate constants of charge transport; C_O and C_R are concentrations of electroactive species in oxidized and reduced forms, respectively, on the electrode surface. It can be the case that the diffusion rate (or known as transport rate) of a species from bulk to the electrode surface is smaller than the consumption rate of reactant involved in the reaction, a concentration difference between O and R in the vicinity of the electrode occurs.

The rate constant k for an electrochemical reaction varies as a function of the applied potential in an exponential manner:

$$k_c = k_{c,0}\, exp(-\frac{\alpha_c nF}{RT} E) \tag{1.6}$$

$$k_a = k_{a,0}\, exp(\frac{\alpha_a nF}{RT} E) \tag{1.7}$$

where α_c and α_a are transfer coefficients for reductive and oxidative current, respectively. The sum of α_c and α_a equals 1 for a simple reaction.

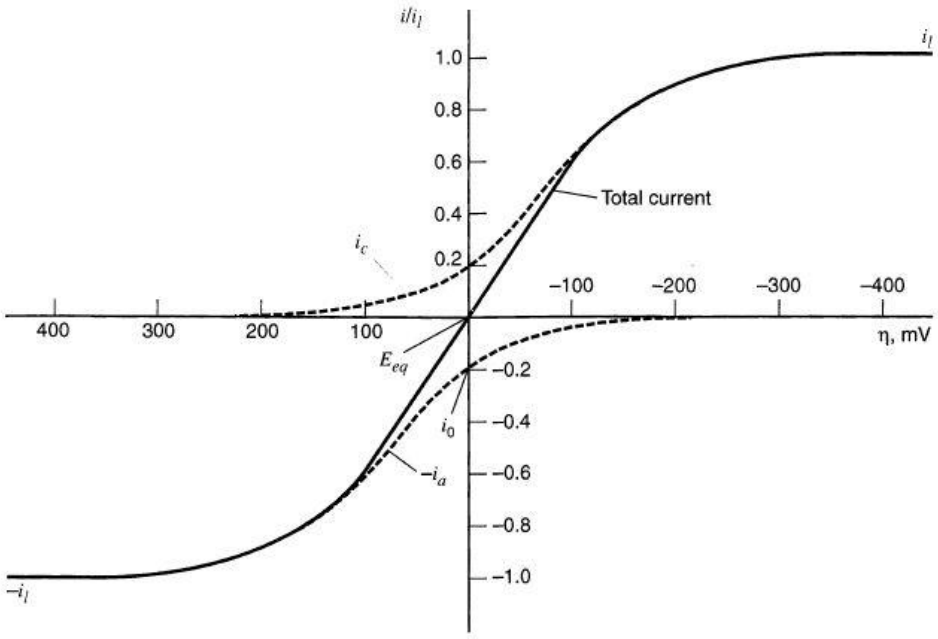

Figure 1.2 The effect of overpotential on the behaviour of current flow[16].

To understand the relationship of potential deviation from the equilibrium potential, namely overpotential η, with current[16, 17], the Butler-Volmer equation can be applied:

$$I = I_0[(\frac{C_O(0)}{C_O(\infty)})exp\left(\frac{\alpha_c nF\eta}{RT}\right) - (\frac{C_R(0)}{C_R(\infty)})exp\left(\frac{\alpha_a nF\eta}{RT}\right)] \tag{1.8}$$

where I_0 is the standard exchange current. Taken from the Butler-Volmer equation, current density is dependent on the variation of exchange current I_0, overpotential η, the concentration of bulk solution and transfer coefficients. When I_0 is large, electroactive species behave as a reversible process as both forward and backward currents flow with minimal overpotential. In contrast, for small I_0, this is referred to as

an irreversible system and requires a large overpotential to drive the reaction. Figure 1.2 depicts the effect of overpotential on the behaviour of current flow. If negative overpotential is large enough, the current behaves as I_c due to the decreased effect of anodic components. By contrast, for a large positive overpotential, the current will be the same as I_a.

1.2.2 Mass transfer

When the rate of electron transfer is very large, the current response will often be controlled by the transport of reactants to the electrode surface. The general modes of mass transport can be categorized as diffusion, convection and migration.

1.2.2.1 Diffusion

Consumption of reactants at the electrode surface leads to generation of a concentration gradient close to the surface of the electrode, a region referred to as the diffusion layer. Diffusion, is caused by a difference in concentration[18] and can be quantitatively predicted using Fick's first law:

$$J = -D\left(\frac{\partial C}{\partial x}\right) \tag{1.9}$$

where, J is the diffusive flux, D is the diffusion coefficient (cm^2/s); C is concentration (mol/cm^3) and x is a one-dimensional Cartesian co-ordinate (cm). Fick's first law demonstrates that flux moves from a position of high to low concentration. The rate of diffusion at a certain position is determined by the concentration gradient at that point. The concentration of reactant varies as the reaction occurs, which is determined as a function of time. In this instance, it is important to understand how concentration of a species changes with time:

$$\frac{\partial C}{\partial t} = D\left(\frac{\partial^2 C}{\partial x^2}\right) + D\left(\frac{\partial^2 C}{\partial y^2}\right) + D\left(\frac{\partial^2 C}{\partial z^2}\right) \quad (1.10)$$

This is Fick's second law written in three-dimensional form.

1.2.2.2 Convection

Convection is induced by external forces in the solution and can occur in two forms. The first form is natural convection, which appears in any solution, resulting from thermal gradients and differences in density. Effects of convection are related to time and electrode size. For an electrode whose size is larger than the order of millimetres, convection in the solution becomes significant on the timescale of 10 s or longer. This type of perturbation is undesirable due to its unpredictability.

The second form is forced convection, which is driven by mechanical forces, such as pressure-driven forces[19] (pumping or draining), gas bubbling[20] and stirring[21]. Forced convection, such as microfluidic or a rocking motion is deliberately introduced into a system to minimize effects of natural convection and to ensure reproducibility of experimental results when the timescale is greater than 10 to 20 s. In most instances, forced convection is controlled so that it is well defined and can be predicted either mathematically or numerically for the reactor geometry. For cases of convective limitation, variation of concentration resulting from the flow of solution can be given by:

$$\frac{\partial C}{\partial t} = -V_x \frac{\partial C}{\partial x} \quad (1.11)$$

where V_x is velocity of solution. In the following chapters, forced convection is applied to assist in better understanding the electrochemical mechanism.

1.2.2.3 Migration

The potential drop at a solid–liquid interface results in the presence of an external electric field ($\frac{\partial \varphi}{\partial \mathrm{x}}$). Charged species in the solution are driven by electrostatic forces in the interfacial region, which induces ion migration. The contribution of migration effects leads to the transport of species during the electrochemical reaction where migratory flux (j_m) demonstrates direct proportional relationship with ionic mobility, u, the concentration of ions in solution, C and strength of the electric field, as follows:

$$j_m \propto -uC\frac{\partial \varphi}{\partial x} \tag{1.12}$$

Parameters such as viscosity of solution, ionic charge and magnitude, can affect the mobility of ions in solution.

When a supporting electrolyte composed of non-electroactive ions with an excess concentration is added to an electroactive system, effects of migration can be eliminated. However, electron transfer in the system is not influenced by presence of the supporting electrolyte. The introduction of a supporting electrolyte also acts to enhance conductivity of the solution.

1.2.3 Introduction to voltammetry

Voltammetric methods are widely used in electrochemistry for analysis and mechanistic studies of redox reactions. In a typical voltammetric measurement, the external potential difference is varied as a function of time with the current response of the system measured as a function of time and/or voltage. Voltammetric measurements are generally carried out using a three-electrode system, which includes a working electrode, a reference electrode and a counter electrode[16]. Different forms of

voltammetry used for measurements in this thesis are introduced in the following section.

1.2.3.1 Potential step chronoamperometry

In potential step voltammetry, the signal input is in the form of *E*-*t* and the output form is *i*-*t*. Illustrated in Figure 1.3 (a), when potential is applied there is an instantaneous step from E_1, where no electrochemical reaction is occurring, to E_2, where reactant O in the vicinity of the electrode has completely transformed to R.

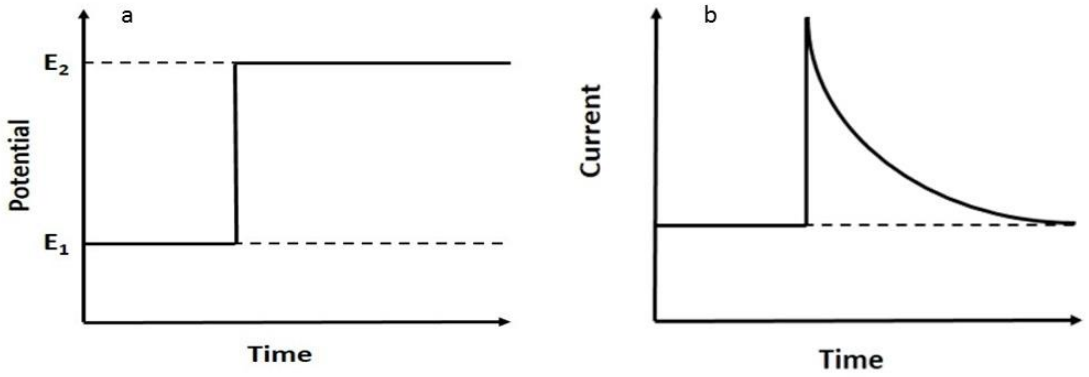

Figure 1.3 (a) Signal input of potential step voltammetry and (b) current-time output of potential step voltammetry.

A large current is detected when potential jumps and the magnitude of the current decreases with time. Current behaviour is dependent on diffusion rate of the reactant moving from the bulk to the electrode surface. In the instance of a reversible electron transfer reaction, current flow can be predicted using the Cottrell equation[22, 23]:

$$i = nFAC_O\sqrt{\frac{D}{\pi t}} \tag{1.13}$$

where C_0 is the concentration of reactant bulk solution and the current response is depicted in Figure 1.3 (b).

1.2.3.2 Linear sweep voltammetry

Linear sweep and closely related cyclic voltammetry are common techniques used to study the performance of electron transfer and mass transport in electrochemical systems[24, 25]. In linear sweep voltammetry, the potential is swept at a fixed scan rate between two values, E_1 and E_2:

$$E(t) = E_1 - v_s t \tag{1.14}$$

where v_s is scan rate of the potential sweep.

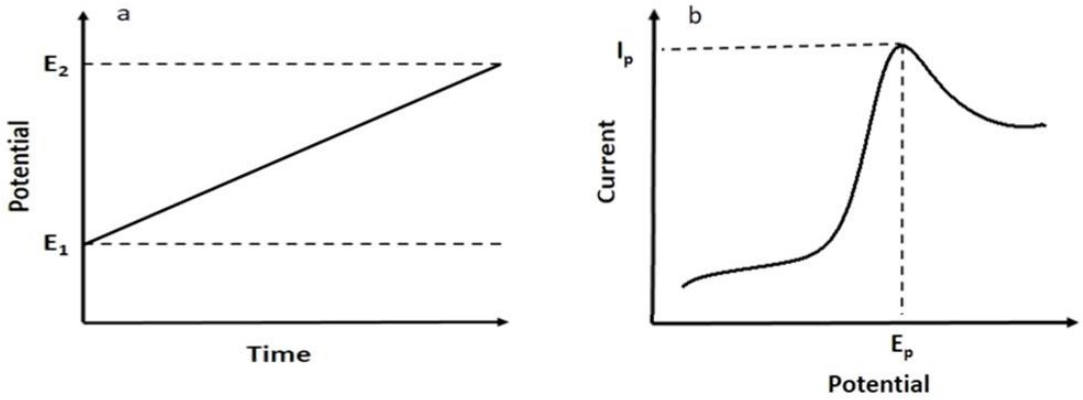

Figure 1.4 (a) Signal input of LSV and (b) the corresponding linear sweep voltammogram.

In the instance of a reversible reaction, electron transfer rate demonstrates a large magnitude and current behaviour is completely controlled by mass transfer in solution. As the potential is swept in a negative direction, the concentration of O and R in the vicinity of the electrode is kept in equilibrium. According to the Nernst equation, peak current I_p appears when the flux of fresh O is not fast enough to be transported to the electrode surface due to growing thickness of the diffusion layer. When peak potential E_p is reached, concentration of O at the electrode surface is largely depleted. Peak potential of the reversible reaction is constant:

$$\left|E_p - E_{\frac{p}{2}}\right| = 2.2\frac{RT}{F} \tag{1.15}$$

However, peak current, I_p, is dependent on scan rate (v_s) and reactant concentration in solution:

$$\left|I_p\right| = 0.4463\, nAFC_{bulk}\left(\frac{nFv_s D_A}{RT}\right)^{\frac{1}{2}} \tag{1.16}$$

This is the Randles-Sevcik equation[26, 27] and is commonly used in studies. The value of peak current varies in a linear relationship with the square root of the scan rate. The increased scan rate leads to a thinner diffusion layer and higher flux of species to the electrode surface.

1.2.3.3 Cyclic voltammetry

When potential is swept from E_1 to E_2 and then reversed, the signal input is a triangle potential cycle against time (illustrated in Figure 1.5) and the technique is called cyclic voltammetry (CV). The CV can be considered as an extended form of LSV, which is generally applied to characterize electrochemical performance of reaction processes, fabricated devices or modified electrodes[28, 29]. While the current of the forward scan is identical to that obtained in LSV, the reduced species R is oxidized back to O when the potential sweeps back to E_1. For an ideal reversible reaction, peak current height for reductive ($I_{p,c}$) and oxidative processes ($I_{p,a}$) should be identical[27]:

$$\frac{|I_{p,c}|}{|I_{p,a}|} = 1 \tag{1.17}$$

Separation of peak potentials only related to the temperature and number of electrons transferred in the reversible reaction:

$$\left|E_{p,c} - E_{p,a}\right| = 2.218\frac{RT}{nF} \tag{1.18}$$

The separation potential that is independent of scan rate is 59 mV/*n* when temperature is 25 °C. If the reaction is irreversible or quasi-reversible, the value will be larger and changes with scan rate.

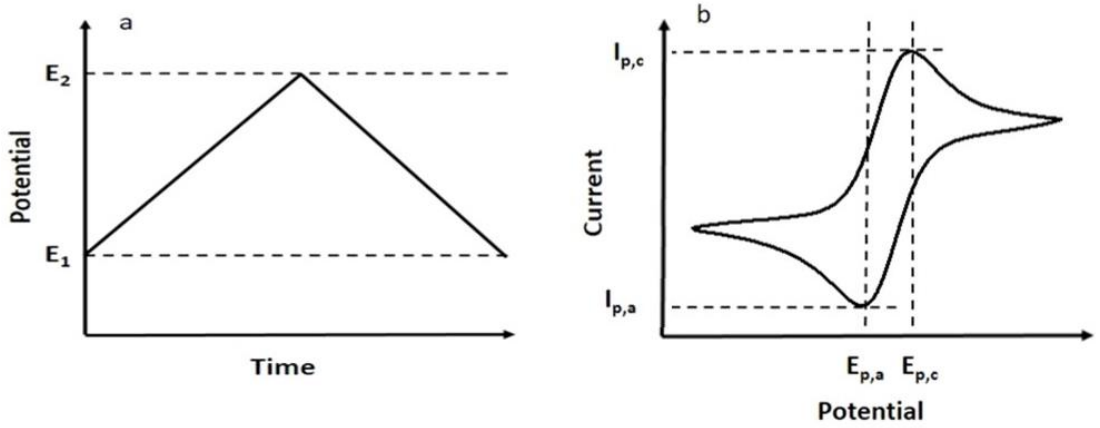

Figure 1.5 (a) Signal input of CV and (b) the corresponding cyclic voltammograms.

Half-wave potential $E_{1/2}$, related to the thermodynamic formal potential of a reaction, is also an important parameter when studying the properties of these processes[30, 31]:

$$E_{\frac{1}{2}} = \frac{E_{p,c}+E_{p,a}}{2} \tag{1.19}$$

$$E_{\frac{1}{2}} = E + \frac{RT}{nF} In(\frac{D_R}{D_O})^{\frac{1}{2}} \tag{1.20}$$

DC voltammetry has been widely used due to its ease for analysis. In some circumstances, it cannot meet the requirements to detect complicated electrochemical reactions and accurately determine the potential. To solve this problem, a perturbation is added to the dc input signal, which has been proven to enhance sensitivity in determination of the potential. The most commonly used technique is square-wave voltammetry.

1.2.3.4 Square wave voltammetry

Square wave voltammetry is a large-amplitude differential technique and is widely used in the analysis of electrode materials, biochemical systems and chemical detection[32]. This method was first reported by G. C. Barker and I. L. Jenkins in 1952 as an advanced technique demonstrating robust sensitivity down to 10^{-7} M[33, 34]. Currently, development and optimization recognize square wave voltammetry is a popular analysis approach, which enjoys the advantages of background suppression, high sensitivity, the capability of obtaining diagnostic, direct analysis of products and a wide range of time scales[16, 35].

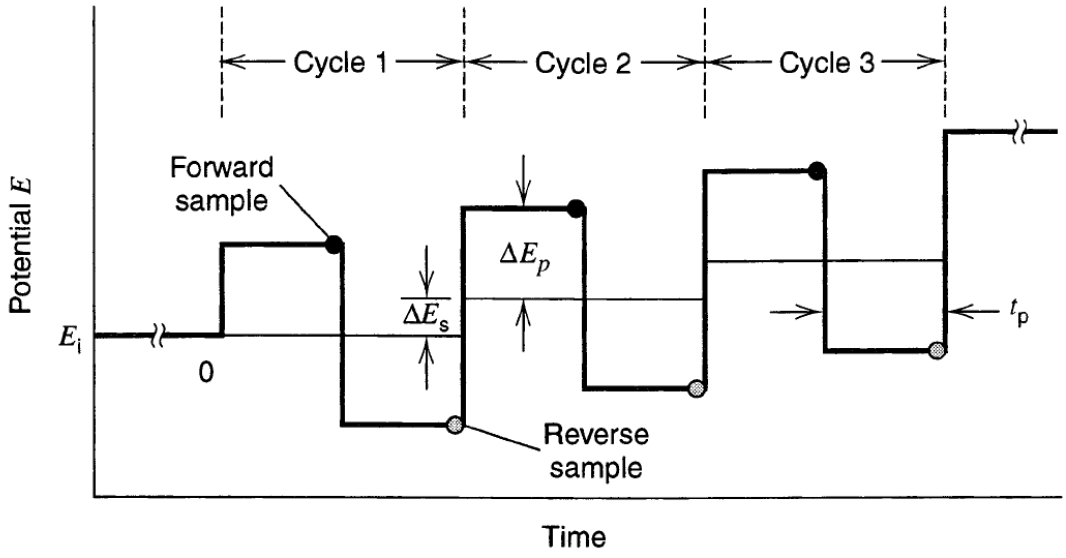

Figure 1.6 Waveform of square wave voltammetry[16].

Figure 1.6 illustrates a symmetrical square wave potential superimposed on a staircase potential. The signal input has an amplitude, ΔE_p, step height, ΔE_s and step width in time, t_p. For this model, frequency (f) and scan rate (v) of the square wave can be described using:

$$f = 1/2t_p \tag{1.21}$$

$$v = \Delta E_s/2t_p = f\Delta E_s \tag{1.22}$$

During an experiment, magnitude of the time scale and potential step are separately determined by t_p and ΔE_s. Current responses for forward and reverse scans can be recognized as I_f and I_r, respectively with the difference between the two written as ΔI. The current of each pulse can be calculated using the equation[36]:

$$i = \frac{nFAD^{\frac{1}{2}}C}{\sqrt{\pi t_p}}\psi(\Delta E_s, \Delta E_p) \tag{1.23}$$

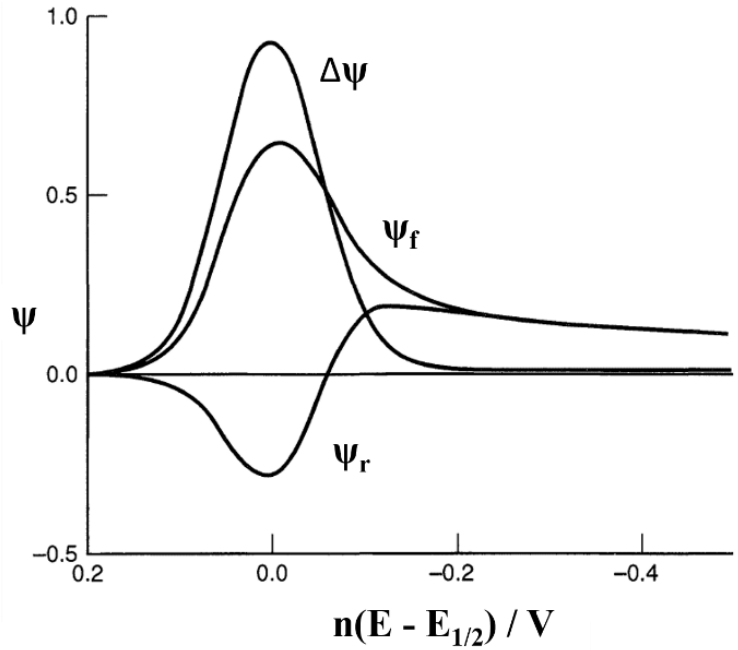

Figure 1.7 Normalized response of square wave voltammogram consists of forward (ψ_f), reverse (ψ_r) and net ($\Delta\psi$) components[16].

where C is the bulk concentration of reactant; ψ is the dimensionless current function determined by step height ΔE_s and amplitude ΔE_p. Current demonstrates a linear relationship with concentration and the square root of frequency. In Figure 1.7, the current response of the forward, reverse and the difference are plotted against voltage. When current difference approaches a maximum, potential is $E_{1/2}$, which is an important parameter in the characterisation of the electrode reaction.

1.2.3.5 Fourier transform large amplitude alternating current voltammetry (FTACV)

To understand the electrode mechanism while separating the faradaic and non-faradaic terms, various voltammetric techniques have been developed, which use a sinusoidally varying potential input, in combination with a linear potential ramp[37, 38].

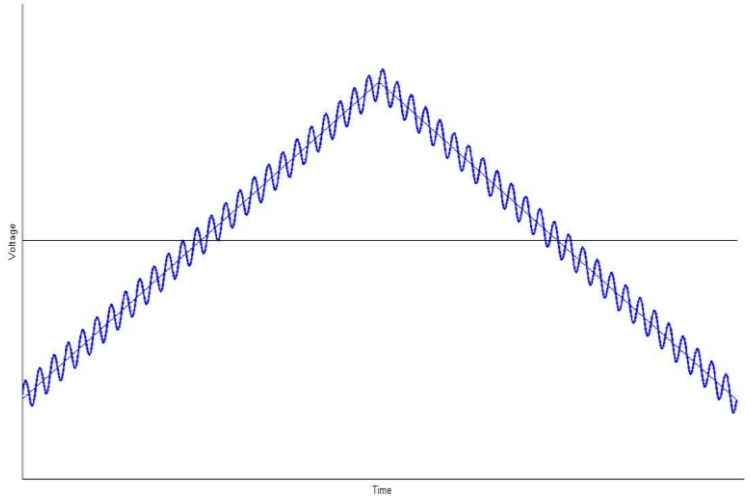

Figure 1.8 Signal input of FTACV.

In the FTACV, signal input is composed of a sinusoidal and dc waveform. Traditionally, in electrochemical impedance measurements, the ac component is introduced as a small-amplitude sine perturbation (with ΔE of 5-10 mV) demonstrating a frequency ranging from 10 Hz to 1000 Hz or higher[39]. Figure 1.8 illustrates signal input in voltage-time and can be described as:

$$E_t = E_{dc} + \Delta E sin(\omega t) \quad (1.24)$$

where E_{dc} is dc voltage; ΔE is amplitude of the ac component; ω is angular frequency. In this approach, phase and magnitude of the current response is measured in the first harmonic.

Alan Bond and his colleagues have presented theoretical treatments for the application of a FTACV approach with ΔE 50-200 mV and the signal response analysed as a Fourier transform inverse Fourier transform sequence[40-42]. The signal input of FTACV in equation 1.24 can be presented with more detail as the angular frequency and amplitude, combined by harmonic components as:

$$E_t = E_{dc} + \sum_{n=1,2,3\ldots}^{N} \Delta E_n \sin(\omega_n t) \quad (1.25)$$

The use of a Fourier series allows the periodic function to be decomposed into a linear combination of harmonic signals. The output response consists of a dc contribution and ac components, which are the fundamental (at ω), second (at 2ω), third (at 3ω) and higher harmonics[40].

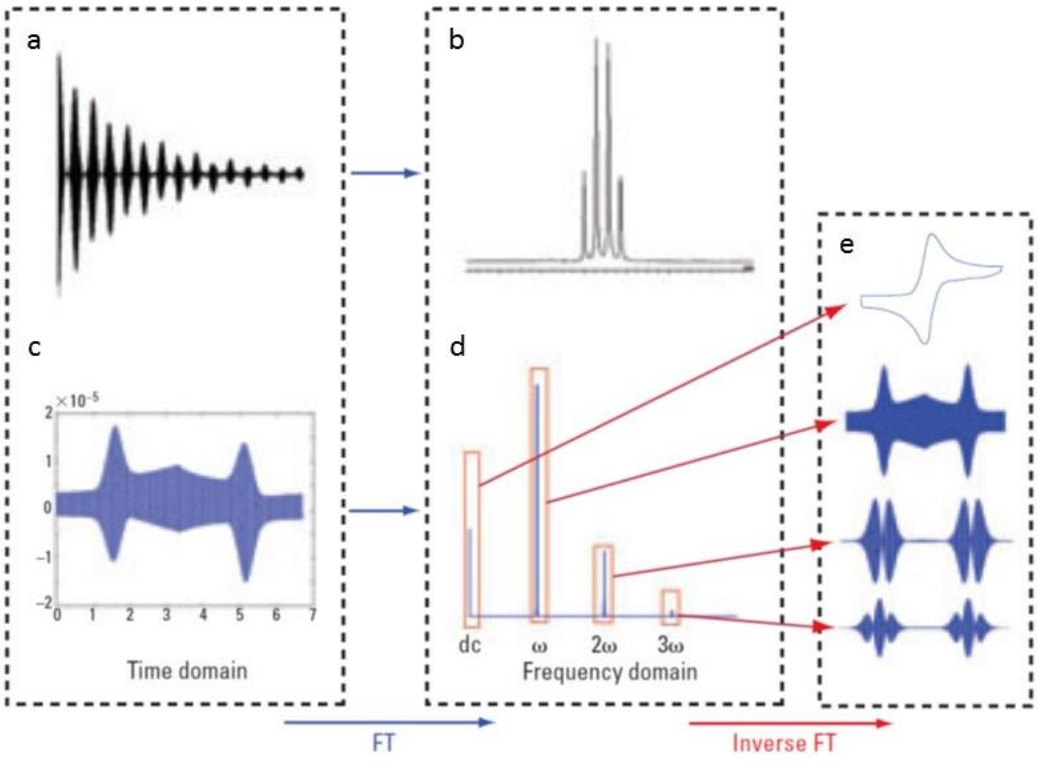

Figure 1.9 Transformation of raw data to time–current form result by the fast Fourier transform algorithm. (a) and (c) time dependent raw results; (b) and (d) periodical frequency–current result obtained by Fourier transform; (e) ready-for-analysis separated dc and harmonic components after inverse Fourier transform treatment[37].

Separation of faradaic from non-faradaic components is achieved using the Fourier transform algorithm. Because in theory, the double-layer capacitive component C_{dl}, will demonstrate a different phase and magnitude relationship to the input signal than that for example, of a charge transfer process. By varying amplitude and frequency, it is possible to extract information about different aspects of a charge transfer reaction[43, 44]. Additionally, second and higher harmonic terms are essentially free from effects of the double-layer charging current so that these higher harmonics can be used to study factors such as coupled chemical or charge transfer processes, which are free from capacitive complications. The influence of uncompensated resistance (R_u) is another factor that should be considered. The existence of R_u undoubtedly affects the manner of both faradaic and non-faradaic contributions. In the FTACV, the second-order faradaic term can be sensitive to R_u and therefore a small variation of potential drop caused by IR_u can be detected in all harmonic components[45, 46]. Because the sensitivity of IR_u is related to the faradaic component of the current, which is determined by the concentration of electroactive reactants, experiments with a series of different concentrations of reactants are usually performed to evaluate effects caused by IR_u.

To obtain dc and harmonic components in FTACV, a certain frequency band containing most of the energy is selected to filter the excluded portion in the power spectrum. Each component demonstrates a unique frequency, which is 0 Hz for dc, $\frac{\omega}{2\pi}$ for the fundamental harmonic, $\frac{\omega}{\pi}$ for the second harmonic and so on. Consider the data processing, the power spectrum at the selected frequencies is treated by an inverse Fourier transform algorithm and the components induced by the dc and the ac signal are generated in a current–time version. As the double-layer charging component is only present in dc and fundamental components, the behaviour of the pure kinetic terms in the second and higher harmonic components can be readily analysed[47].

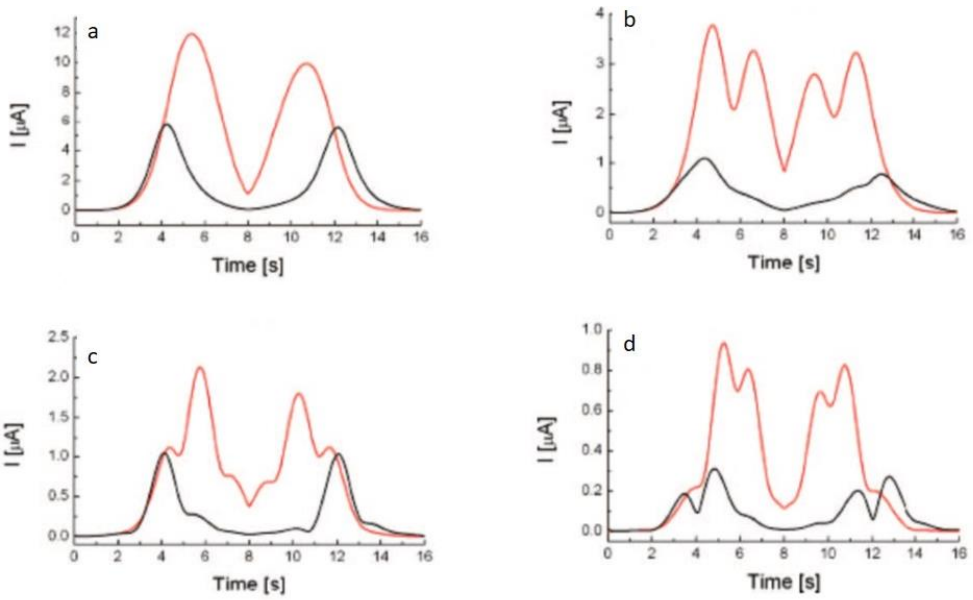

Figure 1.10 (a) First, (b) second, (c) third and (d) fourth ac harmonic component of quasi-reversible reaction in the absence (black) and presence (red) of catalytic reaction[48].

In a reversible system, the rate of electron transfer is fast enough and the reaction is under diffusion control. For the dc component, a classic duck-shape curve in current–time or current-voltage form, which is identical to the result of CV, is separated. When looking at the ac components, in Figure 1.9, a bell-shaped curve can be identified in the fundamental component, which is not varied by scan rate, amplitude or frequency. A single current peak can be found on a forward scan when $E_{dc} = E_{1/2}$, which is near the standard potential of the redox species. Ideally, the curve of the reverse scan should retrace closely over the forward curve. Effects of the capacitive background can be detected at the baseline. For the second harmonic, two symmetrical peaks are obtained in both forward and backward scans. The middle point of the two peaks is $E_{1/2}$. As such, Bond and colleagues have built up a simulation model to predict the R_u of the system in the second harmonic component due to its sensitivity[49, 50]. They demermined height and the shape of the peaks are good indications of reversibility. Three peaks with the middle one higher than those adjacent are obtained in the third harmonic. Theoretically, the three peaks should be symmetrical about the line of $x = E_{1/2}$ with height of the forward peaks equalling to those of the backward curves. For the fourth

and higher harmonic components, behaviour of the peaks provides qualitative information. By incorporating simulation models, abundant quantitative results can be obtained.

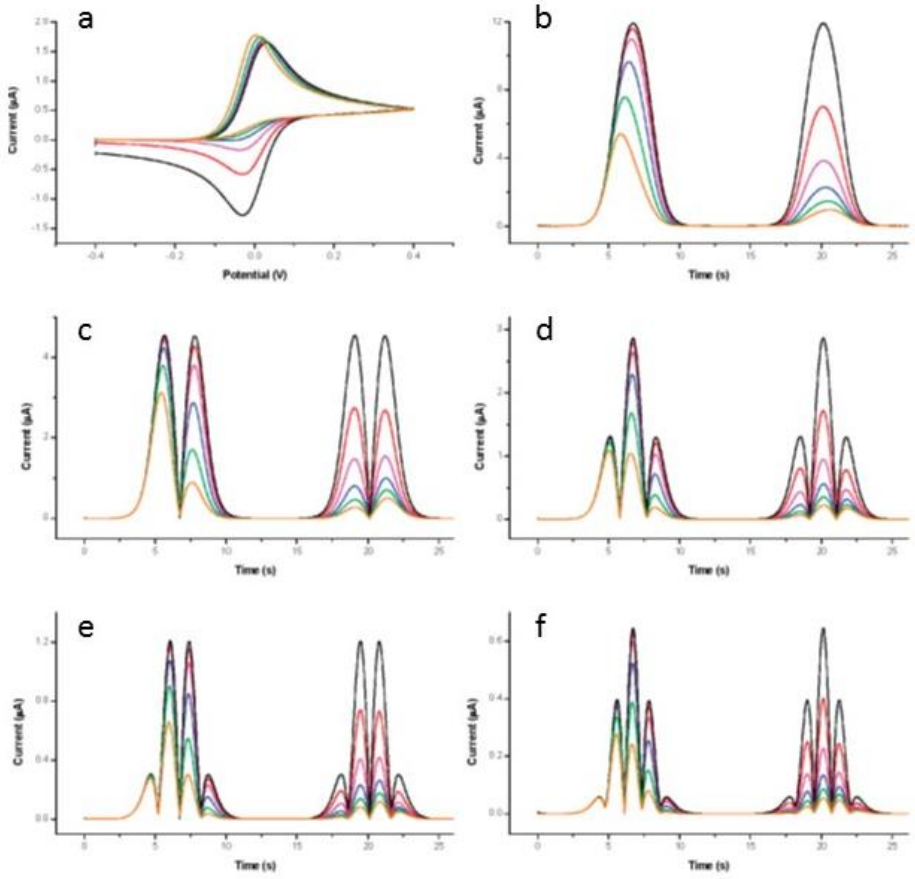

Figure 1.11 Simulated results of (a) dc, (b) first, (c) second, (d) third, (e) fourth and (f) fifth harmonic component of electrochemical chemical reaction with kinetic rate of charge transfer 0 (black), 0.1 (red), 0.32 (magenta), 1.0 (blue), 3.2 (green) and 10 s^{-1} (orange)[51].

When the rate of charge transfer decreases, behaviour of the ac components will vary correspondingly(Figure 1.10)[52]. In the fundamental component, current peaks of forward and backward reactions demonstrate different heights. Peak position will vary depending on frequency and scan rate, which agrees with results taken from dc voltammetry. For the second harmonic component, peak height of the two peaks in the

same scan will be different due to the competition of kinetic control and diffusion control. Asymmetry of peaks can also be observed in the third and fourth harmonic components.

Application of FTACV has also extended into studies of a heterogeneous reaction coupled with a homogeneous chemical reaction[51]. As Figure 1.11 shows, stronger effects of a chemical reaction on the system lead to a peak decrease at both the forward and backward scan in all harmonics. This phenomenon is consistent with dc results. However, $E_{1/2}$ as a property of electroactive species does not vary and can be easily obtained using the value of the second harmonic component. Notably, the value of $E_{1/2}$ using FTACV is easier to be achieved than when using the dc approach. Additional discussion will be provided in subsequent chapters. The non-linear voltammetric technique provides a ready access to information-rich and fast detection. It has proven value in applications of biochemistry, new materials[53] and fundamental electrochemical studies[54].

1.2.4 Selectivity of electrochemical detection

In a practical application, electrochemical detectors are required to analyse complex mixtures, in which case they should show a high selectivity to minimise interference from other chemicals. The dc voltammetric technique can provide reasonable selectivity by controlling the proper potential range. In some circumstances, however, chemicals that have a close electroactive potential or react with the target chemical will affect the results. In this case, improvements are necessary to increase the selectivity of the electrochemical sensors. The selectivity can be enhanced by three approaches: (a) increasing the selectivity of the membrane using ion-selective electrodes, (b) increasing the selectivity of the electrode via modification of the electrode surface, (c) increasing the selectivity of the voltammetric technique.

Ion-selective electrodes were developed in the 20th century and many different types have been developed for commercialization. Glass electrodes are among the most widely used solid-state membrane electrodes and a schematic is shown in Figure 1.12. During the measurement, the thin glass membrane should be fully immersed in the test solution. When the membrane is selectively permeable to a single species, an electrode potential difference can be measured and responds in a Nernst-like relationship to the ion's activity in the solution. Based on the ion selectivity, the commercialised glass electrodes can be divided into three types: proton-sensitive electrodes, sodium-sensitive electrodes and cation-sensitive electrodes. For the other solid-state membrane electrodes, such as AgCl, LaF_3, Ag_2S, CuS, the structure is similar to that of glass electrodes[16]. The membrane can selectively adsorb the species in the bulk electrolyte and the chemicals can be detected. The Ag_2S membrane, for example, can selectively accommodate S^{2-} and an insoluble precipitate is formed. By measuring the potential difference, the S^{2-} concentration can be determined[55].

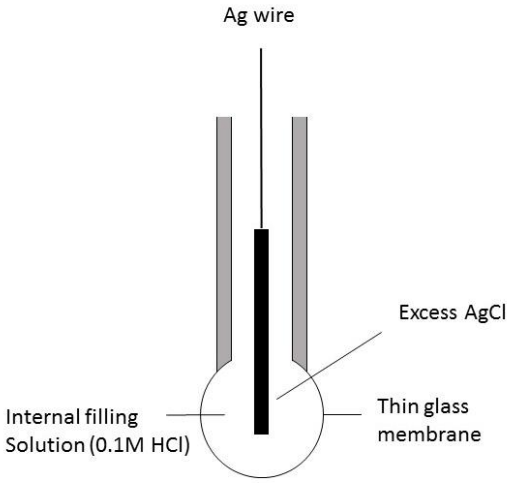

Figure 1.12 Schematic of a typical glass electrode

Modification of the electrode surface is also a common approach to detect chemicals selectively. For the attached material, its stability on the electrode surface and reactivity towards the target chemicals are the two main concerns. Ideally, the electrodes should have high reactivity with the target chemicals and be inactive towards other compounds.

When considering its application in sulphide detection, detecting material with factors of good reversibility, fast kinetics in reacting with sulphide and fast regeneration even at low potential are important[56]. Ferrocene and its derivatives are the most commonly used mediators, which meet the above requirements well. Electrodes screen printed with ferrocyanide ion containing gel have been reported to detect sulphide compounds successfully in the presence of other anions[57]. Electrodes modified by ferrocenecarboxylic acid have also been reported as having a linear relationship with the sulphide concentration and can be used to determine the sulphide concentration quantitively in solution[56].

As detailed in the previous section, the dc voltammetric technique can distinguish chemicals by potential range. However, its selectivity is limited to chemicals that have greatly different electrochemical properties and are not affected by each other. These two factors limit its application in industrial analysis. To solve these problems, the improvement by superimposing a large-amplitude sinusoidal signal is introduced. As introduced in section 1.2.3.5, the faradaic signal is distributed to the fundamental and higher harmonic components; the capacitive signal, however, is present at the fundamental components only. Therefore, the enhancement of signal-to-noise ratio can be achieved at higher harmonic components. Moreover, each electroactive reaction has a unique 'fingerprint' phase angle to the frequency spectrum[58]. By adjusting the voltammetric parameters, a favourable selectivity can be achieved if the phase angle difference of the interfering chemical and target chemical is close to 90°[59]. Kuhr's group has reported the selective detection of glucose and maltose due to the difference of phase angle at high harmonic components, and sensitivity of the sinusoidal ac voltammetry is down to nM[60]. By employing the nature of the 'fingerprint' phase angle of redox couples, large-amplitude sinusoidal voltammetry has been used to selectively detect chemical mixtures with similar electrochemical properties, such as ferrocene derivatives[59], oligonucleotides and DNA[61]. Moreover, large-amplitude sinusoidal voltammetry can also combine with capillary electrophoresis and

microfluidic devices to enhance its selectivity in the detection of carbohydrates[62-64]. To support the experimental results, Bond's group has developed a complete numerical model of large-amplitude alternating current voltammetry to estimate qualitatively and quantitatively the distribution of the power spectrum in the frequency domain, which fits various electrochemical systems[44, 65].

1.3 Coupled chemical and electrolysis reactions

With the exception of a simple electron transfer processes, an electrochemical reaction is also likely to be complicated by other heterogeneous or homogeneous chemical reactions. The following section will provide examples.

1.3.1 Chemical electrolysis (CE) reaction

In the following case, a preceding chemical reaction occurs in advance of the electrolysis reaction and generates the electroactive reactant O as follows:

$$Z \rightarrow O \qquad C \text{ step}$$

$$O + e^{-} \rightleftharpoons R \qquad E \text{ step}$$

Initially, the concentration of O is zero. The electrochemical behaviour is determined by electron transfer and the mass transport that are not only controlled by the electroactive process but also related to the kinetics of the C step. The CE mechanism commonly exists in systems of weak acids, reduction processes involving metal complexes and organic substances.

1.3.2 Electrolysis chemical (EC) reaction

In the EC reaction, the chemically induced processes occur following an initial electrolysis step:

$$O + e^- \rightleftharpoons R \qquad \text{E step}$$

$$R \xrightarrow{k_{EC}} Z \qquad \text{C step}$$

The product R, generated in the E step, is unstable in the system and transformed to Z with a rate constant of k_{EC}. If the rate of the chemical reaction is large, species R will be consumed in the homogeneous reaction as soon as it is formed in the vicinity of the electrode.

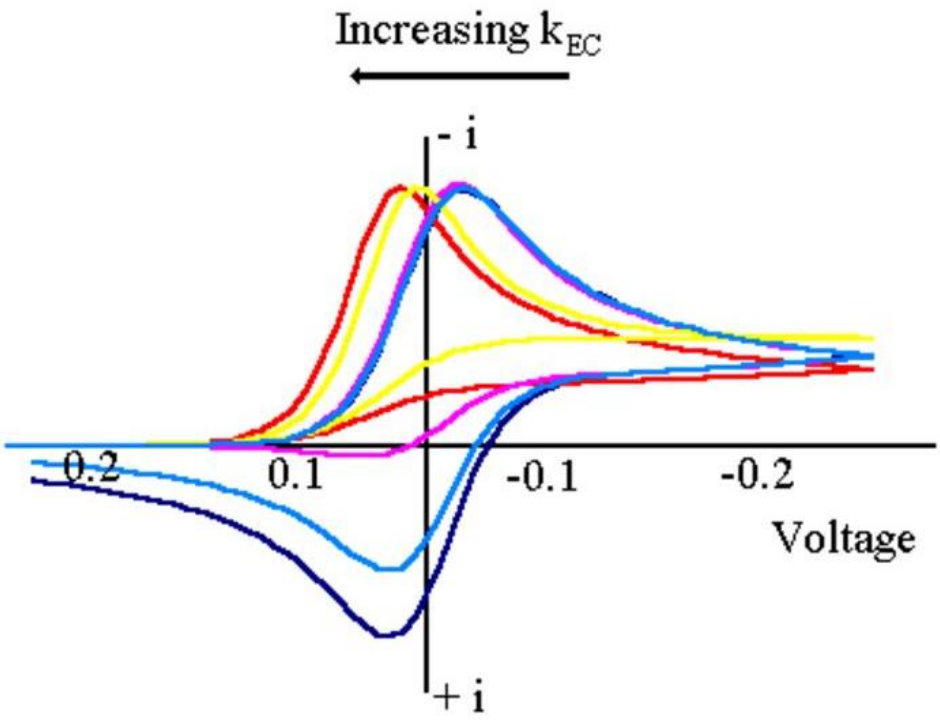

Figure 1.13 Cyclic voltammograms of the EC reaction with increasing kinetics k_{EC} of homogeneous reactions from small (navy) to large value (red).

As illustrated in Figure 1.13, behaviour of the forward peak by CV is similar to that of a reversible reaction. When the potential is swept back from E_2 to E_1, current curves

differ as the kinetic value varies. The re-oxidation process from R to O is reduced as the electroactive species R is involved in the C step. The magnitude of current loss is dependent on the rate constant of the chemical reaction and the speed of the potential sweep. When considering the kinetics for a k_{EC} with small value, the rate of R decaying is slower whereby a larger amount of R is ready to be transformed to O. In this instance, the current curve of the backward scan presents a peak and little difference from stable CVs is detected. As such, when k_{EC} is increased, the peak of the backward scan decays. However, once k_{EC} reaches above a certain value, all R is consumed by the chemical reaction and no peak can be observed on the reverse scan consistent with the scan marked in yellow. Another phenomenon related with reaction rate is the shift of peak potential. As k_{EC} increases, the current curve shifts to the oxidation direction and it will be easier for reduction of O (Figure 1.13). This phenomenon can be clarified using the Nernst equation (equation 1.2). The introduction of a homogeneous chemical reaction disrupts the original equilibrium by removing generated R leading to the establishment of a new equilibrium benefiting the production of R. As a result, a peak shift can be observed in the voltammogram. The stability of R in the system is reflected by the height of the reverse curve, which leads to the possibility of being able to estimate the reaction rate.

1.3.3 Electro catalytic (EC′) reaction

The EC′ reaction consists of an electron transfer step and catalytic chemical reaction, where the prime (′) indicates a catalytic process, as follows:

$$O + e^- \rightleftharpoons R \qquad \text{E step}$$

$$R + Y \xrightarrow{k_{EC'}} Z + O \qquad \text{C′ step}$$

The generated R in the electrochemical step is involved in a catalytic chemical, (C′) process. The catalytic reaction of R and substrate Y results in the regeneration of

electroactive species O, which is in turn involved in the electrochemical reaction. As a result, a current enhancement can be detected. Figure 1.14 illustrates current behaviour of various concentrations of substrate by CV. The blue line is a pure reversible reaction without substrate. The regenerated O from the homogeneous chemical reaction is reduced to R at the electrode and induces extra current flow. The backward peak decays as the amount of substrate increases due to consumption of R in the catalytic reaction. Theoretically, current enhancement is determined by the concentration of substrate in the solution and the rate constant $k_{EC'}$.

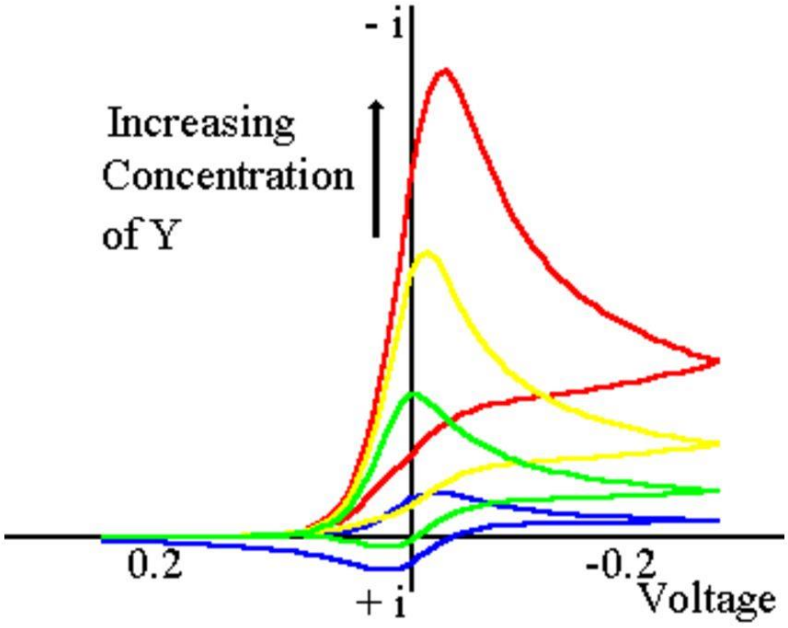

Figure 1.14 Cyclic voltammograms of the EC′ reaction with increasing concentration of substrate from small (navy) to large value (red).

Current response of the reversible electrochemical reaction obtained by CV is defined by the electron transfer rate and mass transport. The Nernst equation can be applied when the electron transfer is fast enough. The ratio of O and R alters with the change of applied potential. A current peak can be observed determined by the mass transfer of the catalytic species to the electrode surface. Effects of non-electroactive substrates introduce other possibility. For the pure kinetic reaction combined with substrate

consumption, competition between the kinetics of the catalytic step and the diffusion of substrate on the electrode results in the peak shape in CV. When the catalytic species is completely consumed by substrate on the electrode, the reduction peak in the reverse scan disappears[66]. As concentration of substrate decreases, a split wave can be observed once the initial concentration of reactant O is close to the concentration of the substrate and the reaction rate of the homogeneous reaction ($k_{EC'}$) is over a certain value[67]. The first peak is related to the catalytic process, whereas the split peak becomes more obvious with an increase of $k_{EC'}$. This highly complex reaction is the focus of the following experimental chapters and the application of advanced ac methods to investigate redox behavior of systems.

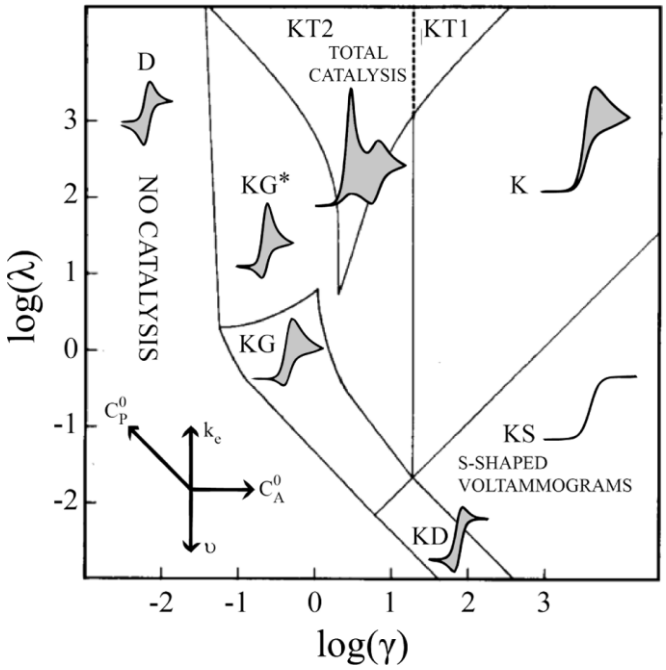

Figure 1.15 Simulated cyclic voltammograms of the EC′ reaction in kinetic zones where λ is the kinetic parameter and γ is the excess factor. Zone D (no catalysis), KG and KG* (electrolysis with slow catalysis), KT (electrolysis with fast catalysis), KD (slow rate of catalysis with excess of substrate), K (fast rate of catalysis with excess of substrate) and KS (excess of substrate)[66].

Figure 1.15 demonstrates variations of current behaviour according to substrate, scan rate and kinetics. A well-defined duck-shape curve is obtained when the reversible

reaction occurs on the electrode illustrated in zone D. A reverse peak, which is determined by the oxidation of R, decays when substrate is added into solution. For a system with large $k_{EC'}$, substrate is immediately consumed by the mediator once it diffuses to the electrode surface from the bulk. A pre-peak that corresponds with the catalytic reaction is observed, as zone KT is presented. However, if the rate of the chemical reaction is small, the reaction will enter zone KG. Catalysis of L-cysteine by ferricyanide-ferrocyanide couple is a typical KG reaction[68]. Reactions in both zone KG and KT will enter zone K when the concentration of substrate is large enough or upon lowering the concentration of redox species in order to decrease the ratio of substrate to mediator. When the catalytic species is completely consumed, this leads to disappearance of the reverse peak[66].

The EC′ mechanism has been examined in a number of different environments and applications because of advantages listed below[69, 70]:

- The enhanced current generated from the electrocatalytic reaction can be exploited to improve sensitivity of electro-detection with numerous electrochemical sensors[71, 72].
- An electroactive couple in the 'E' step can be used as a selective mediator to assist detection of non-electroactive substances. In this instance, the electrochemical response of the redox couple is studied as a function of the non-electroactive substrate ('Z') through calculations or calibration. This will allow for specific sensing devices to be developed[73, 74].
- Other than analytical detection, energy conversion is another important application of the EC′ mechanism (such as flow batteries)[72, 75, 76].

The EC′ mechanism has been widely used to study the detection of sulphide species. High toxicity of liberated hydrogen sulphide leads to physiological suffering in low concentrations and can cause fatal sickness in high concentrations[77]. Even though

high reactivity of sulphide species in aquatic systems has decreased in environmental accumulation and risk levels[78], quantification of sulphide using monitoring technologies is important, particularly for those regularly exposed to sulphide, such as drilling and refining of crude oil. In comparison with conventional detection routes, such as spectroscopic technology and chromatography, electrochemical detection devices stand out because of low price, simplicity of design and high sensitivity[79]. Development of electrodes[77, 80, 81] and redox mediators for electrocatalysts[78, 79, 82] has been widely discussed. Carbon materials, such as fullerene, carbon nanotubes and graphene along with their derivatives have been widely studied and accepted as efficient materials for electrocatalytic sensors, for both chemical and medical fields[72, 83]. Variation of current signal can be used for characterization. Kinetic rate of electron transfer among molecules is determined by controlling the concentration of non-electroactive substances. Additional detail on this topic will be provided in Chapter 3.

1.4 Types of electrodes

1.4.1 Microelectrodes

Microelectrodes, are recognized to possess one or more dimensions on the scale of 50μm or below. This small-scale characteristic leads to significant advantages for electrochemical analysis applications over macroscopic or larger scale electrode geometries. The small size leads to enhanced mass transport effects, small double-layer capacitance effects and small ohmic loss in comparison to larger scale electrodes[84].

For instances of mass transport related phenomena, the underlying physical reason for this can be understood from the scale of the depletion layer (e.g. diffusion layer

thickness) surrounding an electrode during an analysis measurement, which in the case of a microelectrode is large in comparison to electrode size. As shown in Figure 1.16, during a voltammetry measurement movement of species from the bulk solution to a macroelectrode surface is essentially perpendicular. For a microelectrode, the edge effect plays an important role as the depletion layer around the electrode is significant relative to the size of the microelectrode[85-87].

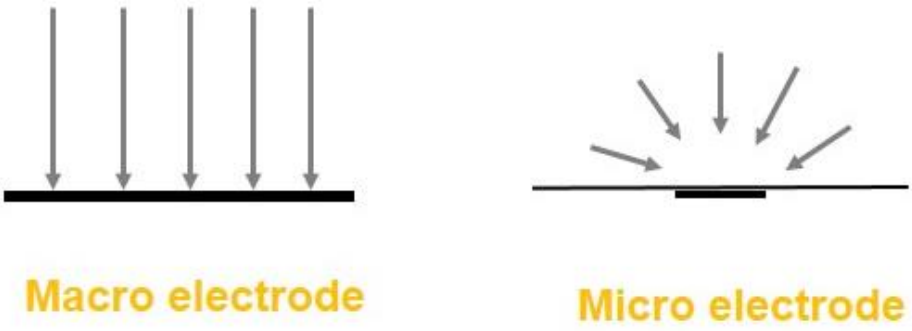

Figure 1.16 Diffusion behaviour on the surface of macroelectrode and microelectrode.

The edge effect and transport characteristics of the microelectrode can be depend on geometric shapes of an electrode. Figure 1.17 illustrates mass transfer characteristics of different microelectrode geometries. For the micro-disc and micro-band electrodes, diffusion in the vicinity of the electrode arrives from two dimensions leading to an enhancement in current at edges of electrodes. Enhanced mass transport allows for the presence of steady-state current when potential scan rate is slow enough. A micro-disc, such as metal wire or carbon fibre that is sealed in a glass insulator, is the most common type[16]. Current behaviour at other electrode geometries such as spherical, cylindrical, ring-shaped and band microelectrodes have also been reported both experimentally and computationally[16, 88-90].

The double layer characteristics of an electrode are related to the overall area of the electrode surface. For a microelectrode system, overall area is dramatically smaller than that of a macroscopic electrode leading to largely reduced capacitance at

microelectrodes. Additionally, the time constant associated with the interface is also considerably smaller than that of macroelectrodes[91]:

$$t_c = \frac{\triangle E}{R}\, e^{-\frac{t}{RC}} \tag{1.26}$$

Thus, when size of an electrode decreases, the magnitude of RC is reduced, which leads to shorter charging time in the system and allowing more rapid voltage scan rates to be used during electrochemical measurements.

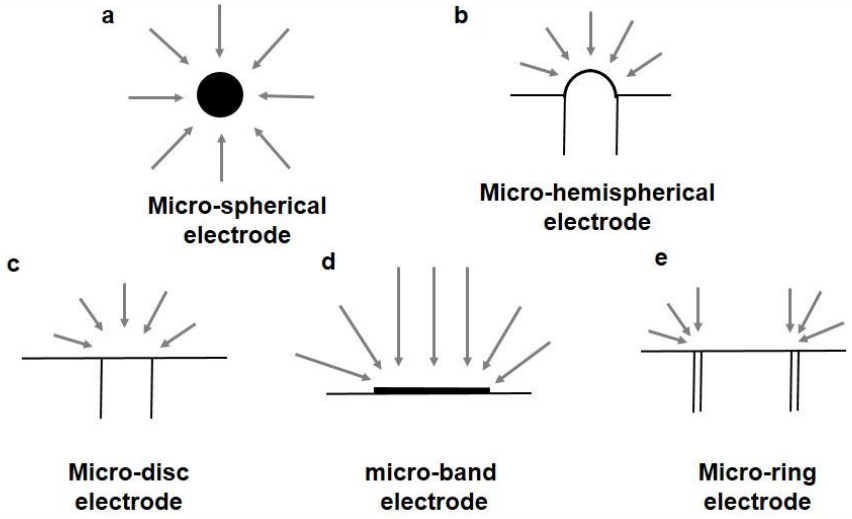

Figure 1.17 Diffusion flux on microelectrodes with different shapes.

1.4.2 Hydrodynamic electrodes

In a hydrodynamic system, typical forced convection is deliberately introduced into the cell in a well-defined manner in order to enhance transport rates to the electrode surface. This also has the added benefit of ensuring fresh reagent is continually supplied to the electrode region. As a consequence, the rate of reaction near the electrode can be changed by controlling convection rate of the solution. Two main approaches are used to introduce convection into an electrochemical cell. The first uses a fixed electrode and the electrolyte is forced to flow over the surface[92]. The second approach is the

well-defined movement of an electrode (e.g. via rotation) to introduce forced convection[93]. Various hydrodynamic electrodes will be introduced in the following sections.

1.4.2.1 Rotating disc

The rotating disc electrode (RDE) is a most commonly used hydrodynamic electrode, which has been applied to study complex redox reactions. A metallic or carbon-based disc electrode embedded in an insulated cylindrical rod is rotated at an arte to induce a well-defined flow pattern close to the electrode surface. Figure 1.18 illustrates electrolyte flow characteristics towards the RDE surface due to the presence of a diffusion gradient.

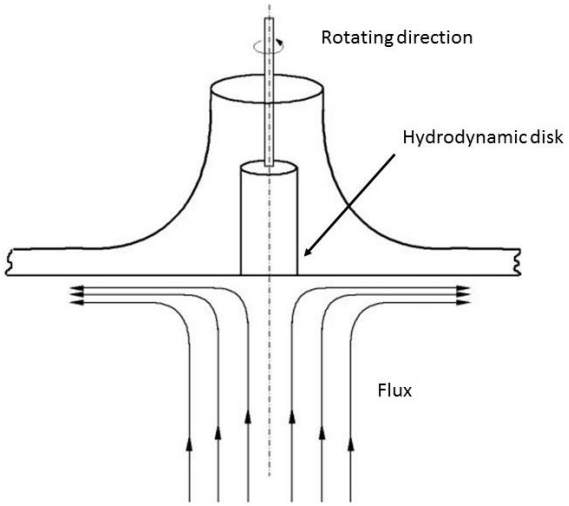

Figure 1.18 Behaviour of solution on the RDE surface[94].

The speed of rotation is typically controlled to ensure laminar flow is established close to the electrode surface, so that behaviour can be mathematically predicted. In this system, mass transport can be predicted by:

$$\frac{\partial[\mathrm{C}]}{\partial \mathrm{t}} = D_C \frac{\partial^2[C]}{\partial x^2} - V_x \frac{\partial[C]}{\partial x} \tag{1.27}$$

where *x* is distance to the electrode surface. In these flowing systems, it is possible to establish a steady state "diffusion layer" around the electrode region leading to the measurement of voltammetric curves which are time invariant (assuming a low enough voltage sweep rate is employed). Additionally, because current is now influenced by the rotation rate and because mass transport is a limited process, Levich[95] first reported the variation of the limiting current for a reversible reaction:

$$i_L = 0.62nFACD^{\frac{2}{3}}v^{-\frac{1}{6}}\omega^{\frac{1}{2}} \tag{1.28}$$

where *v* is kinematic viscosity. Based on equation 1.28, it can be determined that the limiting current demonstrates a linear relationship with the square root of rotation speed.

1.4.2.2 Wall jet electrode

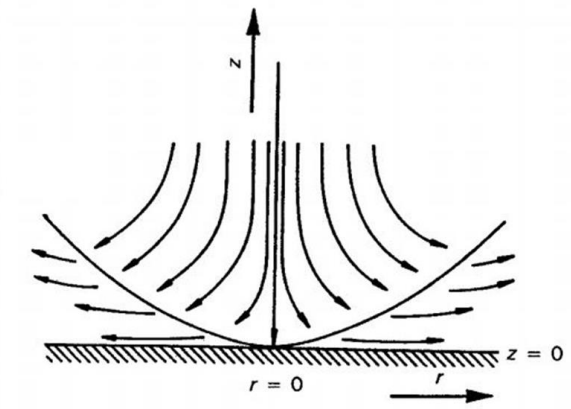

Figure 1.19 Behaviour of flow on wall-jet electrode[96].

In the wall jet electrode, a fluid is propelled onto a planer electrode[97], in instances where the electrode is much larger than the jet. As fluid impinges onto the electrode surface, the liquid spreads out radially, which leads to a characteristic dependence of the current as a function of fluid flow rate. In this geometry and under laminar flow conditions the current density is highest at the centre of the electrode and falls as radius

increases[98]. The wall jet has been used for online detection and a broad range of mechanistic and analytical applications[96, 99].

1.4.3 Micro hydrodynamic electrode

1.4.3.1 Microjet electrode

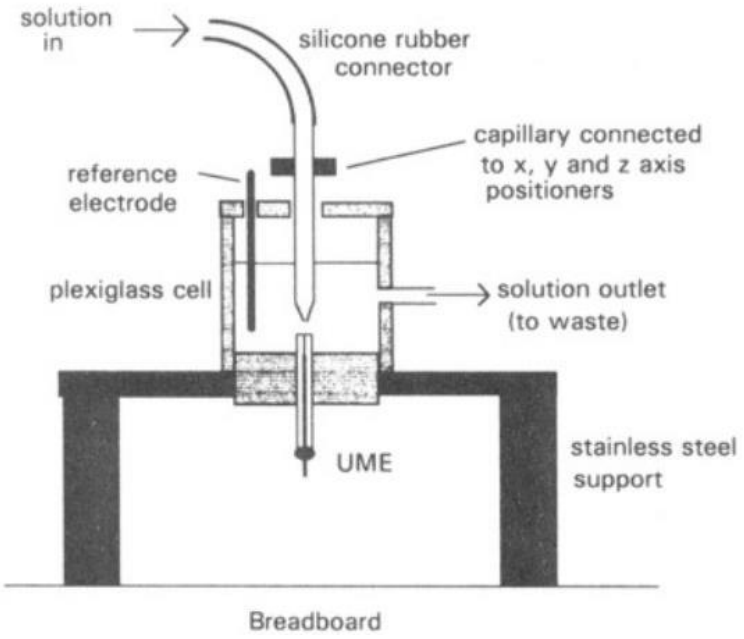

Figure 1.20 Schematic of microjet electrode[100].

The microjet electrode is similar to wall jet geometry. However, the jet in the microjet electrode is larger than the size of the electrode, which is typically a microelectrode. Figure 1.20 shows a schematic of a microjet electrode. The diameter of the nozzle is in the range 25-100 μm and the electrode size is commonly 25 μm in diameter. A jet of electrolyte is fired onto the electrode surface from a capillary with high velocity. In comparison to the diffusion only system, the value of mass transport rate by applying a microjet electrode increases by up to two orders of magnitude[100, 101]. By controlling

the rate of nozzle oscillation that is parallel to the electrode, the behaviour of mass transport, involving convection and diffusion, can be well defined[102, 103]. The microjet electrode has demonstrated value in the studies of electrochemical kinetics, such as heterogeneous electron transfer and homogeneous reactions, by applying steady-state voltammetry. Measurement accuracy can be up to 10^{-9} M[102].

1.4.3.2 Microfluidic channel flow systems

The channel electrode is a hydrodynamic system where the electrode is a fixed and the electrolyte is forced to flow through a rectangular duct and over an electrode embedded in one wall of the reactor. Figure 1.21 presents the flux in the micro-channels and the structure of micro-channel devices.

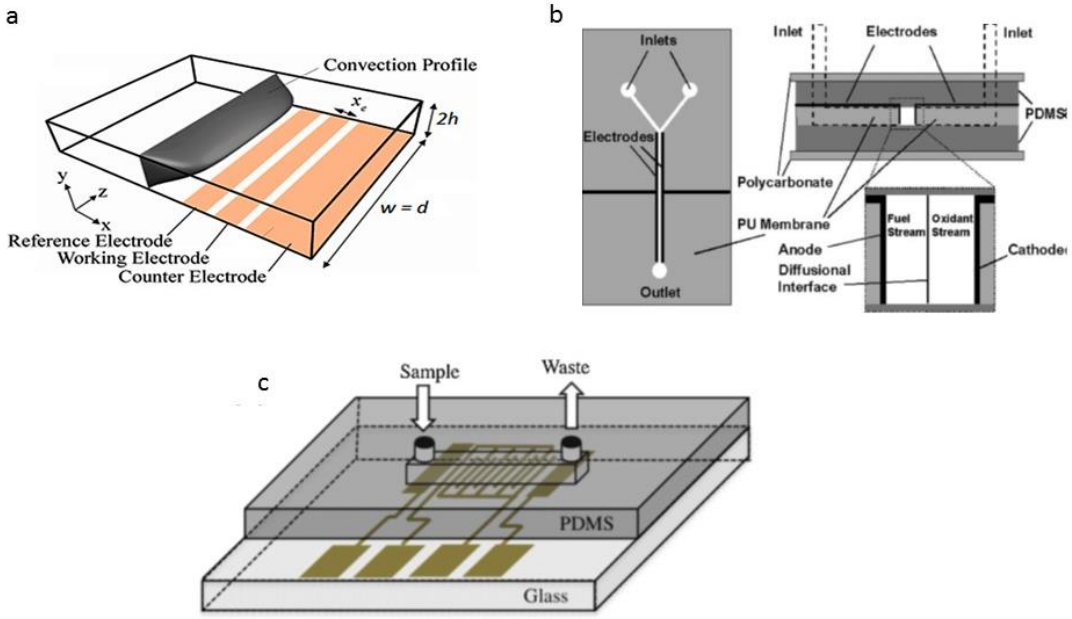

Figure 1.21 Schematic illustration of hydrodynamic channel electrode: (a) flux of laminar flow in the channel; (b) Y-shape of fluidic device; (c) fluidic devices with gold electrodes[104-106].

The flow is typically parabolic in nature under laminar flow conditions whereby flow stability can be predicted using the Reynolds number for geometry [107]:

$$R_e = \frac{v\, l\, \rho}{\mu} \tag{1.29}$$

This device can be used with either large scale (macro) or smaller microelectrodes[108]. The application of microchannel electrodes can be used to cover chemical detection, monitoring of cell behaviour and fuel cells[105, 109]. For voltammetric measurements, the mass transport limited current is (i_L), and under laminar flow can be predicted to vary as a function of the cube root of the volumetric flow rate [104, 106, 110, 111]:

$$i_L = 0.925nFC_bD^{\frac{2}{3}}v_f^{\frac{1}{3}}h^{-\frac{2}{3}}d_d^{-\frac{1}{3}}wx_e^{\frac{2}{3}} \tag{1.28}$$

where n is the number of electrons transferred in the reaction; C_b is the bulk concentration of redox species; D is the diffusion coefficient; v_f is the volumetric flow rate; h is the height of the half-cell device; d is the width of the channel and w is the length of the electrode. Figure 1.22 illustrates the electrochemical behaviour of a reversible couple at various volume flow rates recorded using linear sweep voltammetry In this thesis, these types of microfluidic devices are used to investigate electrochemical mechanisms and specifically explore the catalytic decomposition of sulphide.

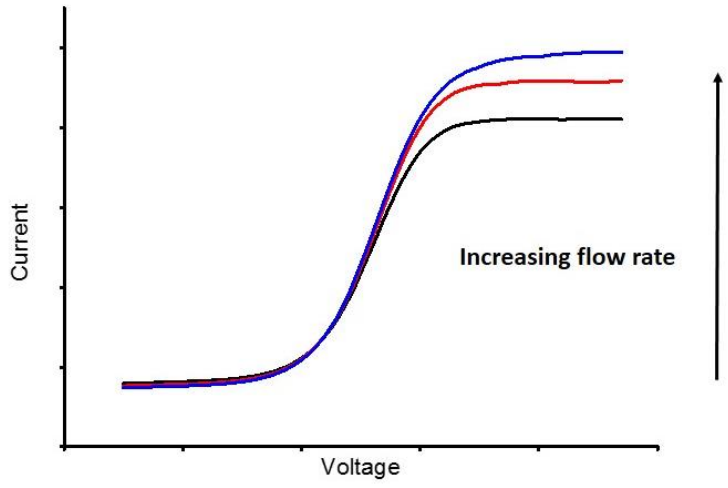

Figure 1.22 Current–voltage curves of hydrodynamic channel electrode with increasing flow rate.

1.5 Thesis structure

The remaining sections of this thesis have the following structure:

Chapter 2 details methodologies used in fabrication of fluidic devices while describing the experimental details of the project. The fabrication processes for the construction of electrodes and microchannels, using both positive and negative photoresist patterns, are detailed.

Chapter 3 presents details of the sulphide detection on macro-scale electrodes by employing the EC′ mechanism. A range of different voltammetric tools were used to investigate the redox reactions, including CV and FTACV. The split-wave phenomenon, which is related to the reaction with sulphide, are discussed. Supporting numerical models are presented to evaluate the observed responses.

Chapter 4 illustrates sulphide detection at micro-scale electrodes. The electrocatalytic reaction of sulphide is reported for the first time using the dc voltammetry and FTACV. The split-wave behaviour related to the reactions with sulphide can be detected in FTACV and has a linear relation to the sulphide concentration.

Chapter 5 presents the design, development and application of microengineered hydrodynamic reactors for the voltammetric investigations of sulphide detection. Split-wave behaviour is discussed according to sulphide concentration and flow rate. The availability of using FTACV to detect sulphide in the fluidic condition is discovered using both experiment and numerical modelling.

Reference

1. Alting, L., et al., *Micro Engineering.* CIRP Annals - Manufacturing Technology, 2003. **52**(2): p. 635-657.
2. Bhaviripudi, S., et al., *CVD Synthesis of Single-Walled Carbon Nanotubes from Gold Nanoparticle Catalysts.* Journal of the American Chemical Society, 2007. **129**(6): p. 1516-1517.
3. Peterson, D.S., et al., *Enzymatic Microreactor-on-a-Chip: Protein Mapping Using Trypsin Immobilized on Porous Polymer Monoliths Molded in Channels of Microfluidic Devices.* Analytical Chemistry, 2002. **74**(16): p. 4081-4088.
4. Vican, J., et al., *Development of a microreactor as a thermal source for microelectromechanical systems power generation.* Proceedings of the Combustion Institute, 2002. **29**(1): p. 909-916.
5. Chae, J., S.S. Park, and T. Freiheit, *Investigation of micro-cutting operations.* International Journal of Machine Tools and Manufacture, 2006. **46**(3–4): p. 313-332.
6. A. Baniya, et al., *Lab-on-a-Chip Device for Hydrogen Sulfide Sensing in Biomedical and Environmental Applications Using Electrochemical Approach.* ASME 2015 International Technical Conference and Exhibition on Packaging and Integration of Electronic and Photonic Microsystems collocated with the ASME 2015 13th International Conference on Nanochannels, Microchannels, and Minichannels, 2015. **3**.
7. A. Baniya, S.T., E. Borquist, D. Bailey, D. Wood, J. Glawe, C. Kevil and L. Weiss, *Hydrogen Sulfide Sensing Using Lab-on-a-Chip Device for Biomedical and Environmental Use.* ASME 2015 International Mechanical Engineering Congress and Exposition, 2015. **3**.
8. Dittrich, P.S. and A. Manz, *Lab-on-a-chip: microfluidics in drug discovery.* Nat Rev Drug Discov, 2006. **5**(3): p. 210-218.
9. Nie, Z., et al., *Electrochemical sensing in paper-based microfluidic devices.* Lab on a Chip, 2010. **10**(4): p. 477-483.
10. Haswell, S.J. and V. Skelton, *Chemical and biochemical microreactors.* TrAC Trends in Analytical Chemistry, 2000. **19**(6): p. 389-395.
11. Cukalovic, A., J.-C.M.R. Monbaliu, and C.V. Stevens, *Microreactor Technology as an Efficient Tool for Multicomponent Reactions*, in *Synthesis of Heterocycles via Multicomponent Reactions I*, A.R.V. Orru and E. Ruijter, Editors. 2010, Springer Berlin Heidelberg: Berlin, Heidelberg. p. 161-198.
12. Ehrfeld, W., V. Hessel, and V. Haverkamp, *Microreactors*, in *Ullmann's Encyclopedia of Industrial Chemistry*. 2000, Wiley-VCH Verlag GmbH & Co. KGaA.
13. Beeby, S.P., et al., *A micro electromagnetic generator for vibration energy harvesting.* Journal of Micromechanics and Microengineering, 2007. **17**(7): p. 1257.

14. Yen, B.C. and J.H. Lang, *A variable-capacitance vibration-to-electric energy harvester.* IEEE Transactions on Circuits and Systems I: Regular Papers, 2006. **53**(2): p. 288-295.
15. Horowitz, S.B., et al., *A MEMS acoustic energy harvester.* Journal of Micromechanics and Microengineering, 2006. **16**(9): p. S174.
16. Bard, A.J. and L.R. Faulkner, *Electrochemical methods: fundamentals and applications.* 2001.
17. PLETCHER, D., et al., *Instrumental Methods in Electrochemistry*. 2001: Horwood Publishing Chichester.
18. Fisher, A.C., *Electrode Dynamics*. 1996: Oxford University Press.
19. Yairi, M. and C. Richter, *Massively parallel microfluidic pump.* Sensors and Actuators A: Physical, 2007. **137**(2): p. 350-356.
20. Wang, S.S., et al., *Acoustically induced bubbles in a microfluidic channel for mixing enhancement.* Microfluidics and Nanofluidics, 2009. **6**(6): p. 847-852.
21. Arvia, A.J. and J.S.W. Carrozza, *Mass transfer in the electrolysis of CuSo4− H2SO4 in aqueous solutions under limiting current and forced convection employing a cylindrical cell with rotating electrodes.* Electrochimica Acta, 1962. **7**(1): p. 65-78.
22. Paddon, C.A., et al., *Coulometry on the Voltammetric Timescale: Microdisk Potential-Step Chronoamperometry in Aprotic Solvents Reliably Measures the Number of Electrons Transferred in an Electrode Process Simultaneously with the Diffusion Coefficients of the Electroactive Species.* Electroanalysis, 2007. **19**(1): p. 11-22.
23. Cottrell, F.G., *Application of the Cottrell equation to chronoamperometry.* Z. Phys. Chem., Stoechiometrie und Verwandt-schaftslehre, 1902(42).
24. Savéant, J.M. and E. Vianello, *Potential-sweep voltammetry: General theory of chemical polarization.* Electrochimica Acta, 1967. **12**(6): p. 629-646.
25. Nicholson, R.S., *Theory and Application of Cyclic Voltammetry for Measurement of Electrode Reaction Kinetics.* Analytical Chemistry, 1965. **37**(11): p. 1351-1355.
26. Lether, F.G. and P.R. Wenston, *An algorithm for the numerical evaluation of the reversible Randles-Sevcik function.* Computers & Chemistry, 1987. **11**(3): p. 179-183.
27. Kissinger, P.T. and W.R. Heineman, *Cyclic voltammetry.* Journal of Chemical Education, 1983. **60**(9): p. 702.
28. Zhao, Y., et al., *Selective detection of dopamine in the presence of ascorbic acid and uric acid by a carbon nanotubes-ionic liquid gel modified electrode.* Talanta, 2005. **66**(1): p. 51-57.
29. O'HAYRE, R.P., et al., *FUEL CELL FUNDAMENTALS*. 2009.
30. Finklea, H.O., et al., *Characterization of octadecanethiol-coated gold electrodes as microarray electrodes by cyclic voltammetry and ac impedance spectroscopy.* Langmuir, 1993. **9**(12): p. 3660-3667.

31. Nicholson, R.S. and I. Shain, *Theory of Stationary Electrode Polarography. Single Scan and Cyclic Methods Applied to Reversible, Irreversible, and Kinetic Systems.* Analytical Chemistry, 1964. **36**(4): p. 706-723.
32. Mirceski, V., et al., *Square-Wave Voltammetry: A Review on the Recent Progress.* Electroanalysis, 2013. **25**(11): p. 2411-2422.
33. Barker, G.C. and I.L. Jenkins, *Square-wave polarography.* Analyst, 1952. **77**(920): p. 685-696.
34. Barker, G.C., *Square wave polarography and some related techniques.* Analytica Chimica Acta, 1958. **18**: p. 118-131.
35. Ramaley, L. and M.S. Krause, *Theory of square wave voltammetry.* Analytical Chemistry, 1969. **41**(11): p. 1362-1365.
36. Osteryoung, J.G. and R.A. Osteryoung, *Square Wave Voltammetry.* Analytical Chemistry, 1985. **57**(1): p. 101A-110A.
37. Bond, A.M., et al., *Changing the Look of Voltammetry.* Analytical Chemistry, 2005. **77**(9): p. 186 A-195 A.
38. Zhang, J., et al., *Large-Amplitude Fourier Transformed High-Harmonic Alternating Current Cyclic Voltammetry: Kinetic Discrimination of Interfering Faradaic Processes at Glassy Carbon and at Boron-Doped Diamond Electrodes.* Analytical Chemistry, 2004. **76**(13): p. 3619-3629.
39. Tan, Y., et al., *Designer based Fourier transformed voltammetry: A multi-frequency, variable amplitude, sinusoidal waveform.* Journal of Electroanalytical Chemistry, 2009. **634**(1): p. 11-21.
40. Gavaghan, D.J. and A.M. Bond, *A complete numerical simulation of the techniques of alternating current linear sweep and cyclic voltammetry: analysis of a reversible process by conventional and fast Fourier transform methods.* Journal of Electroanalytical Chemistry, 2000. **480**(1–2): p. 133-149.
41. Gavaghan, D.J., D. Elton, and A.M. Bond, *A comparison of sinusoidal, square wave, sawtooth, and staircase forms of transient ramped voltammetry when a reversible process is analysed in the frequency domain.* Journal of Electroanalytical Chemistry, 2001. **513**(2): p. 73-86.
42. Gavaghan, D.J., et al., *Analysis of ramped square-wave voltammetry in the frequency domain.* Journal of Electroanalytical Chemistry, 2001. **512**(1–2): p. 1-15.
43. Lee, C.-Y. and A.M. Bond, *Evaluation of Levels of Defect Sites Present in Highly Ordered Pyrolytic Graphite Electrodes Using Capacitive and Faradaic Current Components Derived Simultaneously from Large-Amplitude Fourier Transformed ac Voltammetric Experiments.* Analytical Chemistry, 2009. **81**(2): p. 584-594.
44. Fleming, B.D., et al., *Separation of Electron-Transfer and Coupled Chemical Reaction Components of Biocatalytic Processes Using Fourier Transform ac Voltammetry.* Analytical Chemistry, 2005. **77**(11): p. 3502-3510.
45. Mashkina, E., et al., *Estimation of electrode kinetic and uncompensated resistance parameters and insights into their significance using Fourier*

transformed ac voltammetry and e-science software tools. Journal of Electroanalytical Chemistry, 2013. **690**: p. 104-110.

46. Milner, D.F. and M.J. Weaver, *The influence of uncompensated solution resistance on the determination of standard electrochemical rate constants by cyclic voltammetry, and some comparisons with a.c. voltammetry.* Analytica Chimica Acta, 1987. **198**: p. 245-257.
47. Lee, C.-Y. and A.M. Bond, *A Comparison of the Higher Order Harmonic Components Derived from Large-Amplitude Fourier Transformed ac Voltammetry of Myoglobin and Heme in DDAB Films at a Pyrolytic Graphite Electrode.* Langmuir, 2010. **26**(7): p. 5243-5253.
48. Lertanantawong, B., et al., *Investigation of Mediated Oxidation of Ascorbic Acid by Ferrocenemethanol Using Large-Amplitude Fourier Transformed ac Voltammetry under Quasi-Reversible Electron-Transfer Conditions at an Indium Tin Oxide Electrode.* Analytical Chemistry, 2008. **80**(17): p. 6515-6525.
49. O'Mullane, A.P., et al., *Higher Harmonic Large-Amplitude Fourier Transformed Alternating Current Voltammetry: Analytical Attributes Derived from Studies of the Oxidation of Ferrocenemethanol and Uric Acid at a Glassy Carbon Electrode.* Analytical Chemistry, 2008. **80**(12): p. 4614-4626.
50. Fleming, B.D., et al., *Detailed Analysis of the Electron-Transfer Properties of Azurin Adsorbed on Graphite Electrodes Using dc and Large-Amplitude Fourier Transformed ac Voltammetry.* Analytical Chemistry, 2007. **79**(17): p. 6515-6526.
51. Lee, C.-Y., et al., *Effects of Coupled Homogeneous Chemical Reactions on the Response of Large-Amplitude AC Voltammetry: Extraction of Kinetic and Mechanistic Information by Fourier Transform Analysis of Higher Harmonic Data.* The Journal of Physical Chemistry A, 2010. **114**(37): p. 10122-10134.
52. Guo, S., et al., *Fourier Transform Large-Amplitude Alternating Current Cyclic Voltammetry of Surface-Bound Azurin.* Analytical Chemistry, 2004. **76**(1): p. 166-177.
53. Harris, A.R., et al., *Efficient strategy for quality control of screen-printed carbon ink disposable sensor electrodes based on simultaneous evaluation of resistance, capacitance and Faradaic current by Fourier transform AC voltammetry.* Journal of Solid State Electrochemistry, 2008. **12**(10): p. 1301-1315.
54. Shiddiky, M.J.A., et al., *Large Amplitude Fourier Transformed AC Voltammetric Investigation of the Active State Electrochemistry of a Copper/Aqueous Base Interface and Implications for Electrocatalysis.* Langmuir, 2011. **27**(16): p. 10302-10311.
55. Hseu, T.-M. and G.A. Rechnitz, *Analytical study of a sulfide ion-selective membrane electrode in alkaline solution.* Analytical Chemistry, 1968. **40**(7): p. 1054-1060.
56. Raoof, J.B., R. Ojani, and M. Kolbadinezhad, *Electrocatalytic Characteristics of Ferrocenecarboxylic Acid Modified Carbon Paste Electrode in the Oxidation and Determination of L-Cysteine.* Electroanalysis, 2005. **17**(22): p. 2043-2051.

57. Tsai, D.-M., A.S. Kumar, and J.-M. Zen, *A highly stable and sensitive chemically modified screen-printed electrode for sulfide analysis.* Analytica Chimica Acta, 2006. **556**(1): p. 145-150.
58. Brazill, S.A., P. Singhal, and W.G. Kuhr, *Detection of Native Amino Acids and Peptides Utilizing Sinusoidal Voltammetry.* Analytical Chemistry, 2000. **72**(22): p. 5542-5548.
59. Chen, W., et al., *Enhancing the Analytical Selectivity of Voltammetric Technique by the Combination of Harmonic Analysis and "Fingerprint" Phase Angle Lock-in Detection.* Analytical Chemistry, 2013. **85**(1): p. 83-90.
60. Singhal, P., et al., *Sinusoidal Voltammetry for the Analysis of Carbohydrates at Copper Electrodes.* Analytical Chemistry, 1997. **69**(8): p. 1662-1668.
61. Singhal, P. and W.G. Kuhr, *Ultrasensitive Voltammetric Detection of Underivatized Oligonucleotides and DNA.* Analytical Chemistry, 1997. **69**(23): p. 4828-4832.
62. Brazill, S.A. and W.G. Kuhr, *A Single Base Extension Technique for the Analysis of Known Mutations Utilizing Capillary Gel Electrophoreisis with Electrochemical Detection.* Analytical Chemistry, 2002. **74**(14): p. 3421-3428.
63. Hebert, N.E., W.G. Kuhr, and S.A. Brazill, *Microchip capillary electrophoresis coupled to sinusoidal voltammetry for the detection of native carbohydrates.* ELECTROPHORESIS, 2002. **23**(21): p. 3750-3759.
64. Hebert, N.E., et al., *Performance of Pyrolyzed Photoresist Carbon Films in a Microchip Capillary Electrophoresis Device with Sinusoidal Voltammetric Detection.* Analytical Chemistry, 2003. **75**(16): p. 4265-4271.
65. Bond, A.M., et al., *An integrated instrumental and theoretical approach to quantitative electrode kinetic studies based on large amplitude Fourier transformed a.c. voltammetry: A mini review.* Electrochemistry Communications, 2015. **57**: p. 78-83.
66. Rountree, E.S., et al., *Evaluation of Homogeneous Electrocatalysts by Cyclic Voltammetry.* Inorganic Chemistry, 2014. **53**(19): p. 9983-10002.
67. Ward, K.R., et al., *Cyclic Voltammetry of the EC′ Mechanism at Hemispherical Particles and Their Arrays: The Split Wave.* The Journal of Physical Chemistry C, 2011. **115**(22): p. 11204-11215.
68. Nekrassova, O., et al., *The Oxidation of Cysteine by Aqueous Ferricyanide: A Kinetic Study Using Boron Doped Diamond Electrode Voltammetry.* Electroanalysis, 2002. **14**(21): p. 1464-1469.
69. Danaee, I., et al., *Kinetic studies of glucose electrocatalytic oxidation on GC/Ni electrode.* International Journal of Chemical Kinetics, 2012. **44**(11): p. 712-721.
70. Steele, B.C.H. and A. Heinzel, *Materials for fuel-cell technologies.* Nature, 2001. **414**(6861): p. 345-352.
71. Gulaboski, R. and V. Mirceski, *New aspects of the electrochemical-catalytic (EC') mechanism in square-wave voltammetry.* Electrochimica Acta, 2015. **167**: p. 219-225.

72. Sherigara, B.S., W. Kutner, and F. D'Souza, *Electrocatalytic Properties and Sensor Applications of Fullerenes and Carbon Nanotubes.* Electroanalysis, 2003. **15**(9): p. 753-772.
73. Sun, Y., H. Buck, and T.E. Mallouk, *Combinatorial Discovery of Alloy Electrocatalysts for Amperometric Glucose Sensors.* Analytical Chemistry, 2001. **73**(7): p. 1599-1604.
74. Toghill, K.E. and R.G. Compton, *Electrochemical Non-enzymatic Glucose Sensors: A Perspective and an Evaluation* International Journal of Electrochemical Science, 2010. **5**(9): p. 1246 - 1301.
75. Debe, M.K., *Electrocatalyst approaches and challenges for automotive fuel cells.* Nature, 2012. **486**(7401): p. 43-51.
76. Wei, G., et al., *A new electrocatalyst and its application method for vanadium redox flow battery.* Journal of Power Sources, 2015. **287**: p. 81-86.
77. Lawrence, N.S., J. Davis, and R.G. Compton, *Analytical strategies for the detection of sulfide: a review.* Talanta, 2000. **52**(5): p. 771-784.
78. Lawrence, N.S., et al., *Ferrocene sulfonates as electrocatalysts for sulfide detection.* Electrochimica Acta, 2006. **52**(2): p. 499-503.
79. Banks, C.E., et al., *Exploring Alkylated Ferrocene Sulfonates as Electrocatalysts for Sulfide Detection.* Electroanalysis, 2007. **19**(24): p. 2518-2522.
80. Lawrence, N.S., et al., *Amperometric Detection of Sulfide at a Boron Doped Diamond Electrode: The Electrocatalytic Reaction of Sulfide with Ferricyanide in Aqueous Solution.* Electroanalysis, 2002. **14**(7-8): p. 499-504.
81. Giovanelli, D., et al., *Electrochemical determination of sulphide at nickel electrodes in alkaline media: a new electrochemical sensor.* Sensors and Actuators B: Chemical, 2003. **88**(3): p. 320-328.
82. Jeroschewski, P., C. Steuckart, and M. Kühl, *An Amperometric Microsensor for the Determination of H2S in Aquatic Environments.* Analytical Chemistry, 1996. **68**(24): p. 4351-4357.
83. Shao, Y., et al., *Graphene Based Electrochemical Sensors and Biosensors: A Review.* Electroanalysis, 2010. **22**(10): p. 1027-1036.
84. Che, G. and S. Dong, *The application of ultramicroelectrode in homogeneous catalytic reaction—V. Electrochemical behaviour of macro-micro-macro triple and micro-micro twin electrodes and the quasi-first-order homogeneous catalytic reaction (EC′) at generation/collection electrode.* Electrochimica Acta, 1994. **39**(1): p. 87-94.
85. Mirkin, M.V. and A.J. Bard, *Multidimensional integral equations: a new approach to solving microelectrode diffusion problems: Part 2. Applications to microband electrodes and the scanning electrochemical microscope.* Journal of Electroanalytical Chemistry, 1992. **323**(1): p. 29-51.
86. Brown, R.J.C. and D.J.L. Brett, *Microelectrode voltammetry as a high accuracy method for determination of diffusion coefficients.* Microchimica Acta, 2009. **164**(3): p. 337-344.

87. Soh, K.L., et al., *Diamond-derived microelectrodes array for electrochemical analysis.* Diamond and Related Materials, 2004. **13**(11–12): p. 2009-2015.
88. Brookes, B.A., N.S. Lawrence, and R.G. Compton, *Microdisk Electrode Voltammetry: Theoretical Characterization and Experimental Verification of a Novel Electrocatalytic Mechanism.* The Journal of Physical Chemistry B, 2000. **104**(47): p. 11258-11267.
89. Niwa, O., *Electroanalysis with interdigitated array microelectrodes.* Electroanalysis, 1995. **7**(7): p. 606-613.
90. ŠTULÍK, K., et al., *Microelectrodes. Definitions, characterization, and applications (Technical report).* INTERNATIONAL UNION OF PURE AND APPLIED CHEMISTRY, 2000. **72**(8): p. 1483-1492.
91. Forster, R.J., *Microelectrodes: new dimensions in electrochemistry.* Chemical Society Reviews, 1994. **23**(4): p. 289-297.
92. Pavlovic, E., et al., *Microfluidic Device Architecture for Electrochemical Patterning and Detection of Multiple DNA Sequences.* Langmuir, 2008. **24**(3): p. 1102-1107.
93. Wang, J. and M. Ariel, *The rotating disc electrode in flowing systems.* Analytica Chimica Acta, 1978. **99**(1): p. 89-98.
94. NAVARRETE, R., *DETERMINING THE BEHAVIOR OF THE ROTATING DISK ELECTRODE SYSTEM.*
95. Opekar, F. and P. Beran, *Rotating disk electrodes.* Journal of Electroanalytical Chemistry and Interfacial Electrochemistry, 1976. **69**(1): p. 1-105.
96. Laevers, P., et al., *A wall jet electrode reactor and its application to the study of electrode reaction mechanisms Part II: A general computational method for the mass transport problems involved.* Journal of Applied Electrochemistry, 1995. **25**(11): p. 1023-1030.
97. Fisher, A.C., et al., *The wall-jet electrode.* Journal of Electroanalytical Chemistry and Interfacial Electrochemistry, 1991. **318**(1): p. 53-59.
98. Albery, W.J., *The current distribution on a wall-jet electrode.* Journal of Electroanalytical Chemistry and Interfacial Electrochemistry, 1985. **191**(1): p. 1-13.
99. Munshi, A.S. and R.S. Martin, *Microchip-based electrochemical detection using a 3-D printed wall-jet electrode device.* Analyst, 2016. **141**(3): p. 862-869.
100. Macpherson, J.V., S. Marcar, and P.R. Unwin, *Microjet Electrode: A Hydrodynamic Ultramicroelectrode with High Mass-Transfer Rates.* Analytical Chemistry, 1994. **66**(13): p. 2175-2179.
101. Cannan, S. and P.R. Unwin, *Characterization and Assessment of the Microjet Electrode as a Detector for HPLC.* Electroanalysis, 2004. **16**(9): p. 712-718.
102. Simjee, N., P.R. Unwin, and J.V. Macpherson, *Hydrodynamic Modulation Voltammetry with a Dual Disk Chopped Flow-Microjet Electrode (CF-MJE).* Electroanalysis, 2003. **15**(18): p. 1445-1452.

103. Macpherson, J.V. and P.R. Unwin, *Characterization and Application of a Mercury Hemisphere Microjet Electrode.* Analytical Chemistry, 1997. **69**(24): p. 5045-5051.
104. Matthews, S.M., et al., *Attributes of Direct Current Aperiodic and Alternating Current Harmonic Components Derived From Large Amplitude Fourier Transformed Voltammetry Under Microfluidic Control in a Channel Electrode.* Analytical Chemistry, 2012. **84**(15): p. 6686-6692.
105. Choban, E.R., et al., *Microfluidic fuel cell based on laminar flow.* Journal of Power Sources, 2004. **128**(1): p. 54-60.
106. Illa, X., et al., *A cyclo olefin polymer microfluidic chip with integrated gold microelectrodes for aqueous and non-aqueous electrochemistry.* Lab on a Chip, 2010. **10**(10): p. 1254-1261.
107. Kenis, P.J.A., R.F. Ismagilov, and G.M. Whitesides, *Microfabrication Inside Capillaries Using Multiphase Laminar Flow Patterning.* Science, 1999. **285**(5424): p. 83-85.
108. Rossier, J., F. Reymond, and P.E. Michel, *Polymer microfluidic chips for electrochemical and biochemical analyses.* ELECTROPHORESIS, 2002. **23**(6): p. 858-867.
109. Rossier, J.S., et al., *Electrochemical Detection in Polymer Microchannels.* Analytical Chemistry, 1999. **71**(19): p. 4294-4299.
110. Sansuk, S., et al., *Ultrasensitive Detection of Dopamine Using a Carbon Nanotube Network Microfluidic Flow Electrode.* Analytical Chemistry, 2013. **85**(1): p. 163-169.
111. Chen, I.J. and I.M. White, *High-sensitivity electrochemical enzyme-linked assay on a microfluidic interdigitated microelectrode.* Biosensors and Bioelectronics, 2011. **26**(11): p. 4375-4381.

Chapter 2 Microfabrication procedures and numerical methodology

2.1 Introduction

This chapter briefly reviews some of the techniques available for the fabrication of microengineered reactors. This is followed by a detailed overview of the procedures employed for the design and fabrication of the microengineered reactors used for measurements in the thesis. Positive fabrication is used for the electrodes and negative for the microchannels.

2.2 Microfabrication methodology

Photolithography (Figure 2.1) typically uses an ultraviolet (UV) light as an energy source to expose a photoresist[1], which has been spin coated onto a substrate. The photoresist is exposed through a high-precision patterned mask to transfer an image of the mask onto the photoresist-coated substrate. In the case of a positive photoresist, the exposed part of the polymer film will be erased after chemical development; for a negative photoresist, the photoresist on the exposed area will remain after chemical development[2]. An extension of traditional UV photolithography is called deep-UV photolithography, this was first introduced by Lin in 1975[3]. Compared with conventional UV methods, the power source of the deep-UV approach is within the range of 200–250 nm. Its shorter wavelength has made it possible to obtain more intensive integrated microproducts with high resolution, as well as the possibility of mass manufacturing[4, 5]. The introduction of deep-UV lithography also broadens the application of photolithography in various materials.

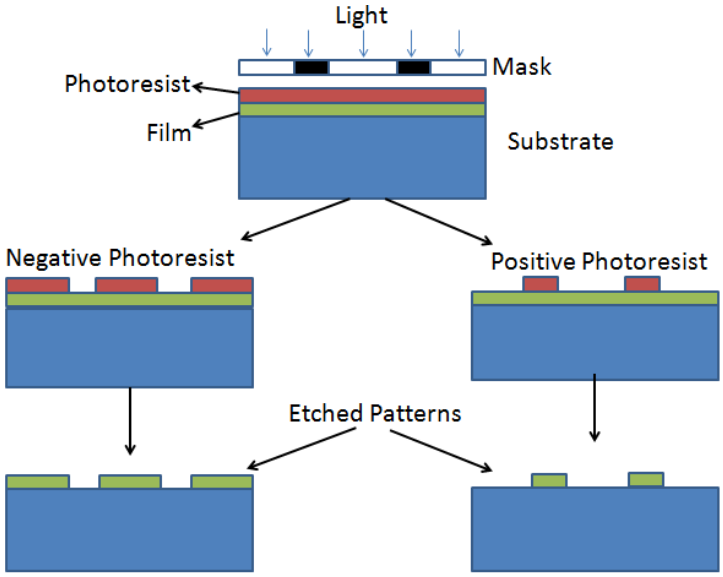

Figure 2.1 Photolithography in microfabrication[6].

X-ray lithography is a higher-energy lithographic technique. This approach was initially developed as a candidate for conventional lithography. Its short wavelength, ranging from 0.2 nm to 5 nm, allows X-ray lithography to reach higher resolution, down to 15 nm features and is not be limited by diffraction[7]. In comparison with the optical lithographic techniques, X-ray lithography can be carried out using simple facilities as lenses are not required. Poly(methyl methacrylate) (PMMA) is one of the commonly used substrate materials due to its positive response characteristics with X-rays, rapidly hardening when exposed. After exposure, chemical development reveals the patterned features. The advantages of X-ray lithography are that it is easy to apply, it has high resolution for accurate manufacturing and it requires a relatively short time in fabrication.

Other energetic power sources for lithography include electron and ion beams; these can offer advantages of high resolution and direct printing of patterns on wafers[8, 9]. Devices used in this thesis were fabricated using photolithographic techniques. The

following sections provide a detailed account of the photolithographic process employed for electrode fabrication and channel fabrication as well as device assembly.

2.2.1 Photolithographic process

2.2.1.1 Substrate preparation

In this thesis, the substrate used for the electrode fabrication is glass of various thickness cut into the desired size by a diamond glass cutter. For the experiments reported in the results chapters, glass wafers with a thickness of 1mm were used for electrode fabrication. All wafers were cut into size 6×6 cm^2 samples and cleaned using piranha solution with sulphuric acid: hydrogen peroxide ratio of 3:1 for at least 15 minutes to remove contaminants on the glass wafers, including dust and abrasive glass particles. Any organic or inorganic residues from glass manufacture would cause bubbles in the resist or electrode structures. In the final step, wafers were rinsed with milli-Q water and dried using high-speed nitrogen gas. Channel structures were constructed onto glass or poly(dimethylsiloxane) (PDMS) substrates using the details described below.

2.2.1.2 Coating of photoresists

A thin film of photoresist of uniform thickness was coated onto the glass using a Delta 10 spin coater (Karl Suss). The pretreated glass wafer was placed on the spin coater and stabilized by a vacuum. Small quantities of photoresist were dropped onto the wafer and the film thickness was controlled by the parameters of spinning speed, acceleration and cycle numbers, in accordance with the viscosity of the polymers.

Both positive and negative photoresists were applied for the overall fabrication process. The positive photoresist used in electrode fabrication was S1828 (1-methosy-2-propylacetate). Table A.1 demonstrated the protocol used for the positive photoresist stages. For procedures using a negative photoresist, SU8-2100 was coated onto the glass wafers. The viscosity of SU8 was larger than that of the positive photoresist. In this case, the coating process could be separated into two steps. A low-speed spin was first applied to spread the polymer uniformly. Then a high-speed spin was used to monitor the thickness of the film layer. Table A.2 shows the protocol for the negative photoresist steps.

2.2.1.3 Pre-baking

Before exposing under UV light, a pre-baking process was carried out to evaporate the excess solvent on a time-controllable hot plate. In this case, the thickness of film was reduced and the adhesion of photoresist to substrate was strengthened. The heating time and temperature varied and depended on the type of photoresist and thickness of the film. Precise control of the temperature and the time of baking were vital. Table A.3 shows the soft baking process for the positive photoresist. For the negative photoresist (Table A.4), a two-step baking was required and the temperature was dependent on the thickness of the layers.

2.2.1.4 Exposure process

The cooled glass wafer was then exposed in a mask aligner (Karl Suss, MJB3), with the UV light exposed through a mask with the desired pattern for transferring into the photoresist-coated wafer. In the case of the positive photoresist, the chemical bond of

the exposed area was broken by UV light so it could be washed away by a specific developer solution. The unexposed part was kept in the development process.

For the negative photoresist, exposure to UV light hardened the adhesive bonding between the glass wafer and the resist. The unexposed area was therefore soluble in negative developer solution. The time should be carefully controlled to avoid under- or overexposure. Insufficient cross-linking occurred when the exposure time was not long enough, which could lead to weak bonding of the negative photoresist.

2.2.1.5 Post-baking

The post-baking process was applied for the negative photoresist procedures to cross-link the exposed polymers. The purpose of post-baking was to strengthen the bonds of exposed areas and to avoid being washed away by developer solution, which leads to inaccuracy of the microstructure. As indicated in Table A.5, the time of post-baking varied depending on the thickness of the polymer layer.

2.2.1.6 Development

Developer solutions were employed to obtain the transferred pattern on the exposed wafer. The photoresist on the glass wafer was selectively washed away depending on the type of polymers and lithographic process. For the positive fabrication, AZ351 (Shipley) was used and the exposed part was efficiently removed after being rinsed for 1 min. For the negative photoresist, EC solvent developer (MicroChem) was used in this work. Table A.6 shows the development time for negative fabrication, which was related to the room temperature and experimental conditions.

2.2.2 Microelectrode fabrication

Patterned glass wafer was placed in a metal evaporator (Auto 306 vacuum coating system) that could coat a wide range of metals. First, the chamber was pumped down to a magnitude of 4×10^{-7}. When the vacuum condition was reached, titanium in the container was heated up to its evaporating temperature and coated onto the wafer with thickness around 20 nm. Then, a gold wire was heated and coated over the titanium layer to form a thin film of gold whose thickness was approximately 150 nm. The titanium acted as an adhesive portion to link the glass substrate and gold electrode. The chamber was vented when the coating process was finished. Then, the coated wafers were immersed in acetone solution and the undesired part was wiped off with cotton sticks. The process lasted about 10 minutes and the gold electrode with designed pattern was achieved. The resulting gold electrode is shown in Figure 2.2.

Figure 2.2 Gold electrode of the positive fabrication.

The whole process should be strictly undertaken in a clean room to ensure the accuracy of the electrodes. Other factors, such as the resolution of the mask, the cleanness of the substrate, the time of pre-baking, the time of post-baking and the time of development,

also affected the precision of the gold electrodes. The fabrication process of microelectrodes is depicted in Figure 2.3.

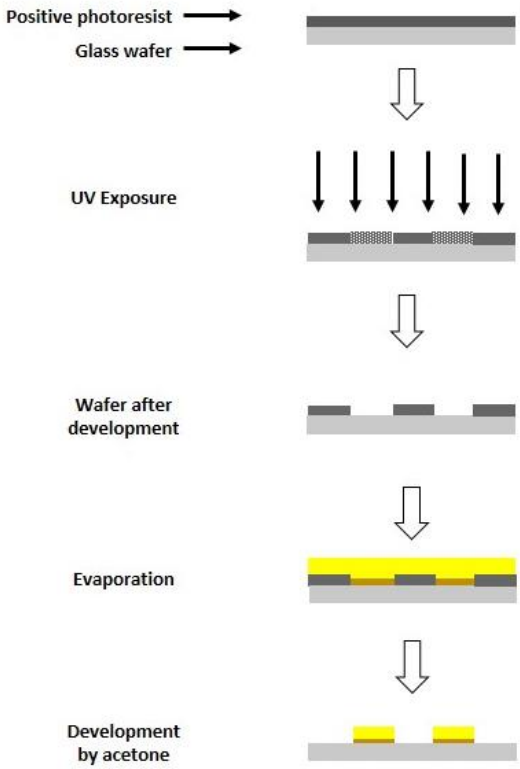

Figure 2.3 Processes of positive microfabrication.

2.2.3 Microchannel fabrication

These were three different approaches for channel fabrication used in this thesis: (1) the channels formed from SU-8 photoresist; (2) channels formed from PDMS; (3) PDMS gaskets sandwiched between an electrode plate and a glass cover slip. Fabrication of the SU-8 channel followed an analogous approach to the processes of negative photoresist fabrication. The time of UV exposure and spinning speed of the spin coater were varied, depending on the required height of the channel. In the case of PDMS-based channels, a mold was produced by the negative microfabrication and used for the molding PDMS channels numerous times.

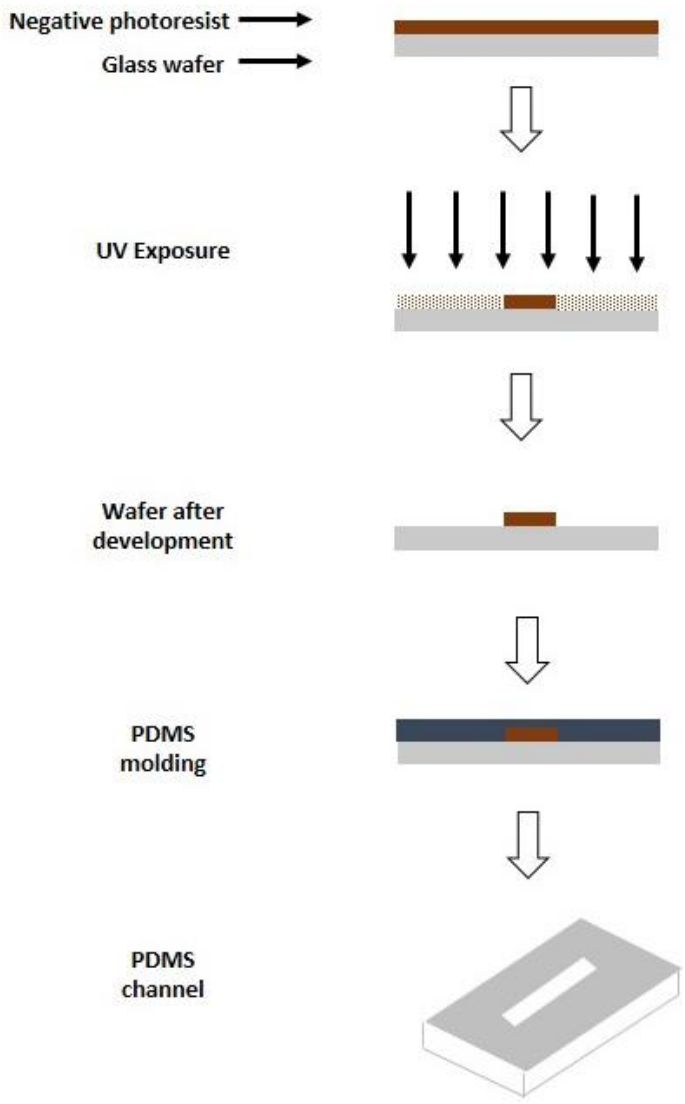

Figure 2.4 Processes of negative microfabrication.

The PDMS preparation procedure was as follows. PDMS solution was rested for 15 min to allow the bubbles to discharge, then poured onto the micro-mold fabricated by the negative photoresist procedure as detailed in Section 2.2.1. The mold was then left for 24 h at room temperature to allow polymer curing. The cured PDMS channel was peeled from the mold. Inlets for fluid were punctured and inlet tubes were fixed by Araldite glue. To enhance the bonding between PDMS and the glass substrate, plasma

treatment was used on the surface of PDMS before contacting the glass wafer. Figure 2.4 depicts the process of channel fabrication.

A modification of the channel structure, namely a PDMS gasket, was used in this thesis to meet the demands for larger channel height applications. Similar to the process of PDMS channel fabrication, the acceleration duration and spin speed were important issues to control the geometry of the prepared gaskets. A spin coat speed of 500 rpm with acceleration of 100 rpm/s for 5 s to spread the PDMS evenly on the substrate was used followed by an increase to 250 rpm with acceleration of 100 rpm/s for 55 s. The wafer was baked in an oven at a temperature of 60°C for 2 h. The procedure was repeated three times and the resulting micro-product peeled from the mold.

2.2.5 Microchannel device fabrication

Two approaches were employed for device assembly: plasma-aided bonding and mechanical bonding. For the former, PDMS and glass substrates were treated by a low-pressure oxygen plasma. The surface of glass wafer was modified so that the adhesive strength between the PDMS and glass substrate could be enhanced. This kind of channel sealing is irreversible. The structure of the device is shown in Figure 2.5 (a). The three-electrode microfluidic system was achieved with working, counter and reference electrodes fabricated on the glass substrate.

The second method was a mechanical bonding-based assembly. Two pieces of Perspex plate were employed to fix the glass substrate, PDMS gasket and a PDMS substrate. The purpose of using PDMS substrate was to seal the top side of gasket due to the stronger adhesion between PDMS films than with other material. By adjusting the tightness of screws, the height of the PDMS channel could be slightly varied (the height

could be calibrated by electrochemical methods). The schematic structure is presented in Figure 2.5 (b).

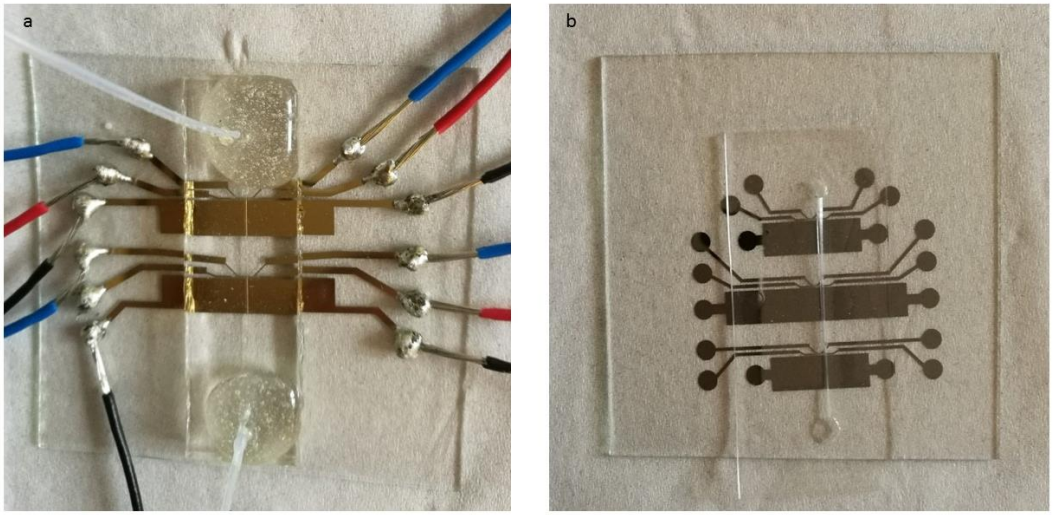

Figure 2.5 Structure of (a) microchannel and (b) microgasket.

2.3 Equipment

Apparatus	Supplier	Model
Analytical balance	Precisa	XT 120A
Diamond glass cutter	Diamond Tech	DL 3000XL
Evaporator	Edwards	AUTO 306
Spin coater	Karl Suss	Delta 10 TT
Mask aligner	Karl Suss	MJB3 340 nm 10W cm^{-2}
Microscope	Olympus	IX70
Syringe pump	Harvard Apparatus	PHD 2000
Plasma system	Diener Electronic	FEMTO

2.4 Reagents

The reagents used in the experiment are listed below.

Reagents	Supplier	Grade
Acetone	Fisher Chemical	General purpose grade
Borate buffer solution	Acros organics	Traceable to NIST
Ethanol	Fluka	Absolute
Ferrocenecarboxylic acid	Fluka	≧97%
Ferrocenemethanol	Sigma-Aldrich	>97%
Gold wire	Advent Materials	99.99%
Hydrogen Peroxide	Sigma-Aldrich	30 wt. % in H_2O
Isopropanol	Fisher Chemical	Laboratory reagent grade
L-cysteine	Sigma-Aldrich	≧98.5%
Microposit 351 developer	Dow Corning	-
Microposit EC solvent	Dow Corning	-
Microposit S1828	Dow Corning	-
PDMS	Dow Corning	-
Potassium chloride	Fisher Chemical	Analytical reagent grade
Potassium nitrate	Sigma-Aldrich	≧99.0%
SU-8 2100	MicroChem	-

Sulphuric acid	Fisher Chemical	>95%
Titanium wire	Advent Materials	>99.6%

Reference

1. Yong, K., et al., *A Simple Photomask with Photoresist Mask Layer for Ultraviolet-Photolithography and Its Application for Selectively Photochemical Surface Modification of Polymers.* Chinese Journal of Analytical Chemistry, 2007. **35**(5): p. 623-627.
2. Becker, H. and C. Gärtner, *Polymer microfabrication technologies for microfluidic systems.* Analytical and Bioanalytical Chemistry, 2008. **390**(1): p. 89-111.
3. Yoshiaki, M., et al., *Deep-UV Photolithography.* Japanese Journal of Applied Physics, 1978. **17**(3): p. 541.
4. Gipstein, E., A.C. Ouano, and T. Tompkins, *Evaluation of Pure Novolak Cresol‐Formaldehyde Resins for Deep U.V. Lithography.* Journal of The Electrochemical Society, 1982. **129**(1): p. 201-205.
5. Bogaerts, W., et al., *Fabrication of photonic crystals in silicon-on-insulator using 248-nm deep UV lithography*. IEEE Journal of Selected Topics in Quantum Electronics, 2002. **8**(4): p. 928-934.
6. Khaleel, H.R., H.M. Al-Rizzo, and A.I. Abbosh, *Design, Fabrication, and Testing of Flexible Antennas*. Advancement in Microstrip Antennas with Recent Applications. 2013.
7. Heuberger, A., *X‐ray lithography.* Journal of Vacuum Science & Technology B, 1988. **6**(1): p. 107-121.
8. Tseng, A.A., et al., *Electron beam lithography in nanoscale fabrication: recent development.* IEEE Transactions on Electronics Packaging Manufacturing, 2003. **26**(2): p. 141-149.
9. Khoury, M. and D.K. Ferry, *Effect of molecular weight on poly(methyl methacrylate) resolution.* Journal of Vacuum Science & Technology B, 1996. **14**(1): p. 75-79.

Chapter 3 Heterogeneous electron transfer coupled with chemical reaction on a macro-electrode

3.1 Introduction

In this chapter, electrochemical detection of sulphide is reported using the electrocatalytic mechanism. In these voltammetric studies, FTACV was used for the first time to investigate the reaction and explore the split wave phenomena that can be observed for this system using the traditional dc cyclic voltammetric technique. The chapter begins with a brief review of currently available methods for the detection of sulphide substrates. Supporting numerical simulations of the EC′ process using the FTACV approach was employed to provide theoretical support.

3.2 Detection of sulphide in aqueous solution

Regardless of the state, detection of sulphide, whether in the gaseous form or in the liquid form, has been investigated widely. Even though it plays a significant role in biogeochemical processes, the toxicity of sulphide (even a small amount of sulphide will induce physiological sickness) has attracted much attention both in research and industry[1]. Taking H_2S as an example, oil fields can produce hydrogen sulphide gas and bring danger to the rig workers. A short-term exposure to 500–1000 ppm of H_2S will cause serious harm to human bodies or even be life threatening. According to the UK Health and Safety Executive, the acceptable concentration of H_2S should be lower than 5 ppm for an eight-hour working shift[2].

In order to avoid the accidents caused by H_2S, four main methods are applied for the detection of sulphide: (1) classical titrimetric detection; (2) kinetic spectroscopic techniques; (3) chromatographic detection; (4) electrochemical techniques[1, 3]. The iodometric technique is the most commonly used in the titration of sulphide wherein an excess amount of iodine is added in the aqueous solution to detect the presence of sulphide, as seen in Scheme 3.1[4]. The simplicity and accuracy of the iodometric technique have gained it popularity as a fast method for sulphide quantification.

$$H_2S + I_2 \rightarrow 2HI + S$$

$$2\ S_2O_3^{2-} + I_2 \rightarrow S_4O_6^{2-} + 2I^-$$

Scheme 3.1 Mechanism of hydrogen sulphide detection by the iodometric technique.

The methylene blue test is one of the most sensitive approaches to characterise sulphide in the aqueous environment, with the detection involving the reaction of sulphide with N,N-dimethyl-p-phenylenediamine. In addition, the presence of a small amount of oxidant, such as ferric ions, is required to produce methylene blue[1]. The concentration of sulphide can be determined by the characterisation of coloration using a spectrophotometric measurement, such as UV/visible absorption and fluorescence[5, 6]. Even though the sensitivity of sulphide detection by spectroscopy can reach concentration levels as low as 0.01 ppm, the chemical selectivity only to sulphide is an issue.

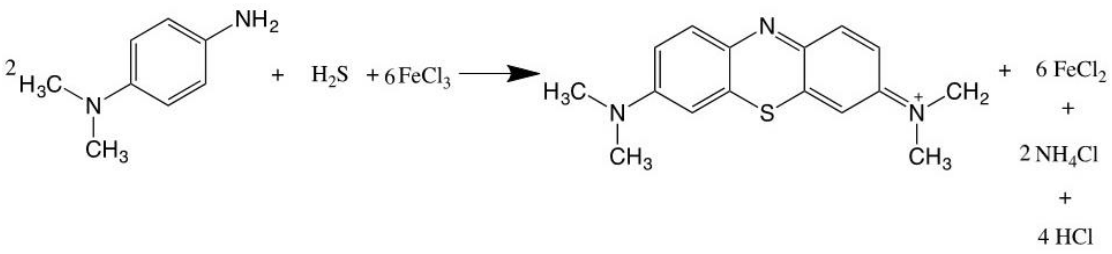

Scheme 3.2 Mechanism of the methylene blue test.

Chromatography is another efficient method that is widely used for sulphide detection. Its ability to separate the sulphide species from other compounds has allowed it to extend its application in complex media under certain circumstances. The pre-column derivatisation employed is a common practice used to enhance the chromatographic characteristics. By introducing the derivatisation process, the separation of analytes in a complicated medium is simplified, which in turn enhances the selectivity of chromatography[7]. Notably, chromatography can be combined with other analytical methods such as mass spectrometry to enhance the accuracy[8, 9].

For the electrochemical techniques, the electrochemical sensor combines electrodes and electrolyte in the detector. H_2S diffuses through a permeable membrane and reacts with the reversible couple in the sensor. The variation of current induced by the reaction at the electrode is linear in the sulphide concentration, which enables a display or an amplifier device to generate an indication of the H_2S concentration. The electrochemical techniques have two key characteristics: continuous sulphide monitoring and high sensitivity. Different from the other techniques, whose procedure limits their operation in the wellbore, the electrochemical sensor due to its repeatability, the ease of signal capturing, low power consumption and no need for pre-concentrating have allowed it to monitor the H_2S level continuously in the oil field[10, 11]. Moreover, in the drilling devices, the electrochemical sensor usually comprises a temperature and pressure compensator to stabilize its application and sensitivity in the wellbore[12]. The sensitivity of the commercial electrochemical sensor can be down to 20nM. As such, the electrochemical techniques have been developed as an alternative to the conventional methods and have gradually expanded their application to a range of sulphide derivatives[10]. There are four main types of electrochemical sensors: potentiometric, galvanic, coulometric and amperometric. The amperometric and potentiometric sensors based on the electrocatalytic mechanism have proven their convenience and accuracy in chemical detection. However, the electrochemical processes on certain sulphide species, such as hydrogen sulphide in gas form, cannot

be directly applied. To solve this problem, modifications to the electrode and the membrane material[13, 14], and the development of electrocatalytic pathways[15] have been reported. Carbon electrodes and their modified materials, such as a combination of carbon nanotube (CNT) with organic functional groups, have proven their capability and precision in sulphide detection. Improvements in the stability of hydrogen sulphide detection have been achieved when using a glassy carbon electrode that is modified with CNTs through chemical vapour deposition[13]. In the detecting process, the CNTs act as a catalyst that encourages the oxidation of sulphide.

$$2[Fe(CN)_6]^{4-} \rightleftharpoons 2[Fe(CN)_6]^{3-} + 2e^-$$

$$2[Fe(CN)_6]^{3-} + HS^- \rightarrow 2[Fe(CN)_6]^{4-} + H^+ + S$$

Scheme 3.3 Mechanism of sulphide oxidation with ferrocyanide/ferricyanide in the EC′ mechanism.

Introducing the functional groups that induce mediated oxidation is another effictive approach for sulphide detection. The redox functional groups, which are usually added directly to the electrolyte or screen-printed onto the electrode surface, have changed the pathway of sulphide oxidation. The sulphide, either in the gas form or in aqueous solution, is oxidised by the functional groups, as Scheme 3.3 shows[14]. Determination of sulphide can be realized by monitoring the current-voltage behaviour of the redox reaction. The electrochemical responses obtained by the amperometric sulphide sensors are based on reversible mediators. The detection of H_2S with ferrocyanide/ferricyanide redox mediator has been well investigated and its mechanism has been developed as commercial H_2S electrochemical sensors[11, 15]. Other redox couples, such as ferrocene derivatives[16] and phthalocyanide compound[17], have also been reported in many papers.

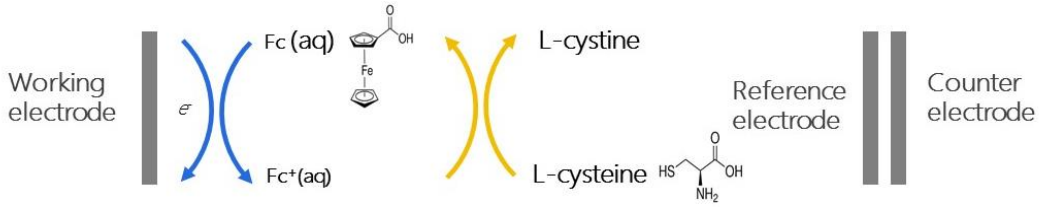

Figure 3.1 Electrocatalytic reaction of FCA with L-cysteine.

In this thesis, the ferrocenecarboxylic acid (FCA) redox couple was used as the redox mediator due to its proven high stability and electrocatalytic activation in the reaction with sulphide[18, 19]. Considering the toxicity and great harm, the H_2S gas cannot be used in the general laboratory; therefore, L-cysteine, a sulphur-containing acid, is used to mimic H_2S in aqueous solution. In the electrocatalytic reaction with the iron-based mediator (ferrocene derivatives or ferrocyanide ion), the mechanism of L-cysteine oxidation is the same as with the process of H_2S[20-23]. In addition, L-cysteine has been widely studied due to its importance in biological processes, pharmaceutical production and formation of chemical complexes[18, 24]. Thus, we can understand the electrochemical processes in a safe working environment without having to handle H_2S gas and have the safety procedures put in place to do this. As Figure 3.1 depicts, the functional group ferrocene is oxidized to ferricenium ion. When sulphide is present in the solution, an irreversible reaction occurs. The cysteine is oxidized to cystine and ferricenium ion is reduced to reproduce the reactant FCA on the working electrode. By measuring the current behaviour of the Fc/Fc^+ couple, the cysteine concentration in the aqueous solution shall be detected. In this chapter, a three-electrode set-up, composed of a glassy carbon working electrode (IJ Cambria Scientific Ltd), a platinum counter electrode and a silver/silver chloride reference electrode, is used.

3.3 Results and discussion

3.3.1 EC′ reaction of ferrocene derivative and L-cysteine on 1 mm glassy carbon electrode by dc voltammetry

First, the electrochemical performance of the redox reaction was studied by CV. The FCA aqueous solution (2mM, 0.1M KCl, pH = 9.2 borate buffer solution) was prepared as electrolyte and was characterised using a 1mm (in diameter) glassy carbon electrode. In Figure 3.2 (a), the effect of the scan rate on the current response is recorded. When the scan rate varied in the range from 5 mV/s to 200 mV/s, the redox peak potentials remained at +0.356 V for the oxidation and +0.283 V for the reduction vs a silver/silver chloride reference electrode. Moreover, the value of peak current increased as a function of the square root of the scan rate, indicating good reversible redox characteristics.

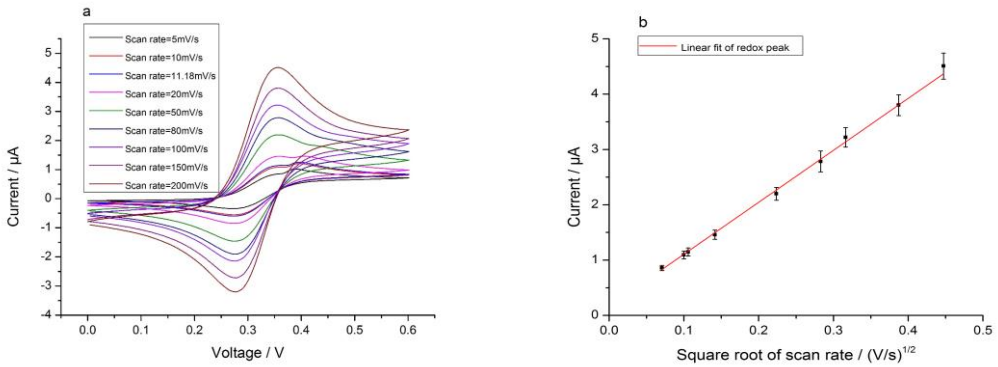

Figure 3.2 CV of 2 mM FCA in the absence of L-cysteine with various scan rates (5, 10, 11.18, 20, 50, 80, 100, 150, 200 mV/s) (a) at a 1mm glassy carbon electrode; (b) linear fit of the peak current against the square root of the scan rate.

The linearity ($I_p/\mu A$ = 9.65 × $10^{-6}\sqrt{scan\ rate\ /(mV/s)}$ +1.55 × 10^{-7}, N = 9, R = 0.9991) is shown in Figure 3.2 (b). The diffusion coefficient of FCA was derived from the slope value of the linear curve by the Randles-Sevcik equation, which was (5.22 ± 0.05) × 10^{-6} cm^2/s, which is in good agreement with the literature[25].

Next, catalytic measurements were recorded by introducing L-cysteine into the reaction vessel with FCA electrolyte solution. CV measurements were carried out as a function of scan rate (10 mV/s to 200 mV/s) and Figure 3.3 shows a typical current response observed for the reaction using the 1 mm glassy carbon electrode when the cysteine-FCA concentration ratios were 1:2, 1:1, 1.5:1 and 2:1. In Figure 3.3 (a), the scan rate was 10 mV/s, and the split wave phenomena associated with the rapid EC′ mechanism can be clearly observed in the voltammetry. Investigations were carried out to explore the effects of scan rate and as the rate increased the potential of the pre-wave shifted from 0.176 V (scan rate = 10 mV/s) to 0.288 V (scan rate = 200 mV/s). The peak potential had a good linearity against the square root of the scan rate (R = 0.99).

When the cysteine-FCA concentration ratio was increased to 1:1, in Figure 3.3 (b), the split wave was clearer and this trend was observed when the cysteine-FCA concentration ratio was increased further to 1.5:1, in Figure 3.3 (c). The current value of the pre-wave was closely equal or even larger than that of the oxidative process of the redox reaction. When the scan rate was higher than 80 mV/s, the current of the pre-wave exceeded the current of the oxidative process. In contrast, for the reductive process, the peak current decreased as the scan rate increased. When the L-cysteine was in a large excess (cysteine-FCA concentration ratio is 2:1), as Figure 3.3 (d) depicted, the effect of the catalytic reaction was stronger and exceeded the peak of the oxidative reaction, especially at large scan rate. However, the appearance of substrate did not affect the peak potentials of the redox reaction for both oxidative and reductive processes of FCA, which remained at 0.356 V and 0.283 V, respectively.

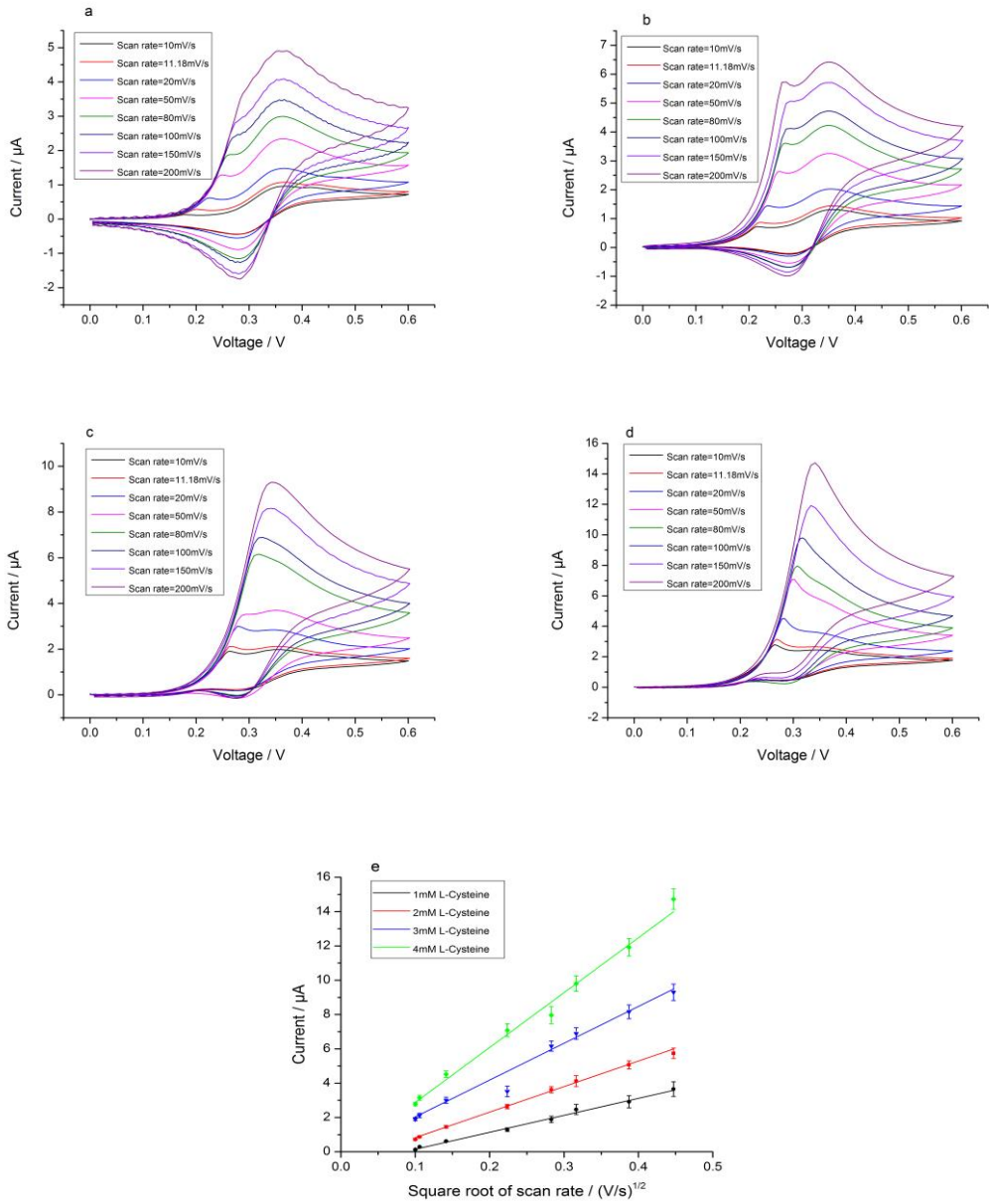

Figure 3.3 CV of electrocatalytic reaction with cysteine-FCA ratios (a) 1:2, (b) 1:1, (c) 1.5:1, (d) 2:1 with scan rates of 10, 11.18, 20, 50, 80, 100, 150, 200 mV/s; (e) the corresponding linear fit.

To understand how the electrochemical behaviour responded to the varying sulphide concentration, a concentrated L-cysteine solution was added to the 2 mM FCA aqueous solution (pH = 9.2 borate buffer solution, 0.1 M KCl) with the concentration gradient of 1 mM. In Figure 3.4 (a), the pre-wave shifted in a positive direction as the L-cysteine concentration became larger, from 0.226 V (at 1 mM L-cysteine) to 0.293 V (at 10 mM

L-cysteine). Correspondingly, the current value of the pre-wave was higher than the oxidative peak of the redox reaction when the L-cysteine concentration was over 3 mM. The peak current of the split wave varied as a linear function of the L-cysteine concentration (Figure 3.4 (b)) ($I_p/\mu A = 6.859 \times 10^{-7} \times$ [concentration of L-cysteine] + 2.533×10^{-7}, N = 10, R = 0.997). The current contribution of the catalytic reaction also exhibited a linear variation as a function of the L-cysteine concentration (Figure 3.4 (c)) ($I_p/\mu A = 4.603 \times 10^{-7} \times$ [concentration of L-cysteine] $+1.125 \times 10^{-6}$, N = 10, R = 0.994).

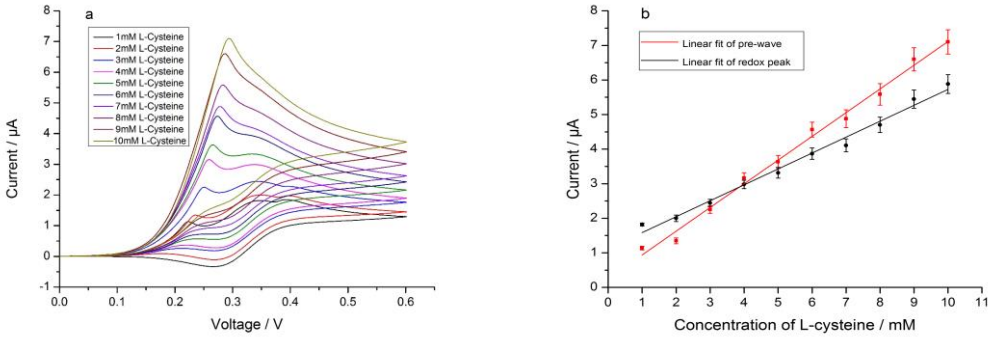

Figure 3.4 (a) CV of 2 mM FCA with various concentrations of L-cysteine (1, 2, 3, 4, 5, 6, 7, 8, 9, 10 mM) and scan rate 11.18 mV/s at the 1mm glassy carbon electrode; (b) linear calibration plot of pre-wave current (red) and oxidation peak current (black).

To understand the influence of the geometry of the electrode, the CV analysis of the EC′ reaction was carried out using a glassy carbon electrode with a larger surface area (3 mm in diameter). In Figure 3.5 (a), the redox peak potentials remained +0.356 V for the oxidation and +0.283 V for the reduction as a function of scan rate from 5 mV/s to 200 mV/s. This is in good agreement with the data recorded using the 1 mm glassy carbon electrode. The peak separation potential of oxidation and reduction was 73 mV, which was larger than the standard reversible peak separation potential 59/n mV. The reaction was regarded as quasi-reversible in nature for FCA. The function of peak current vs the square root of scan rate was in a linear relationship, as shown in Figure 3.5 (b).

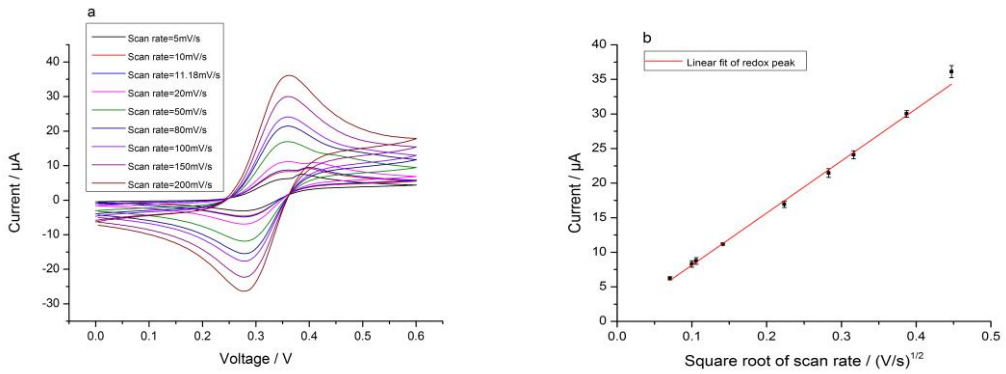

Figure 3.5 CV of 2 mM FCA in the absence of L-cysteine with various scan rates (5, 10, 11.18, 20, 50, 80, 100, 150, 200 mV/s) (a) at a 3 mm glassy carbon electrode;(b) linear fit of the peak current against the square root of the scan rate.

When the sulphide substrate was introduced into the electrolyte, in Figure 3.6, a split wave was observed in advance of the oxidative peak. The pre-wave shifted in an oxidative direction as the scan rate increased (scan rate: 5 – 150 mV/s). The peak shift of the split wave according to the scan rate can be explained as follows: the peak position of the pre-wave corresponded to the point where the L-cysteine on the electrode surface was totally consumed. When a fast scan rate was applied, less time was available for the electrode catalytic reaction to proceed due to the kinetic limitations. The oxidative shift of the pre-wave led to the merger of the current signal response of the catalytic reaction and oxidative processes so that the process moved from KT2 to KG* (Figure 1.15) as the scan rate increased[26]. The peak height of the pre-wave was a linear function of the square root of the scan rate, which corresponded well with the results of the 1mm glassy carbon electrode (which is not shown here). However, the potential of the redox reaction was not affected by the catalytic reaction, which remained +0.356 V and +0.283 V for oxidative and reductive peaks, respectively.

The electrochemical behaviour of the changing concentration of L-cysteine was then studied using a 3 mm glassy carbon electrode, as in Figure 3.7. The pre-wave shifted

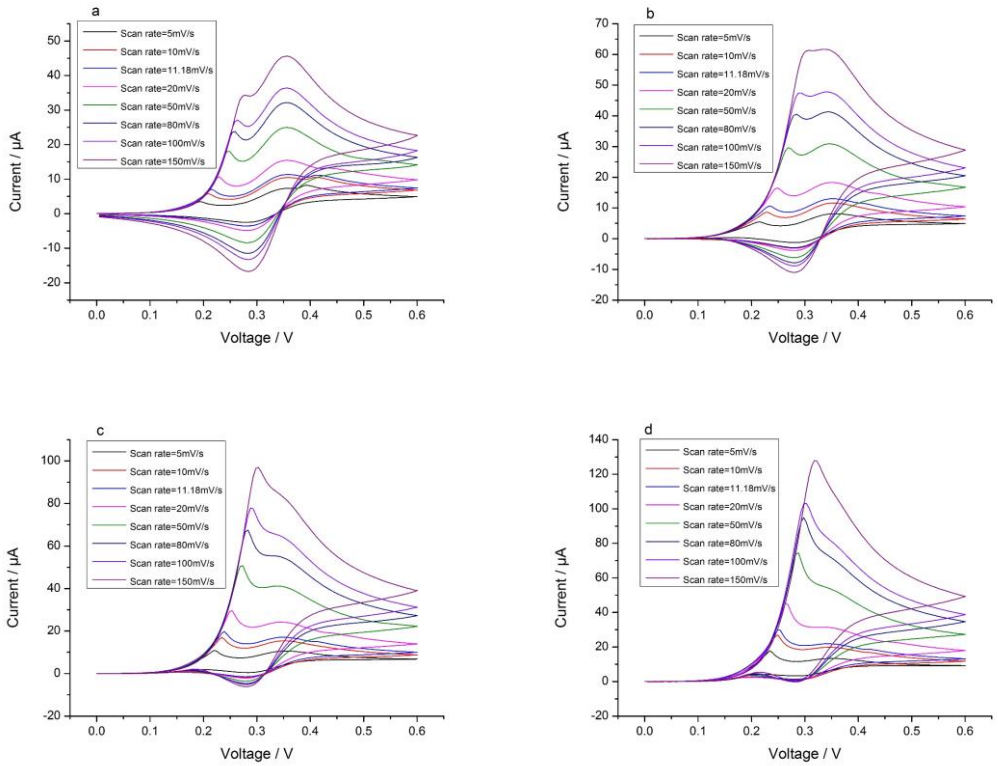

Figure 3.6 CV of the electrocatalytic reaction with cysteine-FCA ratio (a) 1:2, (b) 1:1, (c) 1.5:1, (d) 2:1 with scan rates of 5, 10, 11.18, 20, 50, 80, 100, 150 mV/s.

to an oxidative direction, which was from 0.224 V (at 1 mM L-cysteine) to 0.278 V (at 10 mM L-cysteine). This is analogous to the results obtained for the 1 mm glassy carbon electrode, the current associated with the pre-wave was a linear function of the L-cysteine concentration ($I_p/\mu A = 6.591 \times 10^{-6} \times$ [concentration of L-cysteine] $+ 2.408 \times 10^{-6}$, N = 10, R = 0.997), as depicted in Figure 3.7 (b). The current rise according to the substrate concentration was due to the current contribution from the oxidation of the regenerated FCA in the catalytic step. The peak current of the oxidative process of the redox reaction was a linear function of the L-cysteine concentration ($I_p/\mu A = 3.138 \times 10^{-6} \times$ [concentration of L-cysteine] $+ 7.690 \times 10^{-6}$, N = 10, R = 0.993), in Figure 3.7 (c). When the L-cysteine was in a large excess, the current response of the catalytic reaction merged with the current of the oxidative process and controlled the electrochemical behaviour of the system. The current value of the reductive peak,

however, kept decreasing and almost disappeared when the substrate concentration was 10mM, where the reaction moved from zone KT2 to zone K.

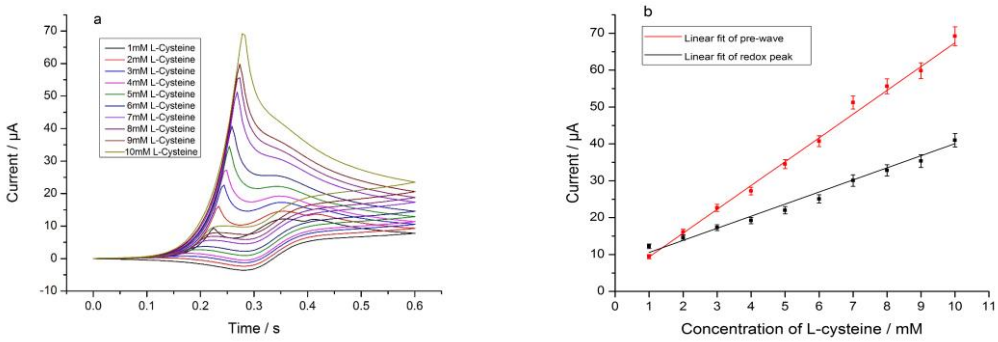

Figure 3.7 (a) CV of 2 mM FCA with various concentrations of L-cysteine (1, 2, 3, 4, 5, 6, 7, 8, 9, 10 mM) at scan rate 11.18 mV/s using a 3 mm glassy carbon electrode; (b) linear calibration plot of pre-wave current (red) and oxidation peak current (black).

3.3.2 FTACV investigation of the EC′ reaction of the ferrocene derivative and L-cysteine

Next, the FTACV was explored for the first time on an EC′ mechanistic system that exhibited split wave behaviour. The electrochemical characteristics of the EC′ mechanism were analysed using the first four harmonics within a potential range of 0–600 mV. The effects of the voltage amplitude and the sinusoidal frequencies on the observed current behaviour were explored and are reported below.

First, the reversible reaction of FCA (2 mM, 0.1 M KCl, pH = 9.2 borate buffer solution) was characterized using the 1 mm glassy carbon electrode. Experimental results displayed in a current-time form are shown in Figure 3.8 and were obtained with the following settings, scan rate: 11.18 mV/s, amplitude: 50 mV, potential range: 0–0.6 V, frequency: from 1 Hz to 6 Hz. For the fundamental harmonic component (Figure 3.8

(a)), the peak potentials of oxidation and reduction, converted from the current-time term, were at 0.318 V and 0.317 V, respectively, which were close to the average of oxidation and reduction peak potentials ($E_{1/2}$) obtained from CV, 0.32 V. The bell-shaped peaks of oxidation and reduction lay symmetrically around the $E_{1/2}$. When the frequency increased, the peak current increased, while the $E_{1/2}$ remained at the same potential and the shape of the reaction peaks did not vary. In the second harmonic component, as Figure 3.8 (b) shows, two peaks on both the oxidative and reductive processes were obtained. The peak height became larger as the frequency increased. For the third harmonic component (Figure 3.8 (c)), a main peak, whose potential was 0.318V, with two side peaks of equal height, were obtained on the oxidative and reductive process. For the fourth harmonic component, similar phenomena were observed in the Figure 3.8(d).

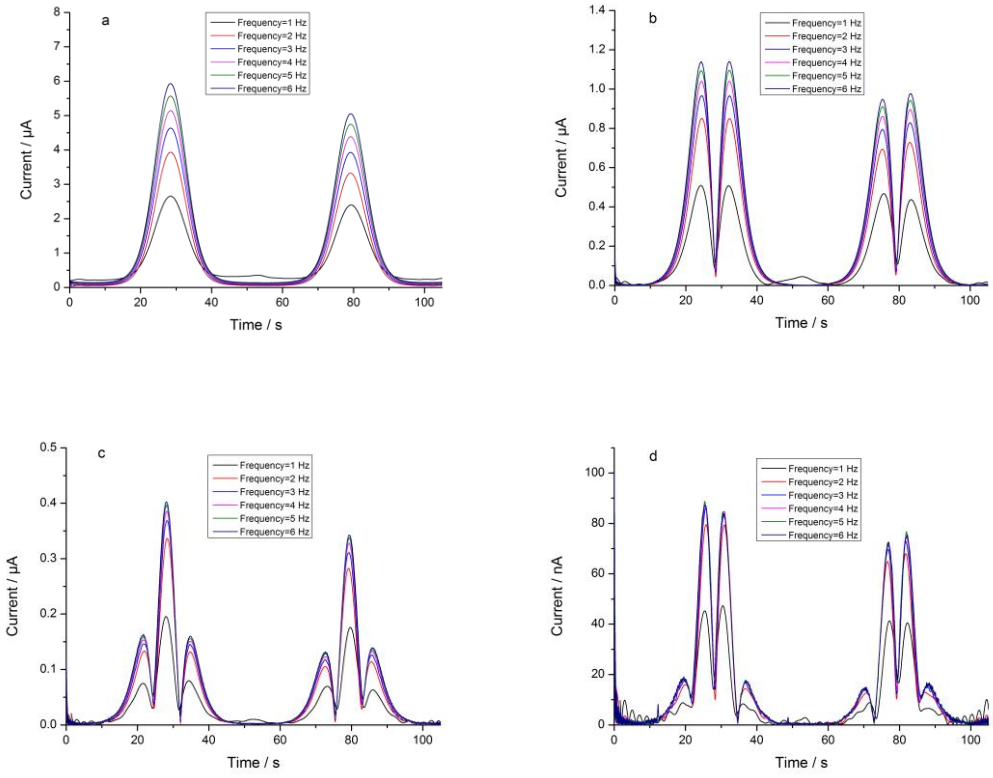

Figure 3.8 The FTACV of 2mM FCA in the absence of L-cysteine with various frequencies, scan rate: 11.18 mV/s, amplitude: 50 mV, potential range: 0–0.6 V, using 1mm glassy carbon electrode; (a) fundamental harmonic, (b) second harmonic, (c) third harmonic, (d) fourth harmonic.

The catalytic reaction was then introduced. The cysteine-FCA concentration ratio was 1:1. For the fundamental harmonic component (Figure 3.9(a)), an inflection related with the C' step was observed ahead of the oxidative peak. As the frequency increased, the inflection became weaker and disappeared when the frequency was over 3 Hz. The shape of the reductive peak, however, was not varied by the introduction of L-cysteine. For the second harmonic component (Figure 3.9 (b)), a small inflection was observed ahead of the first oxidative peak and decayed as the frequency increased.

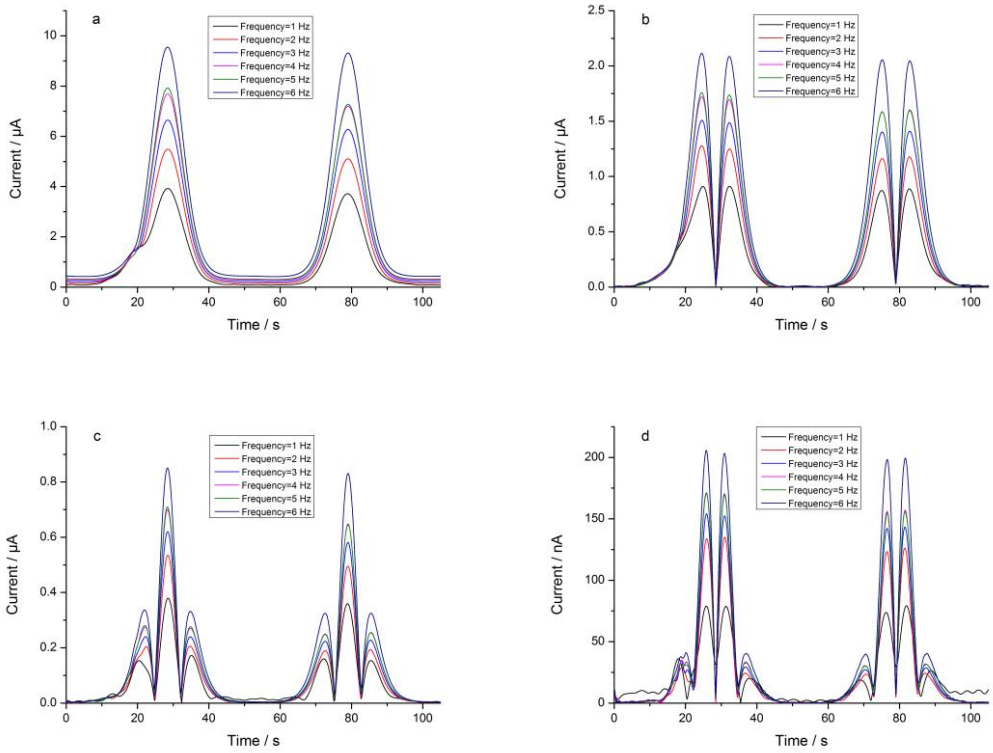

Figure 3.9 The FTACV of 2 mM FCA with 2 mM L-cysteine at various frequencies, scan rate: 11.18 mV/s, amplitude: 50 mV, potential range: 0–0.6V at a 1 mm glassy carbon electrode; (a) fundamental harmonic, (b) second harmonic, (c) third harmonic, (d) fourth harmonic.

When the frequency was over 5 Hz, the pre-wave disappeared. Different from the first harmonic, the frequency range for the second harmonic was larger and the baseline of the second harmonic remained at 0 due to avoidance of the capacitive background signal. In Figure 3.9 (c), the pre-wave became more apparent in the third harmonic component. The peak area of the first peak was larger than the third due to the current

contribution of the C' process. Similar phenomena were observed in the fourth harmonic (Figure 3.9 (d)).

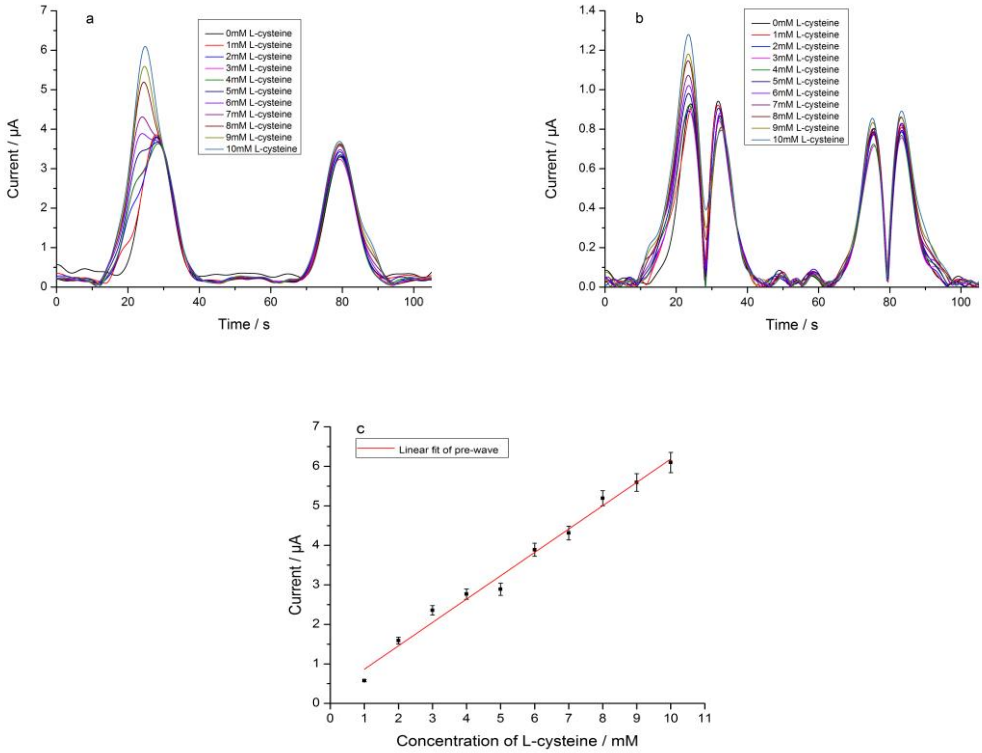

Figure 3.10 The FTACV of 2 mM FCA with various concentrations of L-cysteine at frequency 1 Hz, scan rate: 11.18 mV/s, amplitude: 50 mV, potential range: 0–0.6 V at a 1 mm glassy carbon electrode; (a) fundamental harmonic; (b) second harmonic; (c) linear fit of the pre-wave current of the fundamental harmonic component.

The effect of different cysteine-FCA concentration ratio was then studied with parameters: scan rate: 11.18 mV/s, amplitude: 50 mV, potential range: 0–0.6 V, frequency: 1 Hz. In Figure 3.10 (a), the height of the inflection increased as the concentration of L-cysteine rose and the pre-wave overtook the oxidation peak when the L-cysteine was in large excess. The peak current of the pre-wave behaved as a function of the cysteine concentration (I_{pp}/μA = 5.911 × 10^{-7} × [concentration of L-cysteine] + 2.747 × 10^{-7}, N = 10, R = 0.993), as Figure 3.10 (e) depicted. There was an inflection on the right bottom of the reductive peak in the fundamental harmonic component. The inflection became more apparent when the L-cysteine was in large excess. However, the potential of the redox peak remained at 0.32 V, which was not

affected by the strength of the catalytic reaction. For the second harmonic component, in Figure 3.10 (b), the inflection presented at the left bottom of the oxidation current and increased as more L-cysteine was added. The current contribution of the catalytic process was mainly at the first peak.

The electrochemical behaviour was then investigated using the 3 mm glassy carbon electrode. The parameters used were scan rate: 11.18 mV/s, amplitude: 70 mV, potential range: 0–0.6 V, frequency: 1–10 Hz. For the fundamental harmonic component, in Figure 3.11 (a), a symmetrical bell-shaped peak presented at 0.32 V for both the oxidative and negative scans. The peak potential was close to the half-wave potential $E_{1/2}$ obtained from CV. The $E_{1/2}$, which was a replacement of the standard potential due to the difficulty in achieving its detection, was important to identify the chemical species. When the frequency increased, not only the peak current but also the value of the baseline increased. The reason was as follows: the fundamental harmonic component was sensitive to both faradaic current and double-layer charging current C_{dl}. The increased frequency as the step scan rate was increased led to more cycles of forward–backward sweeps. As a result, the faradaic current rose. Even though C_{dl} has been minimized in the low-frequency condition, a small growth of C_{dl} with frequency increase could be observed on the baseline. For the second harmonic component (Figure 3.11 (b)), similar to the results of the 1 mm glassy carbon electrode, a pair of equal height peaks presented on both the forward and backward scans with the middle potential at 0.32 V. The equal heights of the two peaks meant the reversibility of the Fc/Fc^+ species. Because of the excellent elimination of the capacitive background current, the baseline of the second harmonic component was close to zero and did not vary with the frequency. Although the faradaic currents were small in value on the third and higher harmonics (Figure 3.11 (c–f)), the responses were not affected by the capacitive background current, in which case the background correction was not necessary.

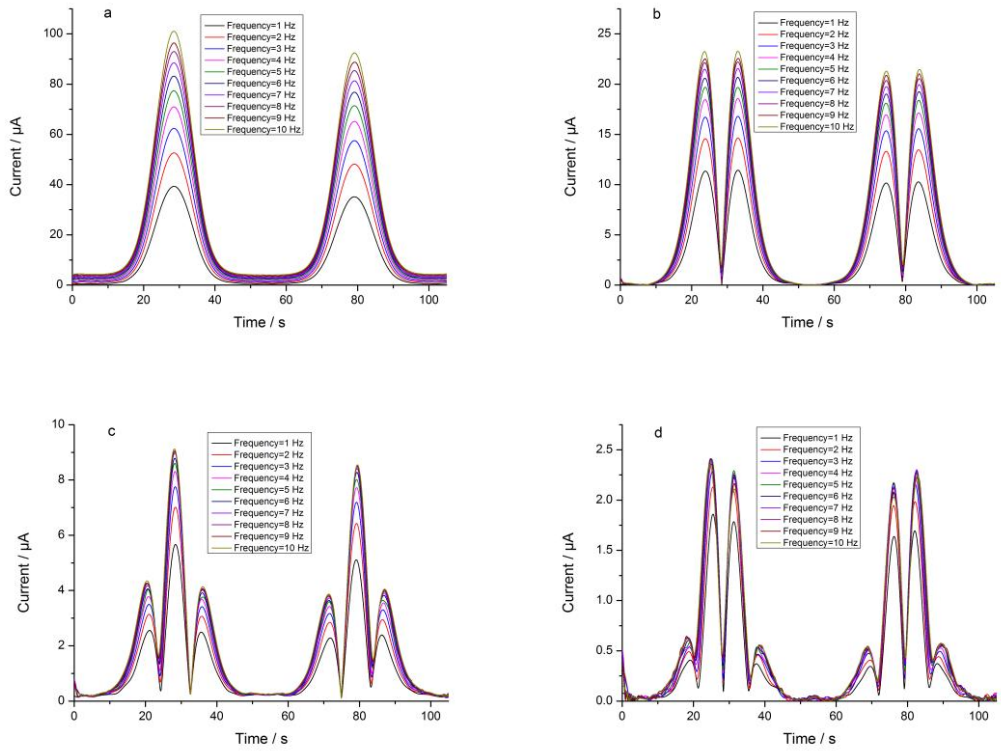

Figure 3.11 The FTACV of 2 mM FCA in the absence of L-cysteine with various frequencies, scan rate: 11.18 mV/s, amplitude: 70 mV, potential range: 0–0.6 V, at a 3 mm glassy carbon electrode; (a) fundamental harmonic; (b) second harmonic; (c) third harmonic; (d) fourth harmonic.

To understand the reaction of sulphide and Fc/Fc^+, L-cysteine with a concentration of 2 mM, 3 mM and 4 mM was added to the 2 mM FCA aqueous solution. The parameters used were scan rate: 11.18 mV/s, amplitude: 50 mV, potential range: 0–0.6 V, frequency: 1–10 Hz. When the cysteine:FCA concentration ratio was 1:1, an inflection appeared and decayed as the frequency increased for the fundamental harmonic component (Figure 3.12 (a)). At higher frequency, as the scan rate of the sinusoidal step scan rose, the chemical reaction was not fast enough to regenerate FCA that returned to the reversible reaction. As a result, the catalytic reaction was less influential compared with the redox reaction. Moreover, the $E_{1/2}$ remained at 0.32 V, which was not affected by the catalytic reaction. For the higher harmonic components, the pre-wave became more independent. For the second harmonic component, as Figure 3.12 (b) depicts, a split peak appeared at 0.208 V when the frequency was 1 Hz. As the frequency

increased, the pre-wave decayed but the potential remained at 0.208 V. For the third and higher harmonic components (Figure 3.12 (c, d)), the pre-wave became more independent due to the greater sensitivity to the faradaic components.

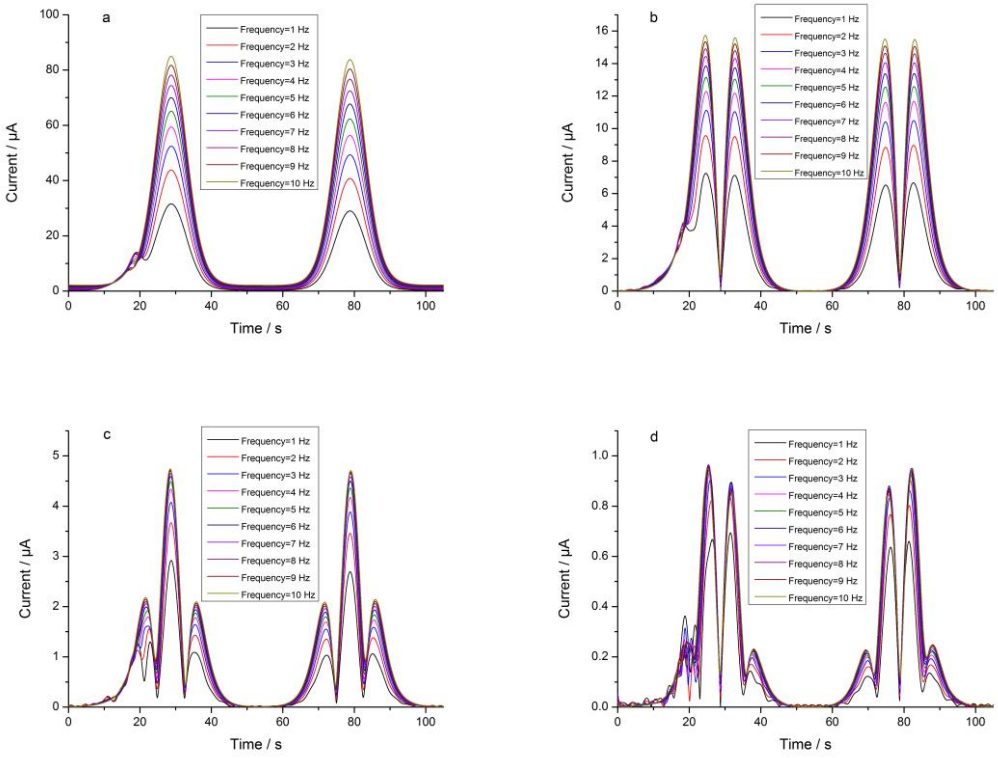

Figure 3.12 The FTACV of 2 mM FCA with 2 mM L-cysteine at various frequencies, scan rate: 11.18 mV/s, amplitude: 50 mV, potential range: 0–0.6 V at a 3 mm glassy carbon electrode; (a) fundamental harmonic; (b) second harmonic; (c) third harmonic; (d) fourth harmonic.

Figures 3.13 and 3.14 demonstrate the signal response when the cysteine-FCA ratio was larger, namely 1.5:1 and 2:1. At all harmonics, the ratio of the pre-wave height vs oxidative peak height decreased as the frequency increased. The explanation could be proposed as follows: (1) the ac sinusoidal potential induced the oxidative and reductive reactions, which enhanced redox peak values; (2) considering the single step of the sinusoidal wave, the increase of frequency led to a faster scan rate, however, the chemical reaction was not fast enough to regenerate FCA, which returned to the reversible reaction.

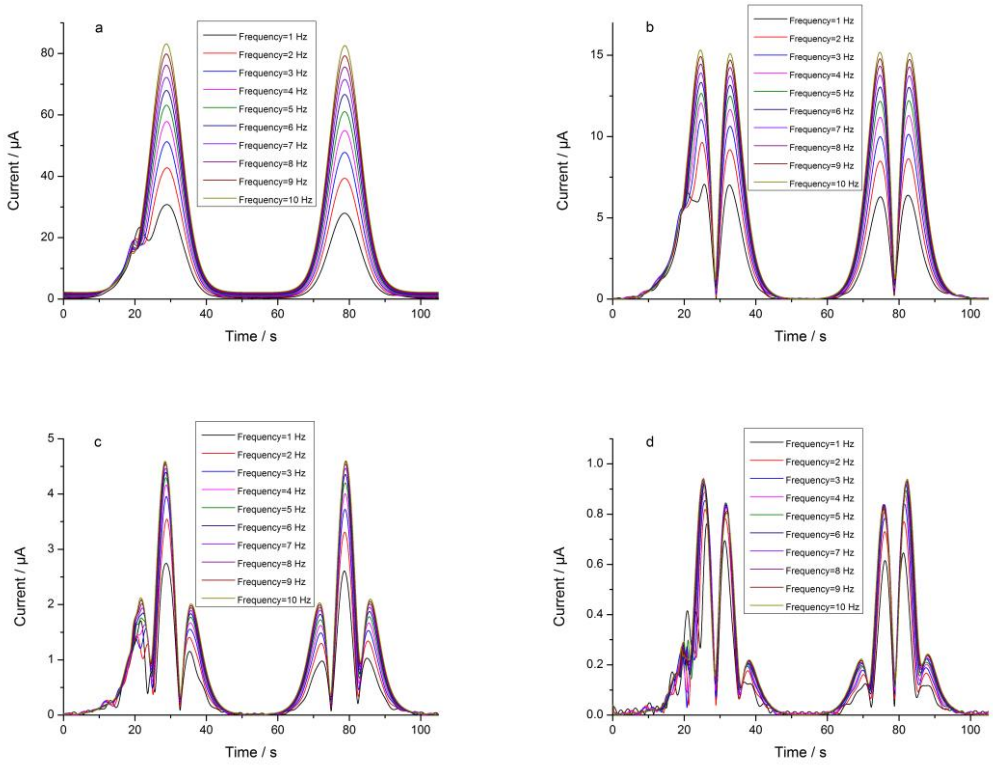

Figure 3.13 The FTACV of 2 mM FCA with 3 mM L-cysteine at various frequencies, scan rate 11.18 mV/s, amplitude: 50 mV, potential range: 0–0.6 V at the 3 mm glassy carbon electrode; (a) fundamental harmonic; (b) second harmonic; (c) third harmonic; (d) fourth harmonic.

To investigate the relationship of L-cysteine concentration and the electrochemical behaviour of the EC′ reaction, the frequency of 1 Hz was selected for the characterization. In Figure 3.15 (a), a clear split wave presented in advance of the oxidative peak. The pre-wave rose as a linear function of the L-cysteine concentration (I_{pp}/μA = 9.065 × 10^{-6} × [concentration of L-cysteine] – 3.194 × 10^{-6}, N = 4, R = 0.996), shown in Figure 3.15 (e). The oxidative peak, however, remained at 0.32 V. Moreover, the peak value was not influenced by the strength of the catalytic reaction, which was different from the results of the dc signal. For the second harmonic component, the influence of the catalytic reaction was mainly on the first peak of the oxidative reaction. The first peak decreased when the L-cysteine was in a large excess, as the positive shift and enhanced current area of the pre-wave led to the current sharing of the first peak of the oxidative reaction. Moreover, the elimination of the capacitive background on the second harmonic component led to a more accurate linear function of pre-wave value

vs the L-cysteine concentration. For the third harmonic component (Figure 3.15 (c)), the pre-wave became more independent from the oxidative peaks and the peak value was much larger than the third peak. When looking at the fourth harmonic component in Figure 3.15 (d), the pre-wave, which was only related to the catalytic reaction, separated as a single peak and rose as the L-cysteine increased. The first and second peaks of the oxidative reaction, however, were influenced by both the catalytic and redox reaction. The third and fourth peaks were free from the C′ step. This was a useful phenomenon that the result of FTACV can be separated into three parts for different uses: (1) pre-wave can be used for the C′ analysis and determining the substrate concentration; (2) the effect of C′ on the redox reaction can be investigated by the first and second peaks; (3) the fourth harmonic component can also separate the electrochemical behaviour of the pure reversible reaction.

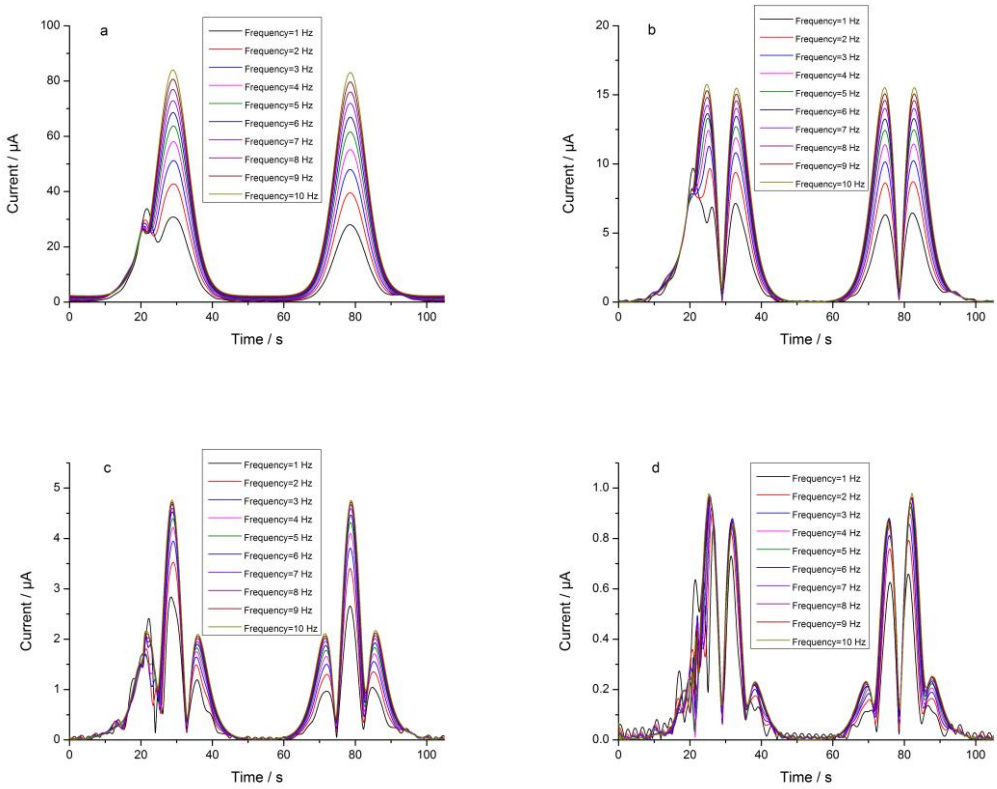

Figure 3.14 The FTACV of 2 mM FCA with 4 mM L-cysteine at various frequencies, scan rate: 11.18 mV/s, amplitude: 50 mV, potential range: 0–0.6 V at a 3 mm glassy carbon electrode; (a) fundamental harmonic; (b) second harmonic; (c) third harmonic; (d) fourth harmonic.

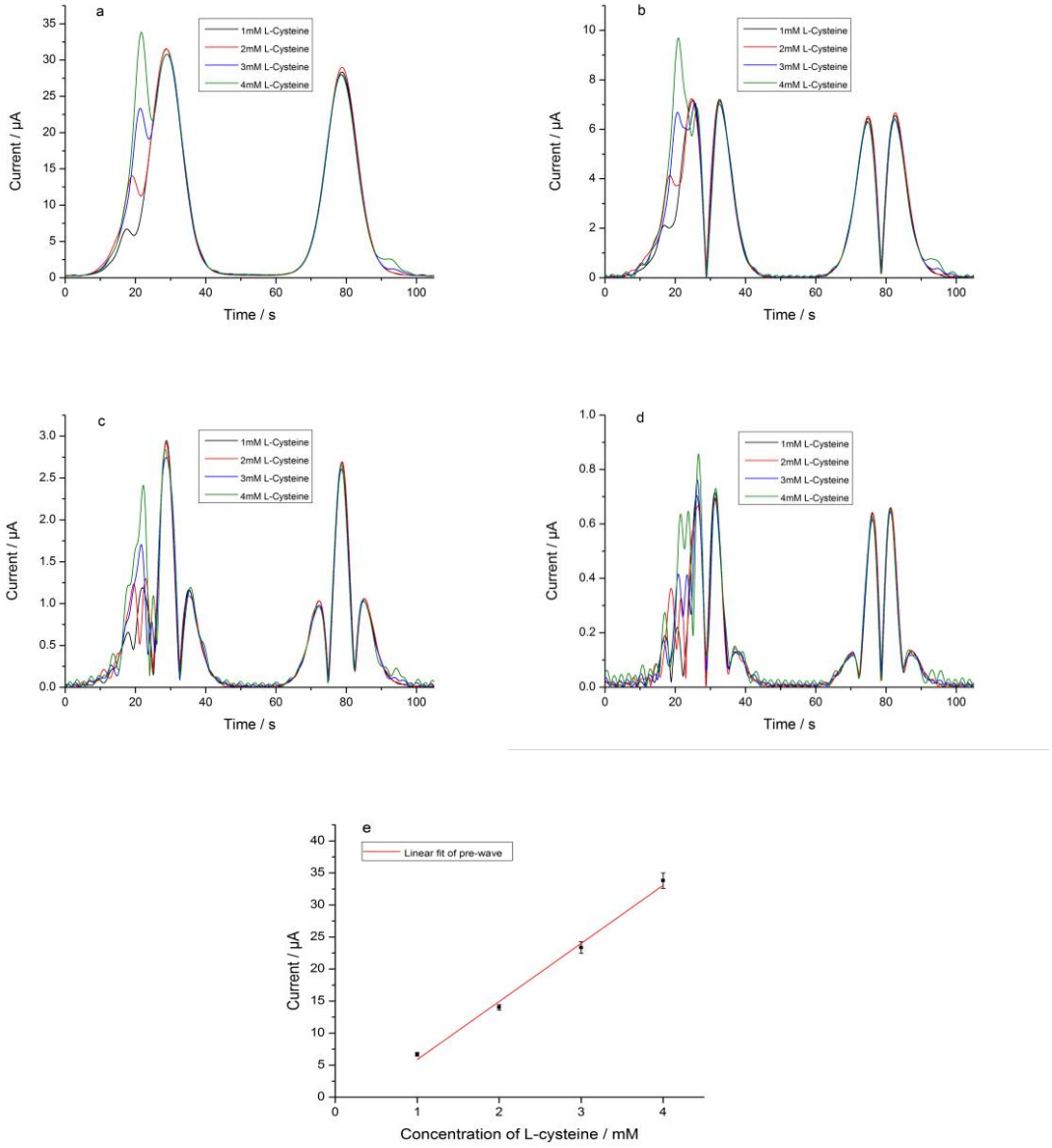

Figure 3.15 The FTACV of 2 mM FCA with various concentrations of L-cysteine at frequency 1 Hz, scan rate: 11.18 mV/s, amplitude: 50 mV, potential range: 0–0.6 V at a 3 mm glassy carbon electrode; (a) fundamental harmonic; (b) second harmonic; (c) third harmonic; (d) fourth harmonic; (e) linear fit of the pre-wave current of the fundamental harmonic component.

3.4 Numerical simulation of the EC′ mechanism using FTACV

To understand the effects of frequency and substrate-mediator ratio on the electrochemical behaviour of the EC′ process, a numerical simulation using a model developed by H. V. Nguyen in this section, was employed theoretically to support the experimental results. By using the large-amplitude sinusoidal ac signal inputs, components of the harmonic information were separated from the raw output by employing a fast Fourier transform model. The parameters used in this section were the amplitude of 50 mV, scan rate of 10 mV/s and macrodisc electrode with surface area 10^{-6} m^2.

Figure 3.16 details the current response of the EC′ mechanism with the following parameters, substrate:mediator ratio: 1:1, frequency: 1-6 Hz, diffusion coefficient of FCA: 7.6×10^{-6} cm^2/s, kinetics for the catalytic reaction: 1000 mol/m^3. For the fundamental harmonic component, as shown in Figure 3.16 (a), pre-waves, which were dependent on the oxidation of the substrate, presented at the bottom of the peak in the forward scan. The pre-wave became less obvious and disappeared when the frequency increased. Moreover, as the current behaviour of the first harmonic was composed of a capacitive background and faradaic response, the baseline related with the capacitance on the electrode surface presented a positive correlation with the frequency. The numerical results corresponded with the result achieved in the experiment. For the second harmonic component, in Figure 3.16 (b), the pre-wave of the catalytic reaction appeared before the redox peak and decayed as the frequency rose. However, the $E_{1/2}$ did not vary with the frequency. As the third and fourth harmonic components were more sensitive to the faradaic response, the pre-wave behaved as a more independent inflection and the growth of the first peak was significant in Figure 3.16 (c) and (d). Similarly, the $E_{1/2}$ that related with the redox couple remained at the same potential.

When the substrate:mediator concentration ratio increased, such as 2:1 and 4:1, in Figures 3.17 and 3.18, stronger split waves presented in the forward scan. Similarly, the pre-wave became less obvious when the frequency increased.

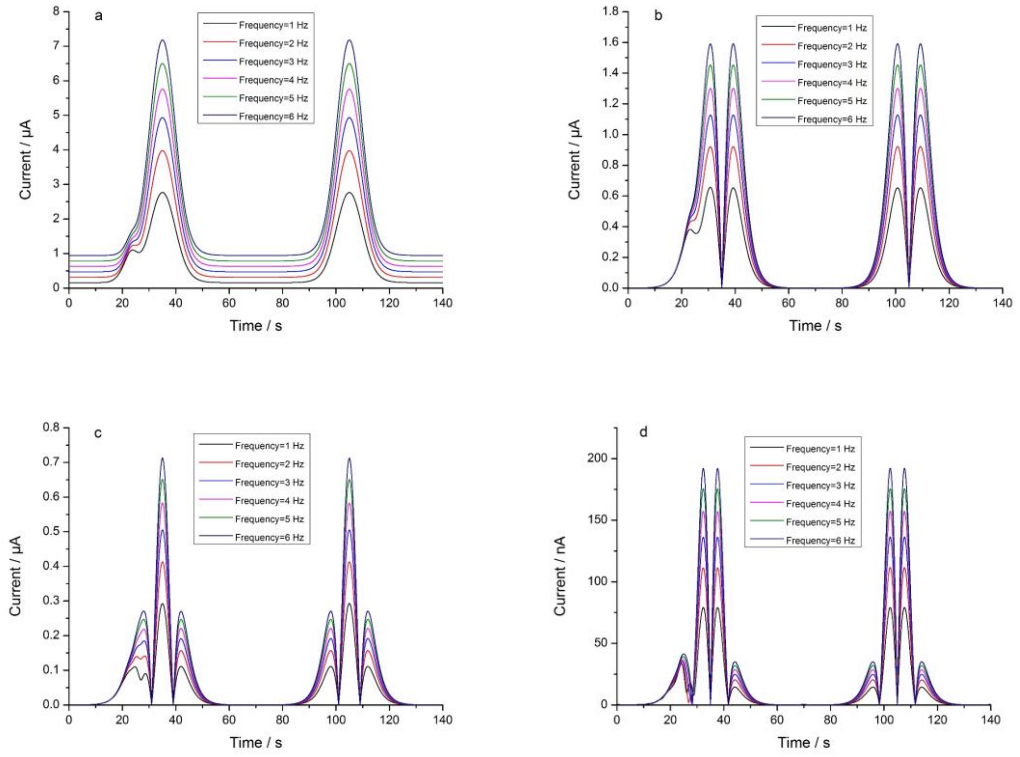

Figure 3.16 Simulation of the FTACV of 2 mM FCA against L-cysteine 1:1 with various frequencies, scan rate: 10 mV/s, amplitude: 50 mV, potential range: –0.1 to 0.6 V at a 1 mm disc; (a) fundamental harmonic; (b) second harmonic; (c) third harmonic; (d) fourth harmonic.

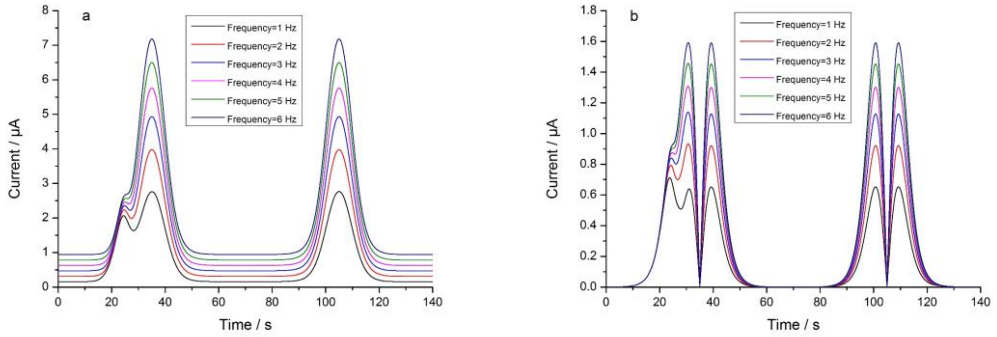

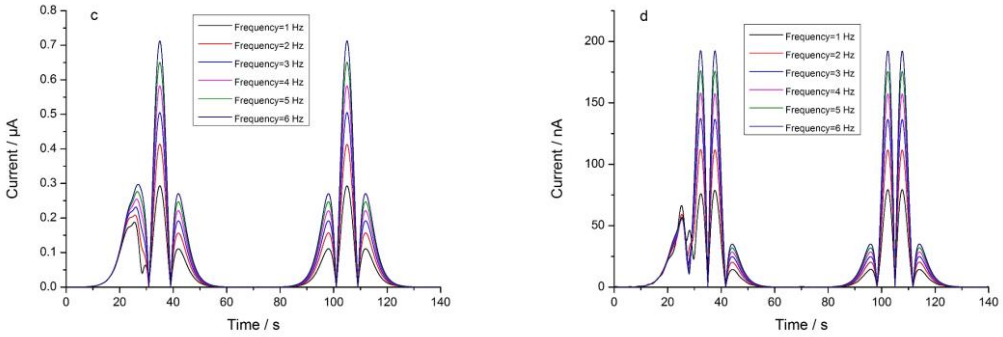

Figure 3.17 Simulation of the FTACV of 2 mM FCA against L-cysteine 1:2 with various frequencies, scan rate: 10 mV/s, amplitude: 50 mV, potential range: –0.1 to 0.6 V at a 1 mm disc; (a) fundamental harmonic; (b) second harmonic; (c) third harmonic; (d) fourth harmonic.

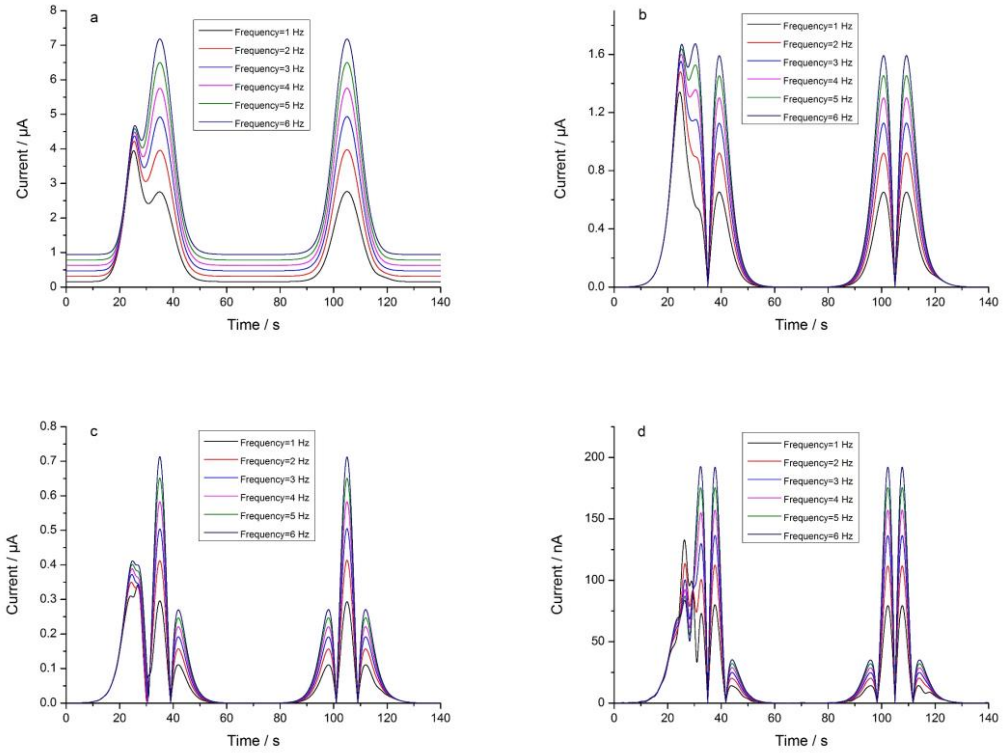

Figure 3.18 Simulation of the FTACV of 2 mM FCA against L-cysteine 1:4 with various frequencies, scan rate: 10 mV/s, amplitude: 50 mV, potential range: –0.1 to 0.6 V at a 1 mm disc; (a) fundamental harmonic; (b) second harmonic; (c) third harmonic; (d) fourth harmonic.

The effect of substrate:mediator ratio on the current behaviour was then simulated when the frequency was 1 Hz, in Figure 3.19. For the fundamental harmonic component, in Figure 3.19 (a), the pre-wave increased as more substrate was introduced into the system. The peak current of the split wave varied as a linear function of the substrate:mediator ratio in Figure 3.19 (e). When the substrate was in large excess, the pre-peak became much higher than the oxidative peak and a small inflection related to homogeneous chemical reaction presented at the bottom of the reductive peak. These phenomena supported the experimental results. The appearance of a reductive inflection can be explained as follows: (1) the substrate on the electrode surface was not totally consumed in the forward scan; (2) the reciprocating sinusoidal signal induced the catalytic reaction, which regenerated the FCA. Moreover, for the fundamental harmonic component, the redox peak was not varied by the catalytic reaction. In the second harmonic, as Figure 3.19 (b) depicts, when the substrate:mediator concentration increased, the pre-wave greatly increased, which even affected the behaviour of the first redox peak. For the third and higher harmonic components in Figure 3.19 (c) and (d), the high sensitivity of detecting the faradaic component and elimination of the capacitive component made them ready for precise analysis. Moreover, the pre-wave in the fourth harmonic component was only caused by the catalytic step; the first and second peaks were the combination of the C′ and E steps as the first peak grew greatly with the substrate concentration; the third and fourth peaks were free from the effect of the C′ reaction.

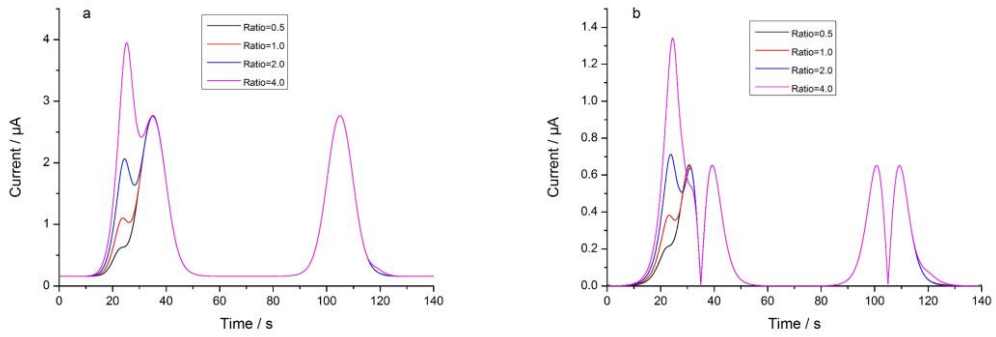

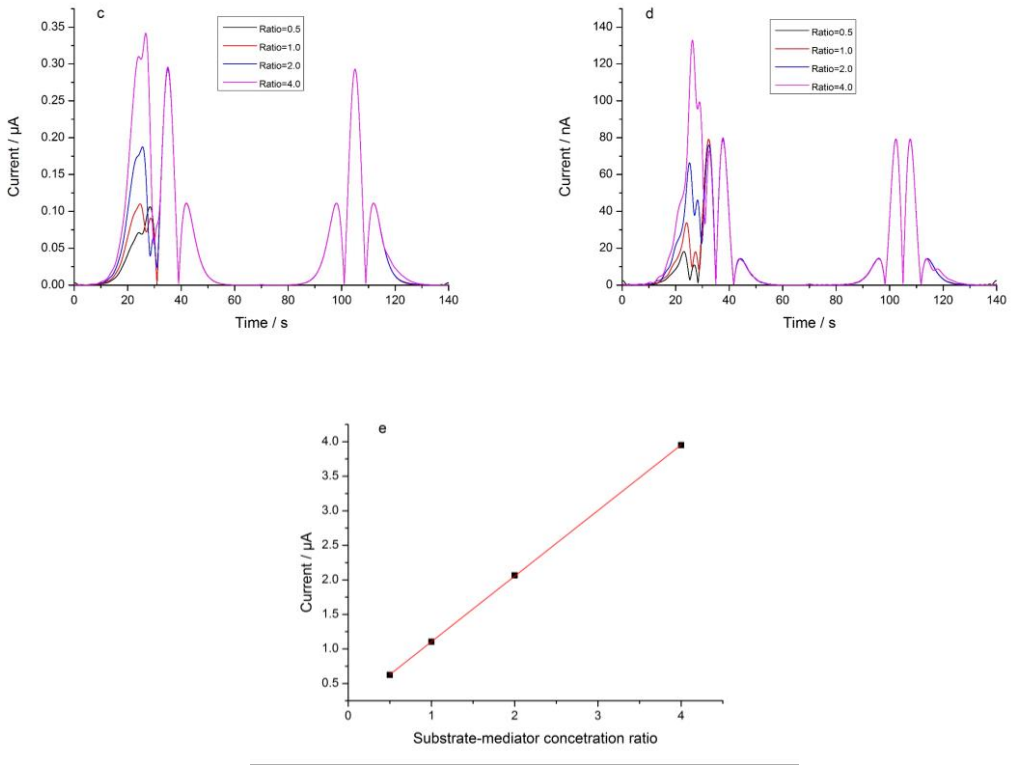

Figure 3.19 Simulation of the FTACV of 2mM FCA with various concentrations of substrate, frequency: 1 Hz, scan rate: 10 mV/s, amplitude: 50 mV, potential range: –0.1 to 0.6 V at a 1 mm disc (a) fundamental harmonic; (b) second harmonic; (c) third harmonic; (d) fourth harmonic.

3.5 Conclusions

In this chapter, the EC′ mechanism for sulphide detection was investigated at macro-electrodes using CV and FTACV. Split waves, related with the chemical reaction with sulphide, were observed in both CV and FTACV under certain conditions. In the dc CV, as the kinetics of heterogeneous electron transfer were fixed, the presence of pre-waves was dependent on the scan rate and the concentration of L-cysteine. The height of the pre-waves and the original peaks were linear functions of the sulphide concentration, which provided the possibility for quantitative detection of sulphide species by utilising the electrocatalytic mechanism in aqueous solution.

FTACV was utilized to study the EC′ mechanism for the first time. One advantage of FTACV is that it is possible to obtain ample information in a short time as its input signal is composed of a dc signal and ac sinusoidal signal. As the harmonic component was higher, FTACV was more sensitive to present the reaction of sulphide. At second and higher harmonic components, the separation of capacitive components allows FTACV to present pure kinetic components. Another advantage is that FTACV gives an accurate determination of potential, such as half-wave potential and pre-wave potential. The concentration of L-cysteine influenced the position of the pre-wave but did not affect the current behaviour of the redox reaction. In the fundamental harmonic component, the peak value of the pre-wave was a linear function of the L-cysteine concentration. As such, FTACV as a novel electrochemical method could be employed effectively to obtain in-depth information in a short period of time.

Reference

1. Lawrence, N.S., J. Davis, and R.G. Compton, *Analytical strategies for the detection of sulfide: a review.* Talanta, 2000. **52**(5): p. 771-784.
2. Executive, H.a.S., *Managing hydrogen sulphide detection offshore.* Offshore Information Sheet No. 6/2009, 2009.
3. Arya, S.P., M. Mahajan, and P. Jain, *Non-spectrophotometric methods for the determination of Vitamin C.* Analytica Chimica Acta, 2000. **417**(1): p. 1-14.
4. Li, J., et al., *Removals of aqueous sulfur dioxide and hydrogen sulfide using CeO2-NiAl-LDHs coating activated carbon and its mix with carbon nano-tubes.* Colloids and Surfaces A: Physicochemical and Engineering Aspects, 2015. **476**: p. 90-97.
5. Sathyadevi, P., et al., *Reaction-based epoxide fluorescent probe for in vivo visualization of hydrogen sulfide.* Biosensors and Bioelectronics, 2015. **68**: p. 681-687.
6. Haddad, P.R. and A.L. Heckenberg, *Trace determination of sulfide by reversed-phase ion-interaction chromatography using pre-column derivatization.* Journal of Chromatography A, 1988. **447**: p. 415-420.
7. Adegoke, O.A., *An overview of applications of pre-column derivatization reactions for the liquid chromatographic analysis of pharmaceuticals and other compounds.* African Journal of Pure and Applied Chemistry, 2012. **6**(14).
8. Robb, D.B., T.R. Covey, and A.P. Bruins, *Atmospheric Pressure Photoionization: An Ionization Method for Liquid Chromatography−Mass Spectrometry.* Analytical Chemistry, 2000. **72**(15): p. 3653-3659.
9. Hobbs, P.J., T.H. Misselbrook, and B.F. Pain, *Assessment of Odours from Livestock Wastes by a Photoionization Detector, an Electronic Nose, Olfactometry and Gas Chromatography-Mass Spectrometry.* Journal of Agricultural Engineering Research, 1995. **60**(2): p. 137-144.
10. Schiavon, G., et al., *Electrochemical Detection of Trace Hydrogen Sulfide in Gaseous Samples by Porous Silver Electrodes Supported on Ion-Exchange Membranes (Solid Polymer Electrolytes).* Analytical Chemistry, 1995. **67**(2): p. 318-323.
11. Jeroschewski, P., et al., *Galvanic sensor for determination of hydrogen sulfide.* Electroanalysis, 1994. **6**(9): p. 769-772.
12. Jiang, L., et al., *Methods and apparatus for the measurement of hydrogen sulphide and thiols in fluids*. 2006.
13. Lawrence, N.S., R.P. Deo, and J. Wang, *Electrochemical determination of hydrogen sulfide at carbon nanotube modified electrodes.* Analytica Chimica Acta, 2004. **517**(1–2): p. 131-137.
14. Prodromidis, M.I., P.G. Veltsistas, and M.I. Karayannis, *Electrochemical Study of Chemically Modified and Screen-Printed Graphite Electrodes with*

[SbVO(CHL)2]Hex. Application for the Selective Determination of Sulfide. Analytical Chemistry, 2000. **72**(17): p. 3995-4002.
15. Jeroschewski, P., C. Steuckart, and M. Kühl, *An Amperometric Microsensor for the Determination of H2S in Aquatic Environments.* Analytical Chemistry, 1996. **68**(24): p. 4351-4357.
16. Banks, C.E., et al., *Exploring Alkylated Ferrocene Sulfonates as Electrocatalysts for Sulfide Detection.* Electroanalysis, 2007. **19**(24): p. 2518-2522.
17. Hart, J.P. and A.K. Abass, *A disposable amperometric gas sensor for sulphur-containing compounds based on a chemically modified screen printed carbon electrode coated with a hydrogel.* Analytica Chimica Acta, 1997. **342**(2): p. 199-206.
18. Raoof, J.-B., R. Ojani, and H. Beitollahi, *L-Cysteine Voltammetry at a Carbon Paste Electrode Bulk-Modified with Ferrocenedicarboxylic Acid.* Electroanalysis, 2007. **19**(17): p. 1822-1830.
19. Lawrence, N.S., *Amperometric Detection of Sulfide: An Electrocatalytic Reaction with Ferrocene Carboxylate.* Electroanalysis, 2006. **18**(17): p. 1658-1663.
20. Martelli, A., et al., *Arylthioamides as H2S Donors: l-Cysteine-Activated Releasing Properties and Vascular Effects in Vitro and in Vivo.* ACS Medicinal Chemistry Letters, 2013. **4**(10): p. 904-908.
21. Lee, P.T., et al., *Selective electrochemical determination of cysteine with a cyclotricatechylene modified carbon electrode.* Analyst, 2015. **140**(1): p. 236-242.
22. Lawrence, N.S., et al., *Amperometric Detection of Sulfide at a Boron Doped Diamond Electrode: The Electrocatalytic Reaction of Sulfide with Ferricyanide in Aqueous Solution.* Electroanalysis, 2002. **14**(7-8): p. 499-504.
23. Nekrassova, O., et al., *The Oxidation of Cysteine by Aqueous Ferricyanide: A Kinetic Study Using Boron Doped Diamond Electrode Voltammetry.* Electroanalysis, 2002. **14**(21): p. 1464-1469.
24. Raoof, J.B., R. Ojani, and M. Kolbadinezhad, *Electrocatalytic Characteristics of Ferrocenecarboxylic Acid Modified Carbon Paste Electrode in the Oxidation and Determination of L-Cysteine.* Electroanalysis, 2005. **17**(22): p. 2043-2051.
25. Bartlett, P.N. and K.F.E. Pratt, *A study of the kinetics of the reaction between ferrocene monocarboxylic acid and glucose oxidase using the rotating-disc electrode.* Journal of Electroanalytical Chemistry, 1995. **397**(1): p. 53-60.
26. Rountree, E.S., et al., *Evaluation of Homogeneous Electrocatalysts by Cyclic Voltammetry.* Inorganic Chemistry, 2014. **53**(19): p. 9983-10002.

Chapter 4 Detection of the split wave of EC′ mechanism at steady state on a microelectrode

4.1 Introduction

Because of the small size and enhanced mass transport, microelectrodes have been widely used to investigate mechanisms and kinetics in electrochemistry. The electrochemical signal obtained is widely accepted with the advantages of high signal-to-noise ratios, enhanced mass transport, large temporal resolution, decreased charging currents and low disturbance by the solution resistance[1], in which case the microelectrode could be developed to meet the needs of sulphide detection.

In this chapter, the voltammetric behaviour of the reaction with sulphide was extended to microelectrode studies. In the case of dc measurements, when the steady state was achieved on microdisc carbon and gold electrodes, the split wave phenomena were explored. These studies were then extended to the FTACV measurements and the split waves were achieved for the first time, which not only proves the possibility of the FTACV in sulphide detection but also presents how the current of the EC′ mechanism behaves when a large-amplitude perturbation is superimposed. To support the interpretation of the experimental observations, a numerical simulation model of the steady state was developed.

4.2 The application of a microelectrode to sulphide detection

One type of sulphide microgas sensor is based on the structure of amperometric Clark sensors that were originally developed to measure oxygen concentration[2]. The Clark sensor is composed by the electrolyte and a two-electrode system, namely, a working electrode and a reference electrode. To improve the sensitivity, a gas-permeable membrane is used to separate the gas and electrode, in which case the effect of fouling on the electrode is reduced. Modification and development of Clark sensors has enhanced the portability and sensitivity. Diethyl-*p*-phenylenediamine (DEPD) is used as a reactant by reacting with sulphide to analyse the hydrogen sulphide[3, 4]. In addition, in comparison with the conventional macroelectrode Clark cell, the improved cell with a microelectrode enables its analytical parameters to be independent of the membrane due to the smaller diffusion layer associated with the microelectrode. The decrease in thickness of the diffusion layer avoids the diffusion layer impinging on the membrane (Figure 4.1). As a result, the microelectrode in the design obviates the need for membrane calibration and simplifies the use of Clark cells in measurements[4].

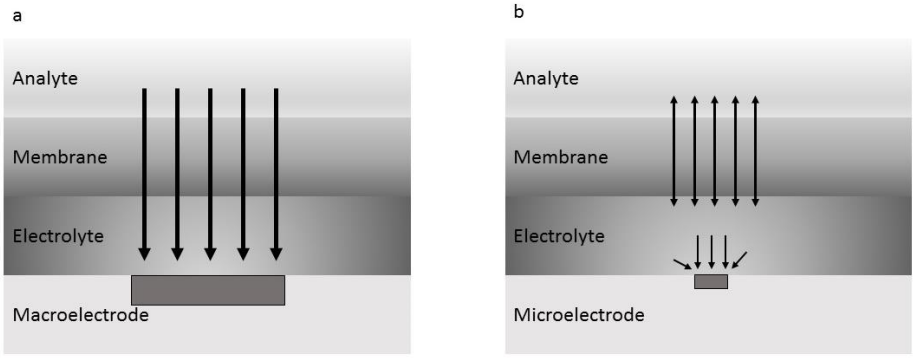

Figure 4.1 Clark cell of (a) conventional design and (b) improved design for membrane independence.

For some situations, the in-situ measurements are necessary as the sulphide is easily oxidised to sulphate by oxidants. Figure 4.2 depicts the schematic structure of the

commercial hydrogen sulphide gas sensor. The electrodes are immersed in a concentrated aqueous acid or salt solution to enhance conduction of ions. Gas enters the device through a membrane that is impermeable to liquid. The literature reports that mercury-coated metal substrate microelectrodes (such as gold, platinum and silver microdiscs) present good reproducibility and stability in sulphide detection[5-8]. For the quantitative determination of gas-phase hydrogen sulphide, a solid-polymer electrolyte (SPE) electrochemical sensor using a Pt electrode was tested for a quantitative determination in a mixed-gas condition (hydrogen sulphide and nitrogen) in laboratory conditions. Its high sensitivity (±1 ppm), fast response (10 s) and satisfactory linearity in the range of 0–100 ppm proved to have the potential for practical application in the field[9, 10]. For the SPE-gold electrode with pre-treated Nafion membrane, its detectability can even reach 0.1 ppm with response time of 9 s due to the enhanced selectivity of the gold electrode to the hydrogen sulphide[11].

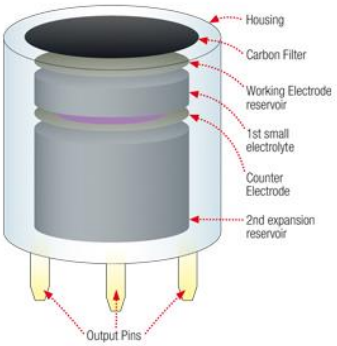

Figure 4.2 Structure of H_2S gas sensors[12].

The H_2S microsensor based on the EC′ mechanism has been commercialised and applied in environmental monitoring and biotechnology. The miniaturized amperometric sensor is composed of three microelectrodes: working, reference and counter electrodes. When the H_2S is passed into the alkaline electrolyte, the formed HS^- is oxidised by ferricyanide ion. The ferrocyanide/ferricyanide redox couple has been reported and commercialised to act as the mediator in the detection of hydrogen sulphide[13]. A schematic structure of the microsensor manufactured by Unisense is

depicted in Figure 4.3. By measuring the current response of the ferrocyanide/ferricyanide redox mediator, the concentration of H_2S can be determined. Small sample amount and fast response time of the measurement are the two advantages[14]. Rather than the metal electrodes, microelectrodes made of boron-doped diamond, carbon material and a modified surface have also been investigated to detect sulphide with the EC′ path[15].

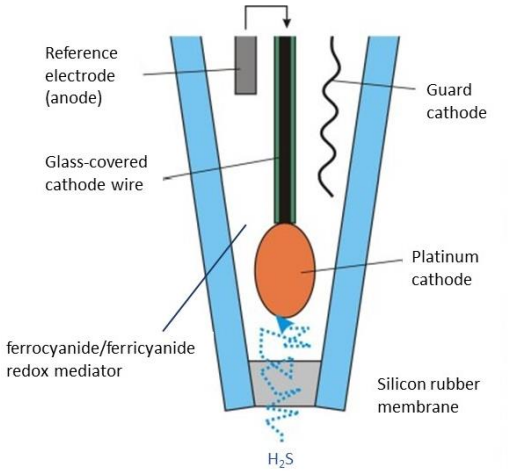

Figure 4.3 Schematic of ferrocyanide/ferricyanide H_2S microsensor.

Different from the electrochemical behaviour on the macroelectrode, a plateau rather than a peak current is achieved on the microelectrode under certain circumstance. The plateau current means a steady state is achieved on the microelectrode, which is more independent of the effects of the uncompensated resistance, capacitance and interference from instruments[16]. The microband, micro-disc and micro-rings are the three main types of microelectrodes. Different shapes of the microelectrode due to the difference in edge effect are used to describe the microelectrode effects of mass transport[17]. To understand better the effect of mass transport on the electrode surface and the kinetics of chemical reactions, many numerical simulations have been performed. Based on the original electrochemical models, a second-order kinetics model is considered and developed to derive the steady state current of the EC′

reaction[18, 19]. However, there is a simplified approximation to reduce the calculation of the reaction–diffusion mechanism. If the substrate concentration is in large excess, the catalytic step can be assumed as pseudo-first order, where the current behaviour is easily described by the linear equation related to the concentration of redox couple in the system[20, 21]. There are many papers reporting the use of pseudo-first-order models to investigate the conditions, such as electrode geometry and concentration of substrate, of the EC′ mechanism under a steady state.

4.3 Results and discussion

4.3.1 Oxidation of L-cysteine with aqueous ferrocene derivatives at a carbon fibre electrode

Initial CV studies were carried out using an aqueous solution of 2 mM FCA dissolved in borate buffer solution (pH = 9.2) with 0.1 M KCl as the supporting electrolyte using a 33 μm carbon fibre electrode. In Figure 4.4 (a), the peak-shaped current became a plateau and a sigmoidal-shape response was obtained. The half-wave potential $E_{1/2}$ achieved at steady-state condition was 0.319 V (at scan rates 5, 10, 11.18, 20 mV/s), which corresponded with the $E_{1/2}$ obtained from CV (0.320 V) and the FTACV (0.318 V) using the macroelectrodes in Chapter 3. To give a clear demonstration of steady-state current behaviour, the current response of 5 mV/s is depicted separately in Figure 4.4 (b). The limiting steady-state plateau current was 7.35 nA. The diffusion coefficient of FCA was $(5.16 \pm 0.05) \times 10^{-6}$ cm^2 s^{-1}, which is in good agreement with the results obtained in Chapter 3. The wave width expressed by the term, $E_{1/4} - E_{3/4}$, was 63 mV. The function of $\log[i/(i_{ss} - i)]$ vs voltage in the potential range of $E_{1/4}$ to $E_{3/4}$ was obtained from the scan rate of 5, 10 and 11.18 mV/s in Figure 4.4 (c). The slope was 64.0 ± 0.5 mV, which revealed a good linearity under steady-state conditions.

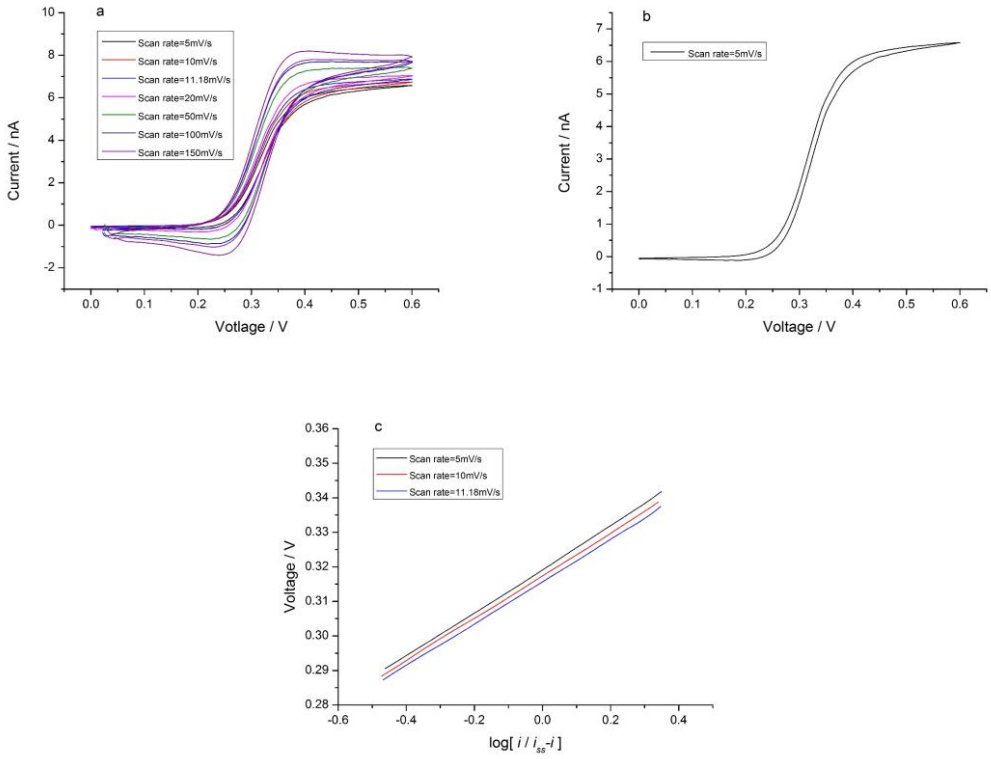

Figure 4.4 *i–E* response of 2 mM FCA at 33 μm carbon fibre (a) at scan rates of 5, 10, 11.18, 20, 50, 80, 100, 150, 200 mV/s; (b) at 5 mV/s at steady state; (c) linear function of voltage against log[$i/(i_{ss} - i)$] for *i–E* curves.

L-cysteine was then introduced into the 2 mM FCA aqueous solution with cysteine-FCA concentration ratio 1:2. The dc response was recorded using the same carbon fibre electrode. Figure 4.5 (a) shows the current enhancement resulting from the catalytic reaction involving FCA^+ and L-cysteine. The pre-wave characteristics were clearly observed, and in line with microelectrode measurements showed a steady-state-like form with the inflection observed before the plateau and decayed with decreasing scan rate.

When the cysteine-FCA concentration ratio was increased to 1:1 (Figure 4.6) and 2:1 (Figure 4.7), the current response of the reduction reaction more closely retraced the current of the oxidation process. Figure 4.6 (a) shows a clear plateau present when the

scan rate was varied from 5 mV/s to 150 mV/s. The limiting current grew from 10.0 nA (at 5 mV/s) to 16.2 nA (at 150 mV/s) as the scan rate increased. This behaviour can be rationalised in terms of the movement across the kinetic zones from KT (with 2 mM L-cysteine) to K [22] (with 4 mM L-cysteine). The cysteine concentration for entering the K zone on the microelectrode system was much lower than the cysteine concentration on the macroelectrode (10 mM). This phenomenon was due to the larger mass transport efficiency on the microelectrode surface. Figure 4.6 (b) and 4.7 (b) depicts the current response when the system approached the steady state at scan rate 5 mV/s.

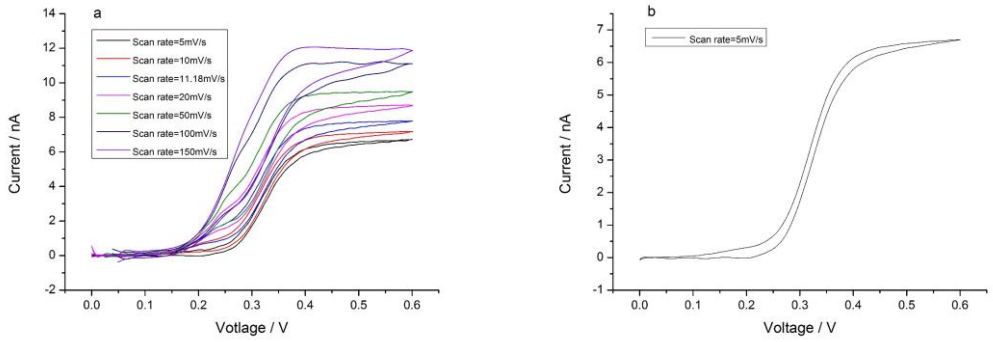

Figure 4.5 CV of 2 mM FCA with 1 mM L-cysteine at a 33 μm glassy fibre (a) at scan rates of 5, 10, 11.18, 20, 50, 100, 150 mV/s; (b) at 5 mV/s at steady state.

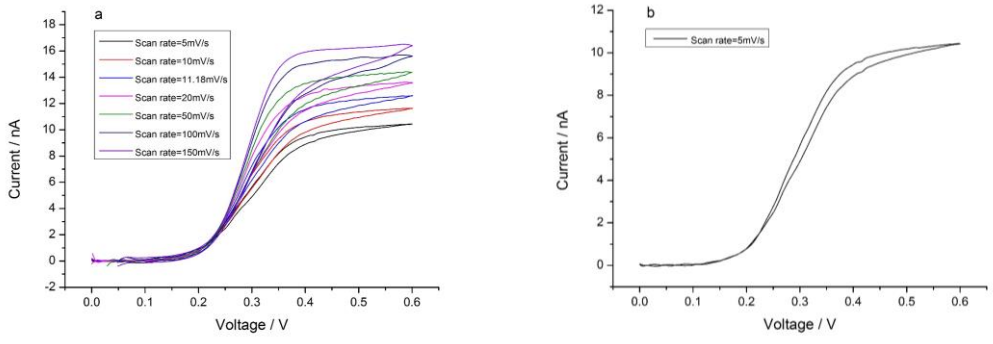

Figure 4.6 CV of 2 mM FCA with 2 mM L-cysteine at a 33 μm glassy fibre (a) at scan rates of 5, 10, 11.18, 20, 50, 100, 150 mV/s; (b) at 5 mV/s at steady state.

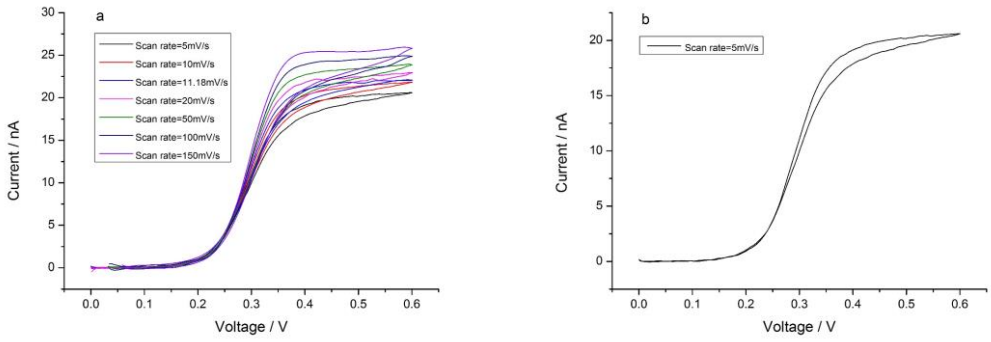

Figure 4.7 CV of 4 mM FCA with 1 mM L-cysteine at a 33 μm glassy fibre (a) at scan rates of 5, 10, 11.18, 20, 50, 100, 150 mV/s; (b) at 5 mV/s at steady state.

The effect of cysteine concentration (0 mM to 10 mM) on the EC′ steady-state current was then explored. As the concentration of L-cysteine increased, the kinetic behaviour entered zone K from KT. However, the pre-wave of the catalytic reaction was not observed in the dc voltammetry. The function of the limiting current vs L-cysteine concentration, depicted in Figure 4.8 (b), presented a good linearity (I_{ss}/nA = 2.877 × 10^{-9} × [concentration of L-cysteine] + 8.032 × 10^{-9}, N = 11, R = 0.996). The linear fit equation obtained can be used as a reference to predict the sulphide concentration.

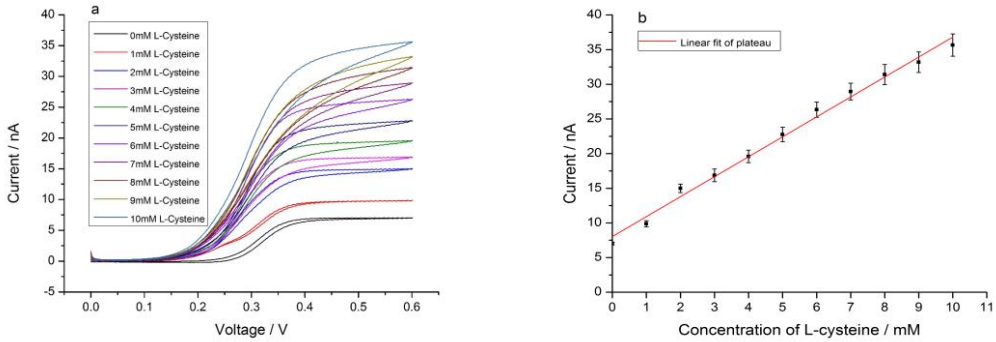

Figure 4.8 (a) CV of 2 mM FCA with various concentrations of L-cysteine (1, 2, 3, 4, 5, 6, 7, 8, 9, 10 mM) at scan rate 11.18 mV/s at a 33 μm glassy fibre.

4.3.2 Detection of L-cysteine oxidation with aqueous ferrocene derivatives at a carbon fibre electrode using FTACV

The FTACV measurements were then carried out for the microelectrode system using the microcarbon fibre electrode. The FCA (2 mM, pH = 9.2 borate buffer solution, 0.1 M KCl) was studied with the following parameters: amplitude: 50 mV, scan rate: 11.18 mV/s and frequency: from 1 Hz to 10 Hz. The first four harmonic components in the potential range of 0 to 600 mV were recorded and presented in Figure 4.9 in a current–time form. In Figure 4.9 (a), the symmetrical bell-shaped peaks indicated a good reversibility and the $E_{1/2}$ obtained were 319 mV (oxidation) and 317 mV (reduction), which were independent to frequency. In Figure 4.9 (b), two peaks with closely equal height were observed in the oxidative and reductive process. The $E_{1/2}$ at the second harmonic was identical to the first harmonic component, 319 mV and 317 mV. Peaks of the third and fourth harmonic components, in Figure 4.9 (c) and (d), increased with the frequency enhancement and lay symmetrically around the $E_{1/2.}$

Next, 1 mM L-cysteine was added to the 2 mM FCA aqueous solution to induce the homogeneous chemical reaction. FTACV was used to detect the electrochemical response of the electrocatalytic reaction with same experimental setup. The current response of the fundamental harmonic component at different frequencies is plotted in Figure 4.10 (a). As the frequency increased, the peak value increased. The peak potential shifted in an oxidative direction, from 299 mV (at 1 Hz) to 318 mV (at 2 Hz) and remained at 319 mV when the frequency was above 3 Hz. The asymmetric shape of the peak was due to the catalytic reaction of FCA and L-cysteine. The current was composed of two parts: the current of the redox reaction and the current of the oxidation of regenerated Fc from the catalytic process. For the second harmonic component, the elimination of capacitive

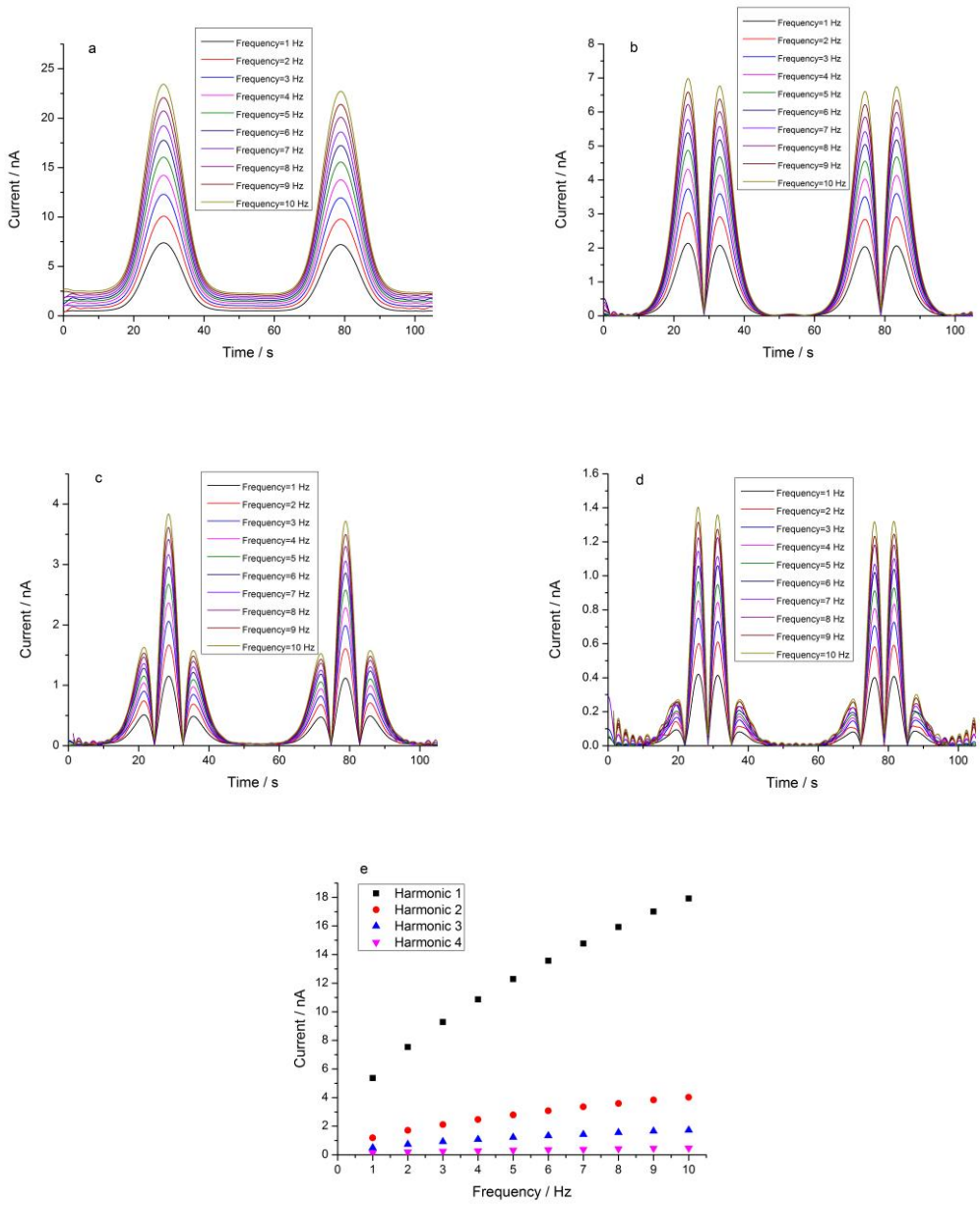

Figure 4.9 The FTACV of 2 mM FCA at various frequencies, scan rate 11.18 mV/s, amplitude: 50 mV, potential range: 0–0.6 V at a 33 μm glassy carbon electrode, (a) first harmonic; (b) second harmonic; (c) third harmonic; (d) fourth harmonic; (e) comparison of peak value of each harmonic component.

background enhanced the ability of pre-wave detection. As Figure 4.10 (b) shows, an inflection was observed ahead of the oxidation first peak and decayed as the frequency increased. The potential of the pre-wave, however, remained at 243 mV and was observed to be independent of the frequency. As expected, because the higher harmonic

components had greater sensitivity to the faradaic component, the current response of the catalytic reaction showed the familiar split wave behaviour in the third harmonic component as in Figure 4.10 (c), with the pre-wave peak observed at 212 mV. Similarly, the pre-wave decayed but the peak of the redox reaction increased as the frequency increased.

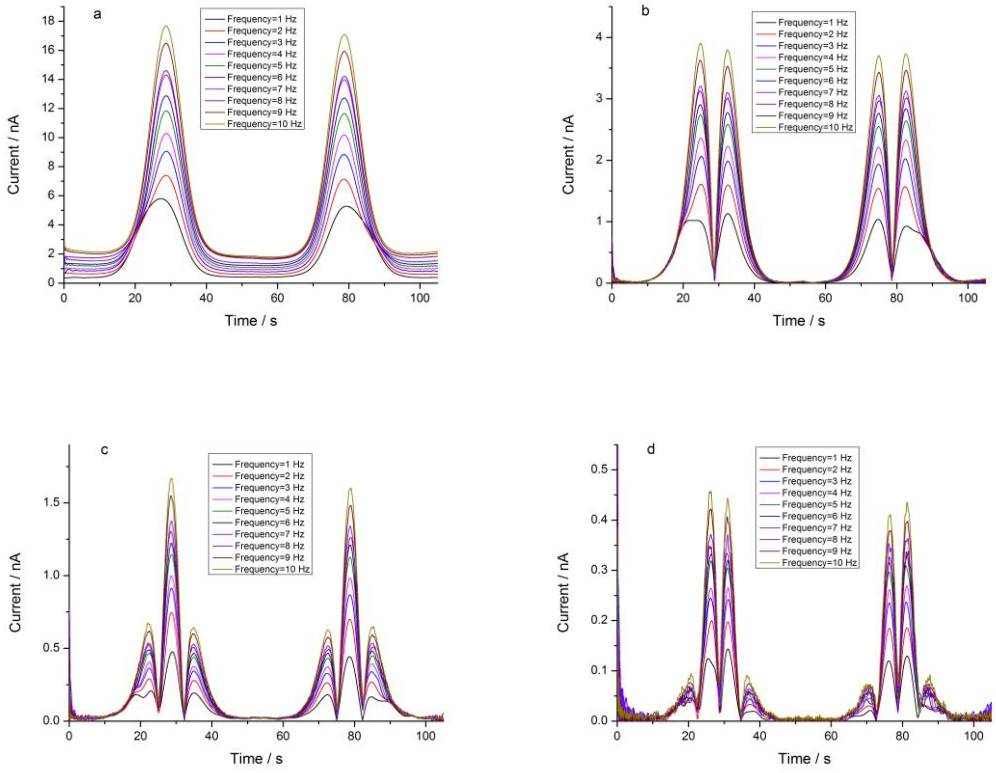

Figure 4.10 The FTACV of 2 mM FCA with 1 mM L-cysteine at various frequencies, scan rate 11.18 mV/s, amplitude: 50 mV, potential range: 0–0.6 V at a 33 μm glassy carbon electrode, (a) first harmonic; (b) second harmonic; (c) third harmonic; (d) fourth harmonic.

Next, FTACV detection was carried out employing the same setup when the substrate-mediator ratio was 1:1. For the fundamental harmonic response, in Figure 4.11 (a), a peak shift was observed when the frequency was lower than 3 Hz. When the frequency was above 5 Hz, the peak potential was not influenced by frequency and remained at 320 mV. For the second harmonic component, the first peak was much higher than the second of the oxidation reaction as Figure 4.11 (b) shows. The phenomenon could be

explained that the signal of the catalytic reaction merged with the current of the reversible reaction. When the kinetic zone of the reaction enters the K zone, the current behaviour is controlled by the current response of the catalytic reaction. As a result, the first peak shifts towards the pre-wave and the value of the first peak becomes enhanced at low frequencies. The contribution of the C′ step, however, is limited at a high frequency. In the third and fourth harmonic components, as Figure 4.11 (c) and (d) depicts, the split wave presented at a low frequency and the peak height decreased as the frequency increased.

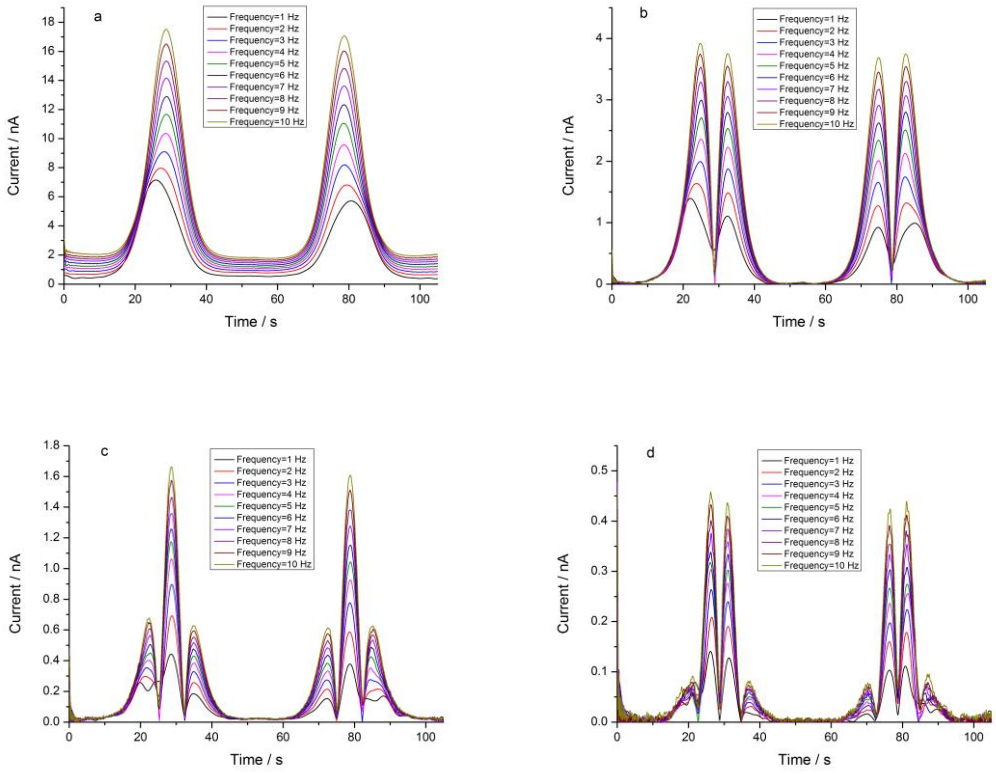

Figure 4.11 The FTACV of 2 mM FCA with 2 mM L-cysteine at various frequencies, scan rate 11.18 mV/s, amplitude: 50 mV, potential range: 0–0.6 V at a 33 μm glassy carbon, (a) first harmonic; (b) second harmonic; (c) third harmonic; (d) fourth harmonic.

The current response of the EC′ mechanism with large excess of substrate species was then studied using FTACV with the same parameters. In Figure 4.12 (a), a positive potential shift of peaks was observed in the fundamental harmonic component. The

current response of the C′ step merged with the original redox peaks in the second harmonic component, which led to a large current enhancement of the first peak, in Figure 4.12 (b). In Figure 4.12 (c) and (d), the disappearance of the pre-peak at the third and higher harmonics indicates the domination of the current by the catalytic reaction.

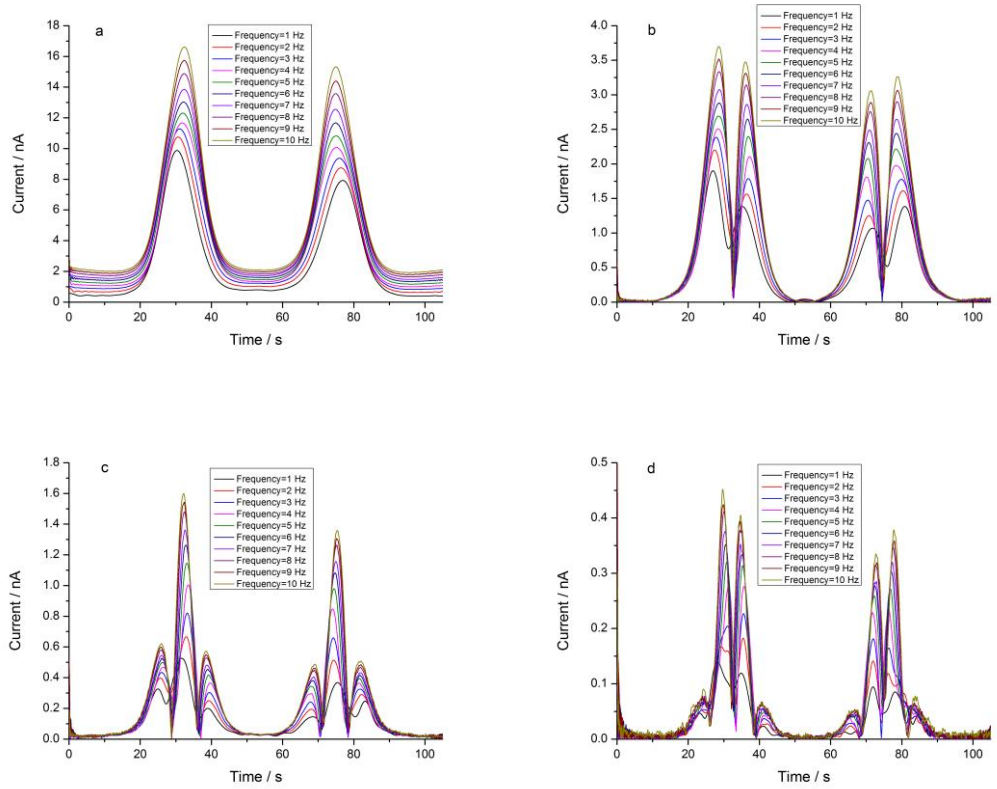

Figure 4.12 The FTACV of 2 mM FCA with 4 mM L-cysteine at various frequencies, scan rate 11.18 mV/s, amplitude: 50 mV, potential range: 0–0.6 V at a 33 μm glassy carbon electrode, (a) first harmonic; (b) second harmonic; (c) third harmonic; (d) fourth harmonic.

To investigate the influence of substrate concentration, the parameters were used as: frequency: 1 Hz, scan rate: 11.18 mV/s, amplitude: 50 mV, potential range: 0–0.6 V. The electrochemical performance of the FCA electrolyte with 1 mM, 2 mM, 3 mM L-cysteine was shown in Figure 4.13. For the fundamental harmonic component, the current enhancement was obtained for both oxidative and reductive reactions, as Figure 4.13 (a) shows. For a forward scan, the response of the catalytic reaction rose as the concentration of substrate increased, which led to a peak shift. The redox peak current

also increased as more substrate was added into the system. For the second harmonic component, in Figure 4.13 (b), when more L-cysteine was added, the current gain of the electroactive reaction grew. As such, the catalytic reaction significantly affected the peak of the original redox reaction. The $E_{1/2}$ was not varied by the substrate concentration and remained at 319 mV. The pre-waves, in the third harmonic component (Figure 4.13 (c)), showed split-wave characteristics. Peak separation was also observed in the fourth harmonic component, in Figure 4.13 (d). FTACV presented the advantage of simple determination of $E_{1/2}$ at second and higher harmonic components.

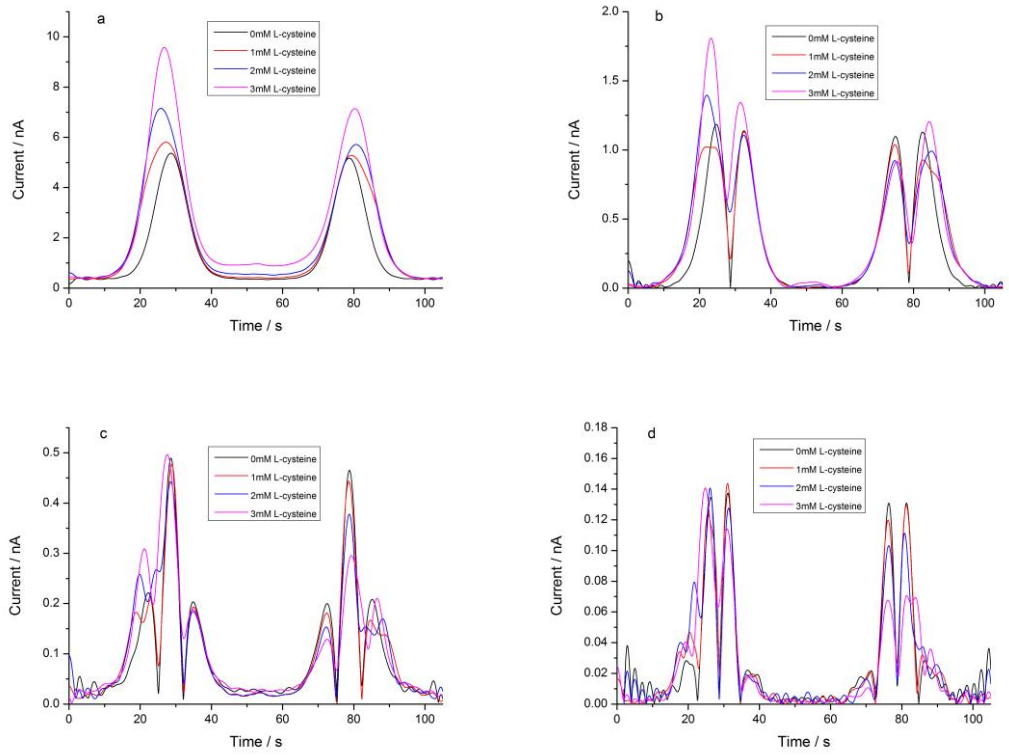

Figure 4.13 The FTACV of 2 mM FCA with various concentrations of L-cysteine at frequency 1 Hz, scan rate 11.18 mV/s, amplitude: 50 mV, potential range: 0–0.6 V at a 33 μm glassy carbon electrode, (a) first harmonic; (b) second harmonic; (c) third harmonic; (d) fourth harmonic.

4.3.3 EC′ process at gold microelectrodes by dc voltammetric technique

Gold electrodes have been commonly applied as the working electrodes due to their widely accepted stability. In this section, a three-electrode system (a: working: 100 μm, reference: 100 μm, counter: 1 cm; b: working: 500 μm, reference: 500 μm, counter: 1 cm) was used to analyse the EC′ mechanism. First, the aqueous electrolyte, containing 1 mM ferrocene methanol and 0.1 M potassium nitrate, was used to define the effective area of the gold electrode. Figure 4.14 (a) and (b) illustrates cyclic voltammograms measured at 100 μm and 500 μm with various scan rates. Effective areas obtained from the Randles–Sevcik equation were 3.48×10^{-4} cm^2 for 100 μm and 11.03×10^{-4} cm^2 for 500 μm.

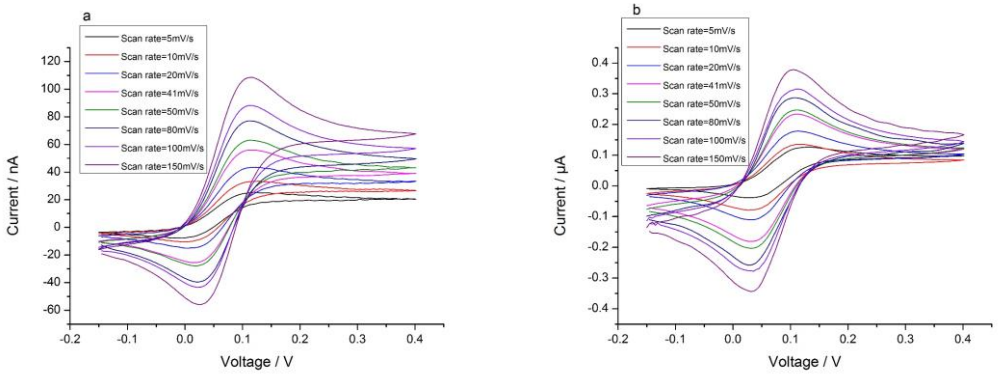

Figure 4.14 CV of 1 mM ferrocene methanol with various scan rates (from 5 mV/s to 150 mV/s) at (a) 100 μm gold electrode; (b) 500 μm gold electrode.

The electrocatalytic reaction, by introducing 2 mM L-cysteine into the 2 mM FCA aqueous electrolyte, was then studied using the gold electrodes. Figure 4.15 (a) presents the current behaviour of EC′ mechanism with the cysteine:FCA ratio 1:1 at the 100 μm gold electrode using the dc voltammetric technique. A plateau was achieved when the scan rate decreased to 14.9 mV/s and characteristic peak-behaviour was observed as the scan was increased. Under steady-state conditions using a scan rate of 14.9 mV/s, the

pre-wave appeared ahead of the plateau (Figure 4.15 (c)). Notably, the linearity of the oxidation peak current vs square root of the scan rate was not influenced by the appearance of L-cysteine, as Figure 4.15 (d) depicts (R_d = 0.997).

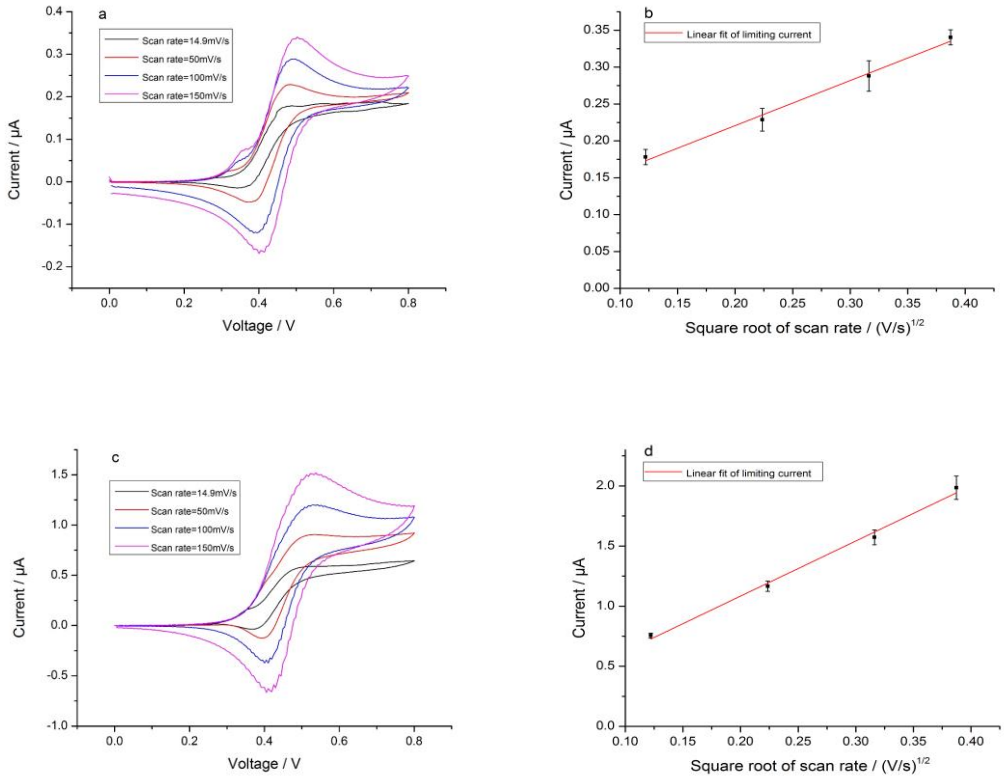

Figure 4.15 CV of 2 mM FCA with cysteine-FCA ratio (a) 1:1 at 100 µm gold electrode; (c) 1:1 500 µm gold electrode; (b) and (d) are linear fits for limiting current vs the square root of scan rate.

4.3.4 FTACV of the EC′ process at gold microelectrodes

The final experimental investigations in the chapter were carried out on a gold microelectrode using FTACV. At the fundamental harmonic, a symmetrical bell-shaped current response was observed, as Figure 4.16 (a) shows. The electrode material did not affect the reversibility of the redox couple, but did influence the characteristic potential. The $E_{1/2}$ at the gold electrode was found to be 239 ± 3 mV, compared with the 319 mV measured at the carbon electrode. In Figure 4.16 (b), even though a small

shift of $E_{1/2}$ occurred in the second harmonic component, the current curve behaved as the expected symmetrical double-peak and centred at $E_{1/2}$. The peak shift may be attributed to the use of a gold pseudo-reference electrode in these measurements. For the second and higher harmonics, again the capacitive component became negligible with the baseline current approaching 0, Figure 4.16 (b–d).

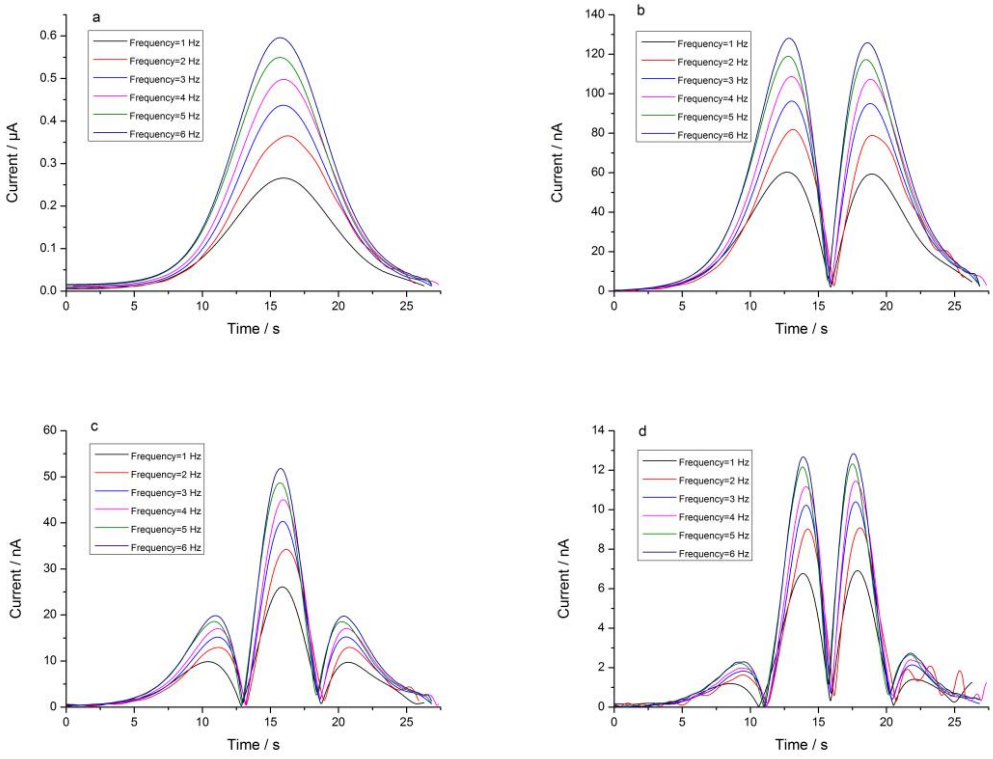

Figure 4.16 The FTACV of 2 mM FCA at scan rate 14.9 mV/s, amplitude: 50 mV, frequency: 1–6 Hz, potential range: 0–0.4 V, at 100 μm gold electrode, (a) first harmonic; (b) second harmonic; (c) third harmonic; (d) fourth harmonic.

2 mM L-cysteine was then added to the Fc/Fc^+ aqueous electrolyte and the solution was monitored using FTACV for the gold electrode with parameters frequency: 1 Hz, scan rate: 11.18 mV/s, amplitude: 50 mV, potential range: 0–0.6 V. For the 100 μm gold electrode, as shown in Figure 4.17, an inflection appeared ahead of the asymmetrical bell-shaped oxidation peak in the fundamental harmonic component. Even though the pre-wave disappeared in the dc voltammograms when the steady state was achieved, it

was still detectable by FTACV. This behaviour was also apparent on the 500 μm gold electrode in Figure 4.18.

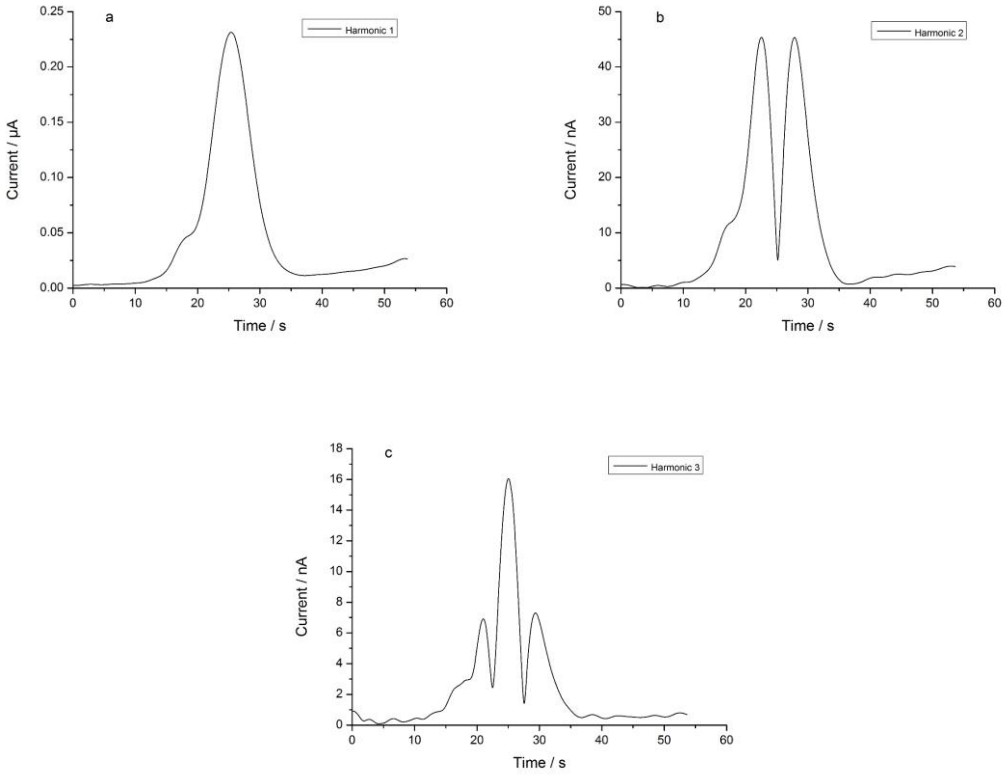

Figure 4.17 The FTACV of 2 mM FCA with 2 mM L-cysteine at scan rate 11.18 mV/s, amplitude: 50 mV, frequency: 1 Hz, potential range: 0–0.6 V, at 100 μm glassy carbon electrode, (a) first harmonic; (b) second harmonic; (c) third harmonic.

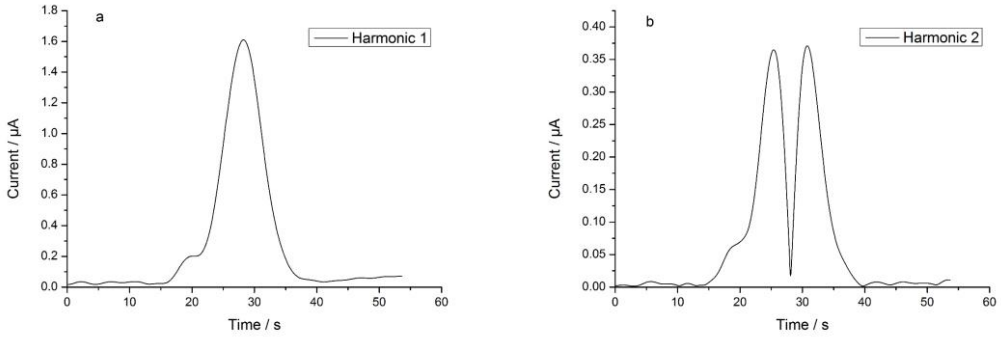

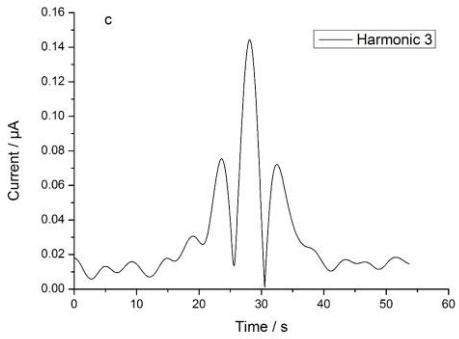

Figure 4.18 The FTACV of 2 mM FCA with 2 mM L-cysteine at scan rate 11.18 mV/s, amplitude: 50 mV, frequency: 1 Hz, potential range: 0–0.6 V, at 500 μm glassy carbon electrode, (a) first harmonic; (b) second harmonic; (c) third harmonic.

4.3.5 Numerical simulation for the EC′ mechanism at microdisc electrodes

Numerical simulations were extended from those presented in Chapter 3 to account for the enhanced mass transport characteristics on the microdisc electrode. In this section, the modelling was used to explore and support the analysis of the trends predicted for this complex EC′ mechanism at microdisc electrodes. The parameters used in these models were as follows: diameter of electrode = 30 μm, scan rate = 10 mV/s, diffusion coefficient of redox species = 7.6×10^{-6} cm^2/s, K_EC′ = 1000, R = 8.314 J/(mol·K), T = 298 K, F = 96485 C/mol.

Figure 4.19 depicts the first four harmonic components of electrochemical behaviour for an EC′ investigation using a microelectrode with a substrate:mediator concentration ratio of 2:1. The frequency range used was 1–6 Hz. For the first harmonic component, in Figure 4.19 (a), the pre-wave appeared ahead of the oxidative response and decayed as frequency increased. The potential of the redox peak, however, did not vary with frequency. Notably, an inflection also appeared in the reverse scan due to the enhanced diffusion efficiency and fast replenishment of substrate on the surface of the

microelectrode. Pre-waves were clearly observed in the second harmonic component (Figure 4.19 (b)). The current contribution from the catalytic reaction led to the area of the first peak being larger than that of the second. For the third harmonic component, (Figure 4.19 (c)) split wave behaviour was again clearly observable and this was seen to merge with the main current peak as the frequency increased. A similar phenomenon was observed in the fourth harmonic component in Figure 4.19 (d).

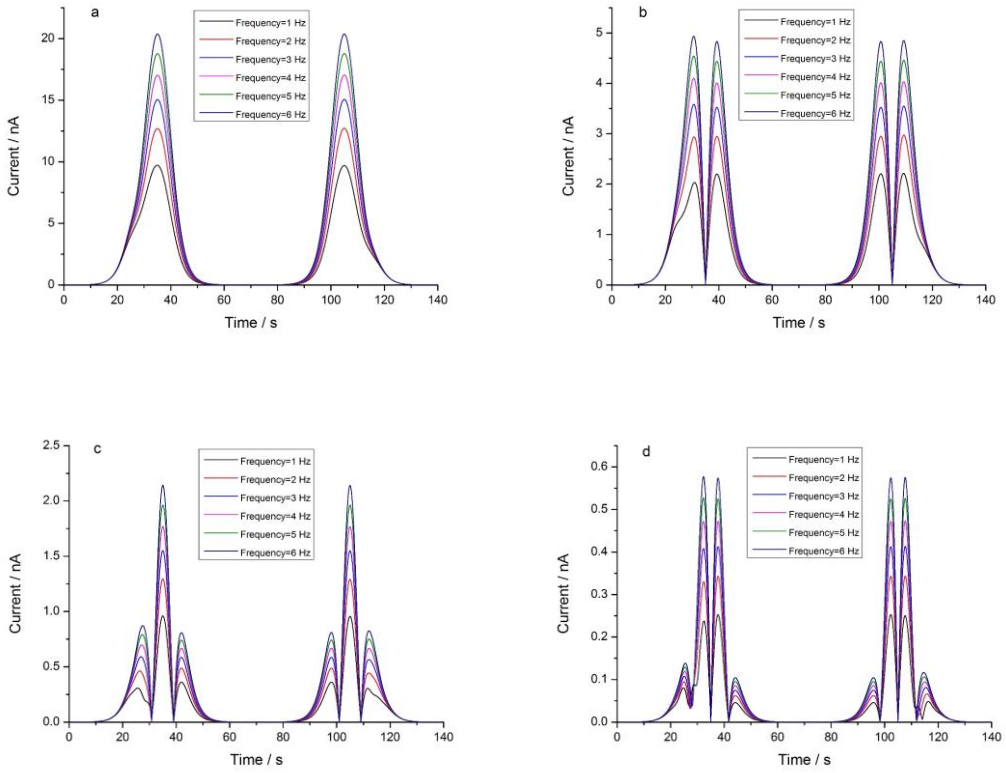

Figure 4.19 Numerical modelling of the EC′ mechanism with substrate-mediator concentration ratio 2:1, (a) first harmonic; (b) second harmonic; (c) third harmonic; (d) fourth harmonic.

Figure 4.20 shows the current response for the case of a substrate:mediator concentration ratio of 1:1. As the frequency increased, the effect of the pre-wave decayed due to the limitation of kinetics of the catalytic reaction. In addition, the E process became significant in the system due to the fast replenishment of redox species from the bulk to the electrode surface. For the second harmonic component, the merging of the pre-wave with the first peak was observed as the frequency increased. When the

frequency was lower than 3 Hz, even though the height of the first peak was lower than the second at the forward scan, the area of the first was larger than the second. Similar phenomena were also observed when the substrate:mediator concentration ratio was 2:1 (Figure 4.21).

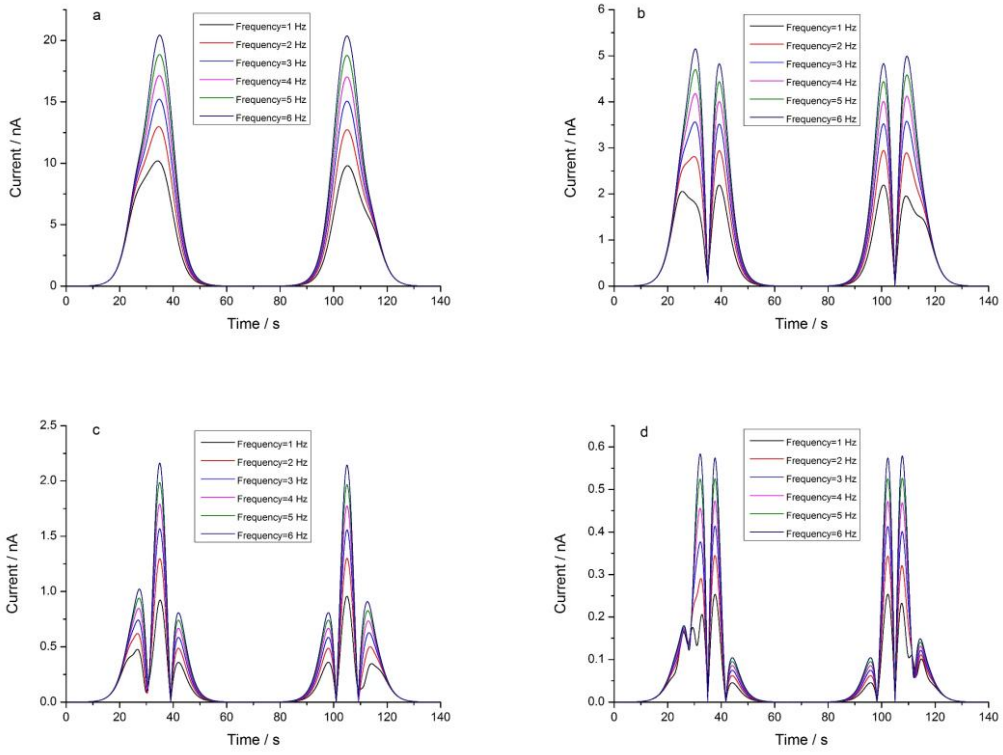

Figure 4.20 Numerical modelling of the EC′ mechanism with FCA against L-cysteine 1:1, (a) first harmonic; (b) second harmonic; (c) third harmonic; (d) fourth harmonic.

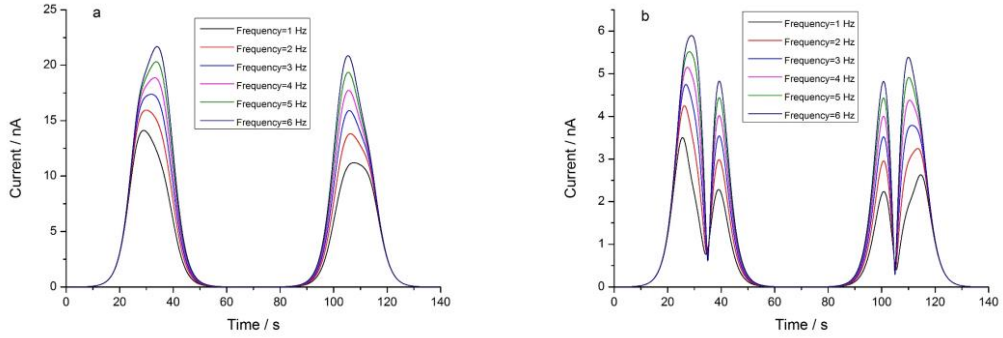

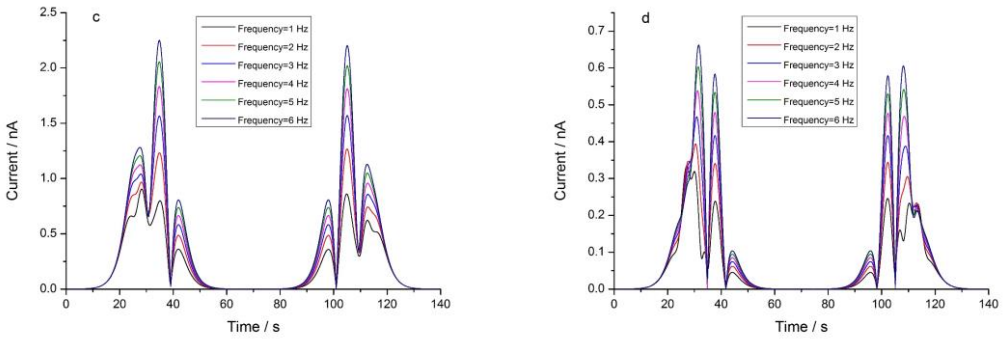

Figure 4.21 Numerical modelling of the EC′ mechanism with FCA against L-cysteine 1:2, (a) first harmonic; (b) second harmonic; (c) third harmonic; (d) fourth harmonic

When the substrate:mediator ratio was increased to 4:1, the current response of the first harmonic component could be seen (Figure 4.22 (a)). The peak of the forward scan was composed of the sum of the current responses of C′ and E steps and the asymmetrical peak shifted towards the redox potential as the frequency increased. For the second harmonic component in Figure 4.22 (b), the first peak was higher than the second at all frequencies and the peak area was larger than the second due to the contribution of the C′ step. Similar phenomena were observed at both the third and fourth harmonic components, as shown in Figure 4.22 (c) and (d). From the simulated results, the peak behaviour was varied by the appearance of the substrate, but the $E_{1/2}$ was not strongly affected. Notably, the simulated outcome was free from uncompensated noise, which, however, caused a significant disturbance at the fourth and higher harmonic components in the experimental results.

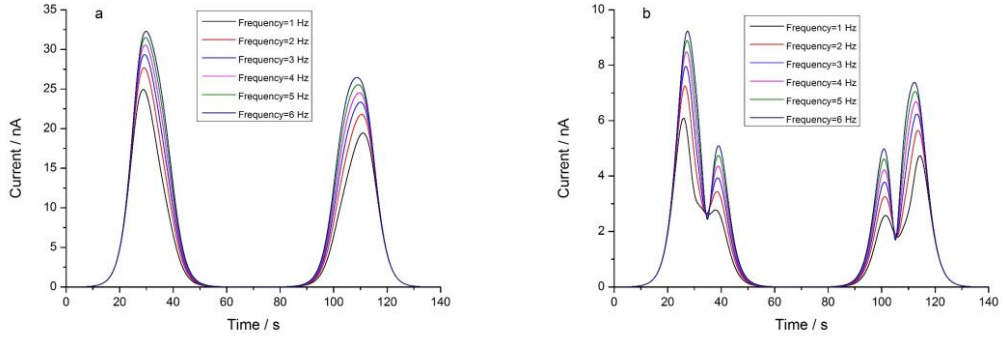

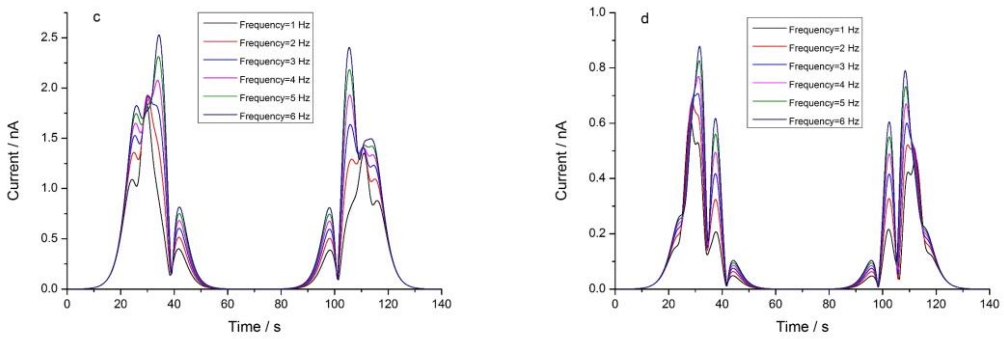

Figure 4.22 Numerical modelling of the EC′ mechanism with FCA against L-cysteine 1:4, (a) first harmonic; (b) second harmonic; (c) third harmonic; (d) fourth harmonic.

Finally, the effect of the substrate concentration was investigated with a frequency of 1 Hz in Figure 4.23. As the substrate concentration increased, the behaviour of the pre-wave changed from an inflection to a peak that merged with the redox peak in the first harmonic component (Figure 4.23 (a)). Moreover, the asymmetrical peak shifted towards the pre-wave. On the reverse scan, the inflection appeared to the right of the reductive curve. For the second harmonic component, the pre-wave of the catalytic reaction merged with the first peak of the oxidative reaction when the substrate:mediator ratio was above 1:1 in Figure 4.23 (b). Comparing with the macroscale electrode, the current of C′ on the microelectrode was stronger due to the enhanced diffusional efficiency.

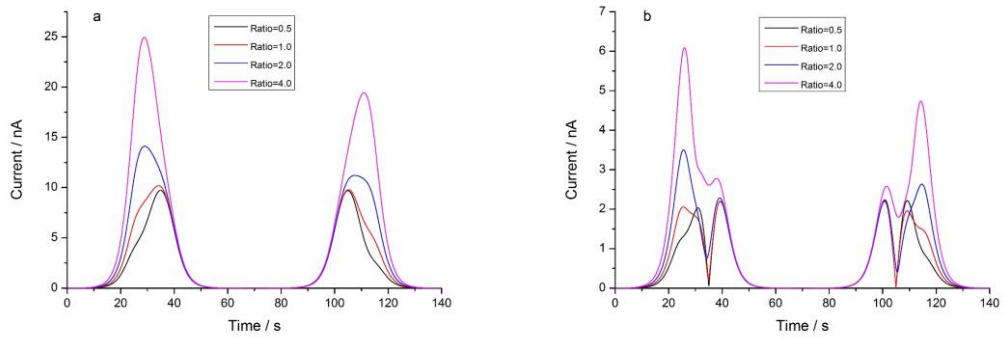

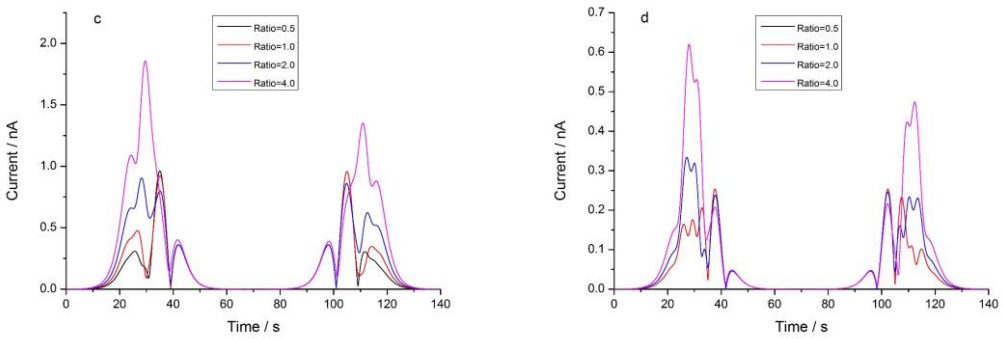

Figure 4.23 Numerical modelling of the EC′ mechanism as substrate:mediator ratio varies from 0.5:1 to 4:1, (a) first harmonic; (b) second harmonic; (c) third harmonic; (d) fourth harmonic.

4.4 Conclusion

In this chapter, the pre-wave behaviour caused by the reaction with the catalytic mediator was investigated at the microscale electrodes using cyclic voltammetry and FTACV. In the dc cyclic voltammetry, the enhanced mass transport characteristics of the microelectrode lead to a loss of a clear split wave feature. This is because the kinetic value of the homogeneous reaction, namely reaction with sulphide, is not sufficient to induce the clear separation. The linear fit of the limiting current vs the sulphide concentration, however, proves the possibility of quantitative detection of sulphide species using the EC′ mechanism on the microscale electrodes.

In comparison to the dc voltammetric technique, FTACV presents an advantage in describing the electrode kinetic reaction with the sulphide. The split waves were clearly observed at the second and become clearer at higher harmonic components, which are sensitive to the faradaic components. The accurate potential determination of FTACV is another advantage, especially for the microelectrode detection, which is hard to determine from the plateau current in the dc voltammetric technique. The numerical simulation agreed with the interpretation of the experimental results. Moreover, the split-wave phenomena under steady state were documented for the first time, which also has enormous value for further fundamental studies of the EC′ mechanism.

Reference

1. Bard, A.J. and L.R. Faulkner, *Electrochemical methods: fundamentals and applications.* 2001.
2. Clark, L., et al., *Continuous recording of blood oxygen tensions by polarography.* Journal of applied physiology, 1953. **6**(3).
3. Lawrence, N.S., et al., *Electrochemically Initiated 1,4-Nucleophilic Substitutions:A General Strategy for the Analytical Detection of Hydrogen Sulfide.* Electroanalysis, 2001. **13**(6): p. 432-436.
4. Lawrence, N.S., et al., *A Thin-Layer Amperometric Sensor for Hydrogen Sulfide: The Use of Microelectrodes To Achieve a Membrane-Independent Response for Clark-Type Sensors.* Analytical Chemistry, 2003. **75**(10): p. 2499-2503.
5. Luther, I.I.I.G.W., et al., *Sulfur speciation monitored with solid state gold amalgam voltammetric microelectrodes: polysulfides as a special case in sediments, microbial mats and hydrothermal vent waters.* Journal of Environmental Monitoring, 2001. **3**(1): p. 61-66.
6. Antonietta Baldo, M., et al., *Voltammetric investigation on sulfide ions in aqueous solutions with mercury-coated platinum microelectrodes.* Analytica Chimica Acta, 2002. **464**(2): p. 217-227.
7. Jordan, J., J. Talbott, and J. Yakupkovic, *Electroanalytical Chemistry of Sulfur Compounds For the New Coal Conversion Technologies.* Analytical Letters, 1989. **22**(6): p. 1537-1546.
8. Shirsat, M.D., et al., *Polyaniline nanowires-gold nanoparticles hybrid network based chemiresistive hydrogen sulfide sensor.* Applied Physics Letters, 2009. **94**(8): p. 083502.
9. Yourong, W., Y. Heqing, and W. E'Feng, *The electrochemical oxidation and the quantitative determination of hydrogen sulfide on a solid polymer electrolyte-based system.* Journal of Electroanalytical Chemistry, 2001. **497**(1): p. 163-167.
10. Pandey, S.K., K.-H. Kim, and K.-T. Tang, *A review of sensor-based methods for monitoring hydrogen sulfide.* TrAC Trends in Analytical Chemistry, 2012. **32**: p. 87-99.
11. Yu, C., et al., *Electrochemical H2S sensor with H2SO4 pre-treated Nafion membrane as solid polymer electrolyte.* Sensors and Actuators B: Chemical, 2002. **86**(2): p. 259-265.
12. Analytics, H., *Gas Detection.* ICE web Index.
13. Jeroschewski, P., et al., *Galvanic sensor for determination of hydrogen sulfide.* Electroanalysis, 1994. **6**(9): p. 769-772.
14. FranaTech, *SHALLOW WATER HYDROGEN SULPHIDE MICRO-SENSOR.* http://www.franatech.com/hydrogen_sulfide_sensor.html.
15. Lawrence, N.S., et al., *Electroanalytical applications of boron-doped diamond microelectrode arrays.* Talanta, 2006. **69**(4): p. 829-834.

16. Oldham, K.B., *Steady-state microelectrode voltammetry as a route to homogeneous kinetics.* Journal of Electroanalytical Chemistry and Interfacial Electrochemistry, 1991. **313**(1): p. 3-16.
17. Harvey, S.L.R., K.H. Parker, and D. O'Hare, *Theoretical evaluation of the collection efficiency at ring-disc microelectrodes.* Journal of Electroanalytical Chemistry, 2007. **610**(2): p. 122-130.
18. Tutty, O.R., *Second-order kinetics for steady state EC′ reactions at a disc microelectrode.* Journal of Electroanalytical Chemistry, 1994. **377**(1): p. 39-51.
19. TUTTY, O.R. and G. DENUAULT, *Second-order kinetics for EC' reactions at a spherical microelectrode.* IMA Journal of Applied Mathematics, 1994. **53**(1): p. 95-109.
20. Tutty, O.R., *The current near the edge of a microelectrode for steady state EC′ reactions.* Journal of Electroanalytical Chemistry, 1994. **379**(1): p. 519-521.
21. Phillips, C.G., *The steady, diffusion-limited current at a disc microelectrode with a first-order EC' reaction.* Journal of Electroanalytical Chemistry and Interfacial Electrochemistry, 1990. **296**(1): p. 255-258.
22. Rountree, E.S., et al., *Evaluation of Homogeneous Electrocatalysts by Cyclic Voltammetry.* Inorganic Chemistry, 2014. **53**(19): p. 9983-10002.

Chapter 5 Detection of a steady-state electrocatalytic reaction in hydrodynamic devices

5.1 Introduction

In this chapter, hydrodynamic voltammetry is used to detect the sulphide concentration using the EC′ pathway. Precisely engineered hydrodynamic devices incorporating microband gold electrodes were recorded by dc and ac voltammetric measurements. The split-wave phenomena achieved in both dc and FTACV were documented for the first time, providing proof of the possibility to detect the sulphide concentration continuously by the electrochemical approach under fluidic conditions. In addition, the results and discussion in this chapter provide guidance for further electrochemical studies on how the EC′ current behaves on hydrodynamic electrodes. Supporting numerical simulations were developed by considering laminar fluid in the rectangular channel based on the electrochemical models to understand the effect of convections on voltammetric properties.

5.2 Microengineered devices in microfluidic application

Innovation in microengineering is considered to be a cross-disciplinary development that combines chemistry, biology, and mechanics[1]. Integrated structures of sensors, actuators, and electronics are commonly referred to as microsystems in Europe or micro-electro-mechanical systems (MEMS) in the United States[2]. A broad range of technologies in microfabrication have been developed, such as lab-on-a-chip[3],

miniaturized chemical analytical sensors[4], and microreactors[5]. These technologies have been applied in a range of areas, such as pressure sensors[6], medical and chemical detectors[7, 8], energy harvesters[9, 10], and environmental monitors[11, 12]. Evolution of these technologies has changed human's life and brought more possibilities both in research and industry. For example, due to the miniaturized size, pressure sensors using MEMS technology have advantageous applications in confined space and preciseness of measurement[13]. Low cost, high sensitivity, and ease of integration with electronics contribute to the potential for economical batch manufacturing [13-15].

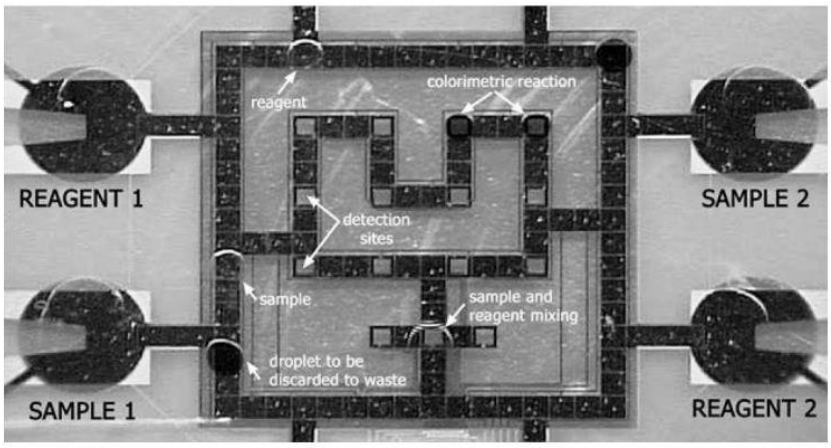

Figure 5.1 A digital microfluidic lab-on-a-chip applied in clinical detection[16]

In addition to the single-function products, prospects of devices that incorporate various functional elements in one and keep on a microscale can also be achieved by microengineering technology. Integration of detecting sensors on an equivalent circuit chip has been widely accepted as an efficient way to realize the idea of multifunctional microscale equipment. A blood glucose sensor uniting the wireless remote monitoring function, the function of blood glucose detection and data communication through a wireless connection is a success of microengineering[17, 18]. The innovation of glucose sensors in smaller sizes reduces customer's reliance on the detecting devices and the function of real-time updating brings an efficient way for data collecting. Moreover,

the microfabrication approaches that integrate multiple sensors not only meet the needs of environmental monitoring but also achieve the miniaturization of devices[19, 20]. The analytical sensor for sulphide in aqueous solution is another example of a lab-on-a-chip device. Every microengineered device is uniquely designed to provide a laminar fluidic circumstance and the three-electrode system is ready for rapid sulphide detection[21, 22]. Figure 5.1 presents an integrated sensor that combines microreactor and microdetector on an electronic board.

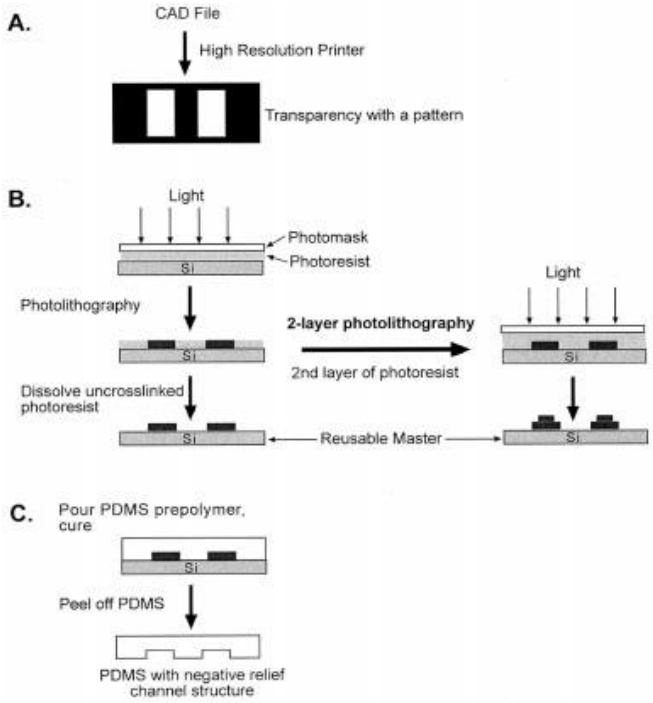

Figure 5.2 Schematic illustration for rapid prototyping and fabricating of PDMS in the microfluidic system[23].

PDMS, due to its low price, excellent flexibility, optical transparency and non-toxicity, has been recognized as one of the most common materials in microfabrication. Procedures for fabricating PDMS elastomer for microfluidic applications have been reported in several papers[23-25]. The soft lithography process, regarded as a typical fabrication method of PDMS, is detailed in Figure 5.2. The simplified procedures save fabrication time and make it possible to manufacture in large batches. Other advantages include the property of water impermeability and excellent sealing on the substrate.

Potentiometric sensors and amperometric sensors are the two main electrochemical approaches to analyse the current/voltage behaviour of microfluidics[26]. In this chapter, the under-controlled electroactive stream in the microengineered devices reacted with sulphide and the change of electrochemical behaviour was detected by dc techniques and FTACV. The split wave was detected for the first time under hydrodynamic circumstances in the FTACV. The FTACV proved its potential in sulphide detection.

5.3 Lab-on-a-chip microfluidic devices for sulphide sensing

Because of the importance in chemical detection and energy conversion, the EC′ mechanism has been widely studied. However, the electrochemical performance of the EC′ mechanism in microfluidic environments remains poorly studied. In addition, the application of high-resolution voltammetry techniques, such as FTACV, has surprisingly been sparse in microfluidic environments.

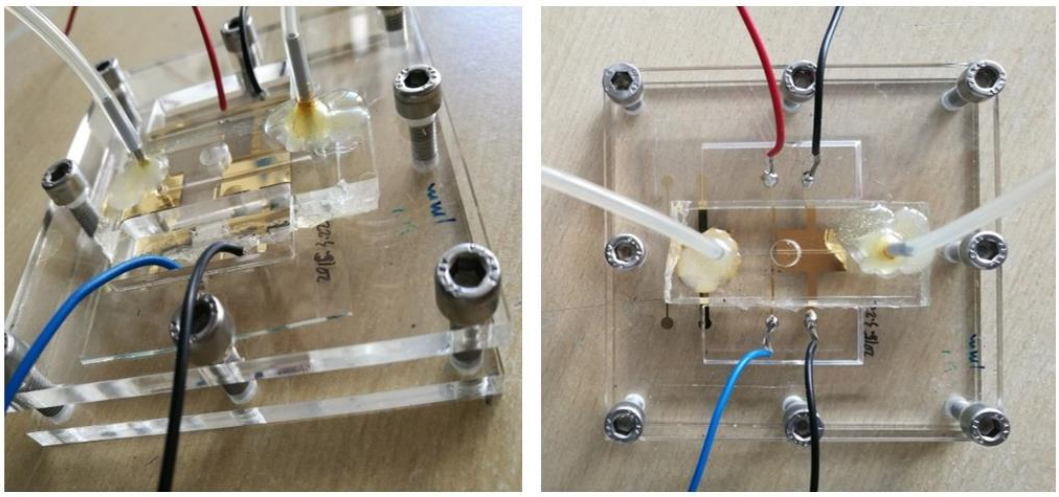

Figure 5.3 The electrochemical microfluidic detector for the EC′ mechanism, with gold band electrodes.

The microfluidic devices applied in this chapter were fabricated by the methods introduced in Chapter 2. A three-electrode system composed of three gold bands as working, counter, and reference electrodes, was fabricated on a glass substrate. The working electrodes used in this chapter were fabricated in three sizes with widths of 2 mm, 500 μm, and 100 μm. PDMS gasket channels were developed with the parameter settings noted in Chapter 2, and a typical cell configuration for voltammetric measurements is shown in Figure 5.3. A rectangular channel (dimensions were height 750 μm, width 700 μm, length 3.5 cm) was constructed and electrodes of 2 mm, 500 μm, and 100 μm plated on one wall of the cell. The length of the channel electrodes was the same as the width of the channel. The expected steady-state voltammetry characteristics for the device using a reversible one-electron transfer agent can be predicted by the Levich equation[27-30]:

$$i_L = 0.925nFC_bD^{\frac{2}{3}}v_f^{\frac{1}{3}}h^{-\frac{2}{3}}d_d^{-\frac{1}{3}}wx_e^{\frac{2}{3}}$$

where n is the number of electrons transferred in the reaction, C_b is the bulk concentration of redox species, D is the diffusion coefficient, v_f is the flow rate, h is the height of the half-cell device, d is the width of the channel, w is the length of the electrode. The schematic illustration is defined in Figure 5.4.

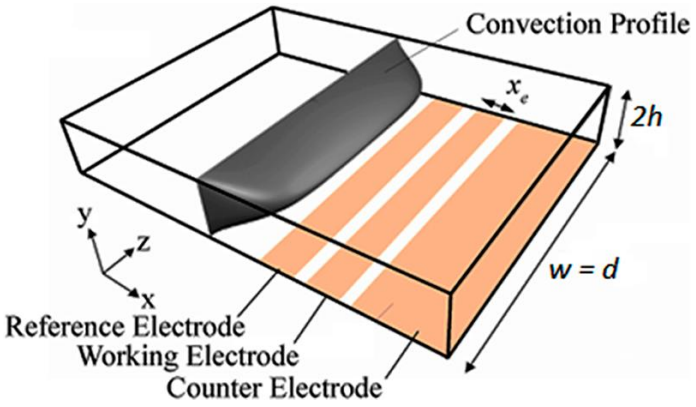

Figure 5.4 Schematic illustration of a microfluidic channel device[27].

5.4 Results and discussion

5.4.1 Calibration of the microfluidic device with ferrocenemethanol

Steady voltammetric measurements were carried out using an analyte stream containing 1 mM ferrocenemethanol as redox reactant and 0.1 M potassium nitrate as supporting electrolyte. Figure 5.5 shows the current response of the ferrocenemethanol in the microfabricated channel using the gold working electrode of width 500 μm and volumetric flow rates in the range from 0.05 cm^3/min to 0.6 cm^3/min. The transport-limited was varied linearly as a function of the cube root of flow rate, as expected from the Levich equation (Figure 5.5 (b)). The data were used to estimate the cell height of the device, which was found to be 786.73 ± 20 μm.

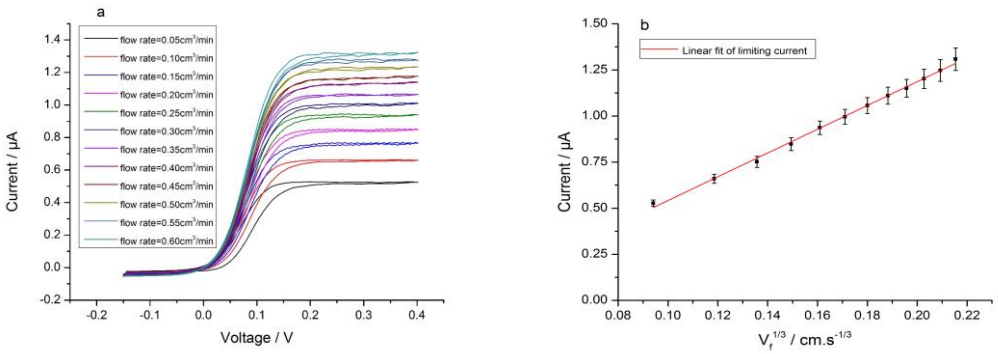

Figure 5.5 (a) CV of 1 mM ferrocenemethanol with various flow rates (from 0.05 to 0.6 cm^3/min) at a 500 μm gold electrode; (b) linear fit of 1 mM ferrocenemethanol with various flow rates (from 0.05 to 0.6 cm^3/min).

Similar measurements were carried out on the 2 mm and 100 μm channel electrodes as well, cell heights were 760.86 ± 20 μm for the 2 mm electrode and 781.80 ± 20 μm for the 100 μm electrode, which are in good agreement (750–800 μm) with that expected from the fabrication process.

5.4.2 Monitoring of the EC′ mechanism under microfluidic conditions

Once the geometry of the channels was confirmed, linear scan voltammetry (LSV) was used to investigate the catalytic reaction of L-cysteine with ferrocenecarboxylic acid (FCA) aqueous solutions (pH = 9.2). Channel cell measurements were carried out using gold electrodes of width 2 mm, 500 μm, and 100 μm as working electrodes.

First, the EC′ mechanism of sulphide and Fc/Fc^+ was investigated in the channel device with a 2 mm gold working electrode. Figure 5.6 shows the reversible reaction of 2 mM FCA with a flow rate of 0.05–0.6 cm^3/min and scan rate of 11.18 mV/s. Figure 5.6 (a) shows typical *i*/*V* curves for the system and the limiting current was observed to vary linearly (Figure 5.6 (b)) with the cube root of the volume flow rate ($I_{ss}/\mu A = 2.45 \times 10^{-5} \sqrt[3]{flow\ rate\ /(\mathrm{cm}^3/\mathrm{min})} - 3.50 \times 10^{-7}$, $N = 13$, $R = 0.999$).

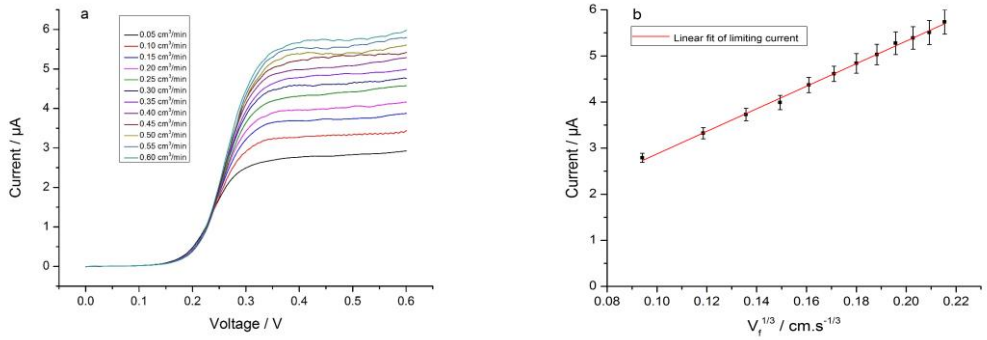

Figure 5.6 (a) LSV of FCA with various flow rates (from 0.05 to 0.6 cm^3/min) at a 2 mm gold electrode with scan rate 11.18 mV/s; (b) linear fit of limiting current.

Next (Figure 5.7 (a)), 1 mM L-cysteine was added to the system. At lower flow rates, a clear pre-wave feature was again observed for the voltammetric response. As the flow rate was increased, the pre-wave began to merge into the main redox wave. This would be expected because the convective effect can now control the delivery of reagent to

the surface and allow the kinetics of the pre-wave to be outrun by selection of an appropriate increased flow rate. When the substrate-mediator ratio increased to 1:1, (Figure 5.7 (b)) the pre-wave features and inflection became less clear. When the substrate-mediator concentration ratio was 1.5:1, as Figure 5.7 (c) and (d) shows, the current of the catalytic step completely merged with the redox curve. Again, this is expected for the convective control. It was noted that several of the waves were shifted in potential and this was considered to be due to the less stable nature of the gold pseudo-reference electrode that was used in the microfabrication process. Measurements were repeated for the smaller electrodes and the same overall characteristics were observed; however, in both cases now the pre-wave features were not observable.

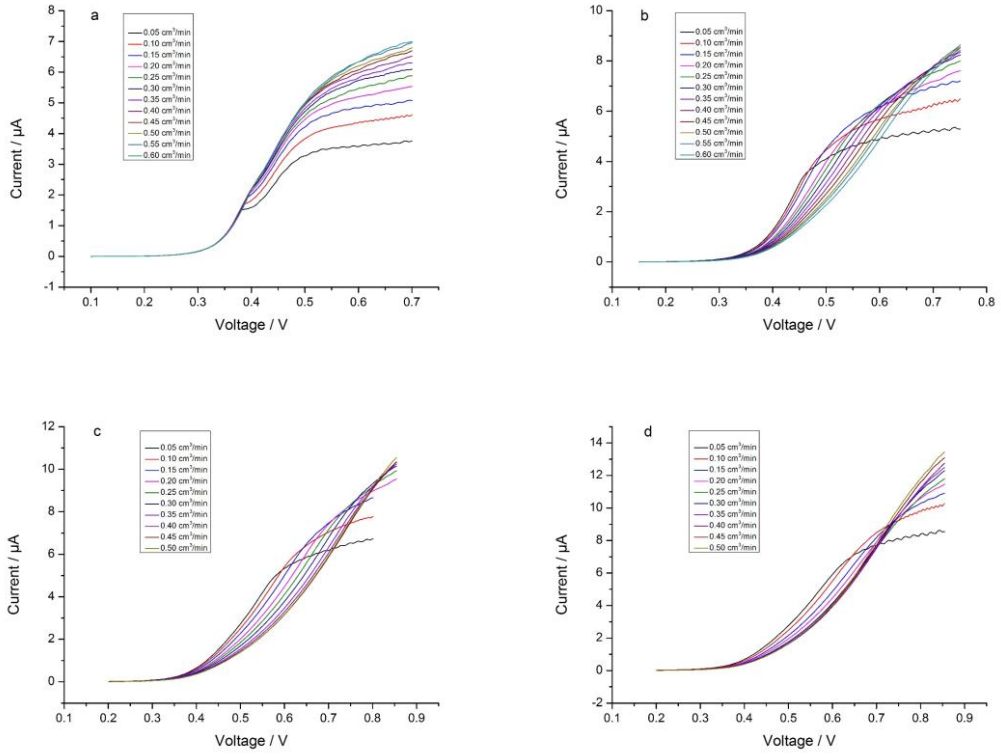

Figure 5.7 LSV of FCA in the presence of L-cysteine with various flow rates (from 0.05 to 0.6 cm^3/min) at a scan rate 11.18 mV/s on a 2 mm gold electrode (a) 1 mM L-cysteine; (b) 2 mM L-cysteine; (c) 3 mM L-cysteine; (d) 4 mM L-cysteine.

Next, the influence of substrate:mediator concentration ratio on the electrochemical behaviour was investigated. The electrochemical response of the same flow rates was compared (0.05 cm^3/min, 0.10 cm^3/min, 0.15 cm^3/min, 0.20 cm^3/min) in Figure 5.8. For the flow rate of 0.05 cm^3/min, in Figure 5.8 (a), a clear split wave appeared ahead of the limiting current when the 1 mM substrate was added to the solution. The inflection, related to the homogeneous chemical reaction, decayed and merged with the redox current as the concentration of L-cysteine increased. In addition, the increase of L-cysteine concentration led to the shift of the current–voltage curve in an oxidative direction. Similar phenomena were achieved at a higher flow rate; the elevated current value at the same flow rate was due to reoxidation of FCA generated from the catalytic reaction of Fc^+ and L-cysteine.

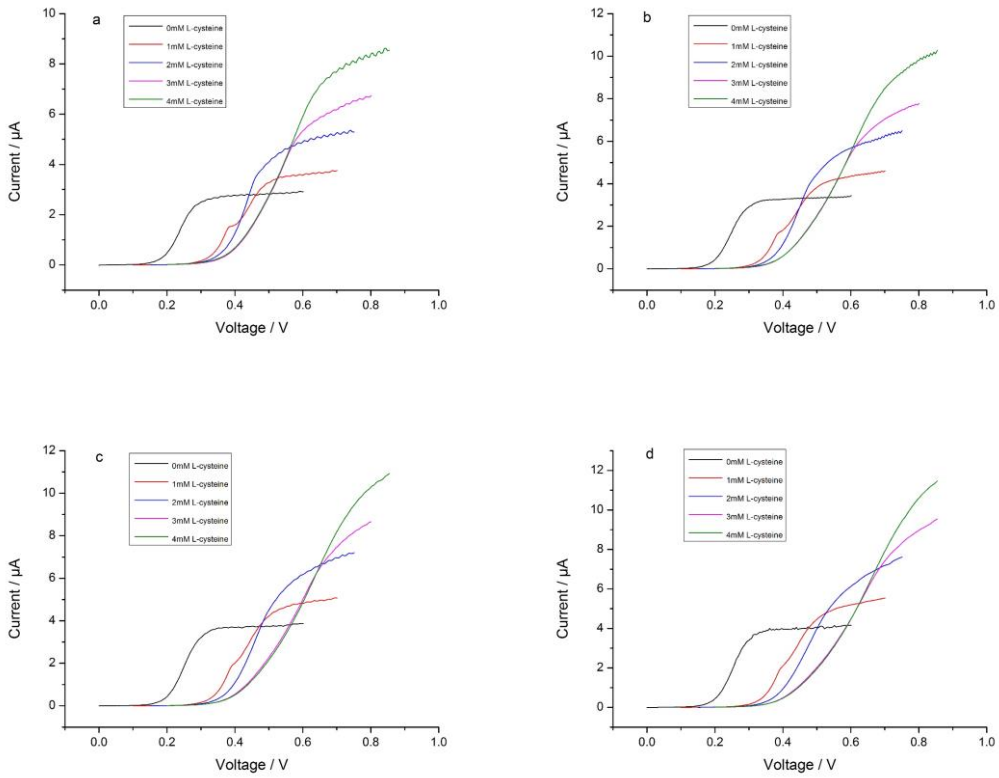

Figure 5.8 LSV of FCA with various concentrations of L-cysteine at scan rate 11.18 mV/s on a 2 mm gold electrode (a) at flow rate 0.05 cm^3/min; (b) at flow rate 0.10 cm^3/min; (c) at flow rate 0.15 cm^3/min;(d) at flow rate 0.20 cm^3/min.

Second, characterization of the EC′ reaction was carried out in a hydrodynamic device with a 500 μm gold working electrode. Figure 5.9 depicts the response of the electrochemically reversible reaction using flow rates 0.1 to 0.6 cm^3/min. The limiting current increased as a function of the cube root of flow rate (R = 0.999). When L-cysteine was introduced into the system with substrate:mediator concentration ratio 1:2, as Figure 5.10 (a) shows, current value increased as v_f was larger. An inflection appeared at low flow rate and decayed as the flow rate rose. The appearance of the inflection was determined by both the diffusion and convection of substrate.

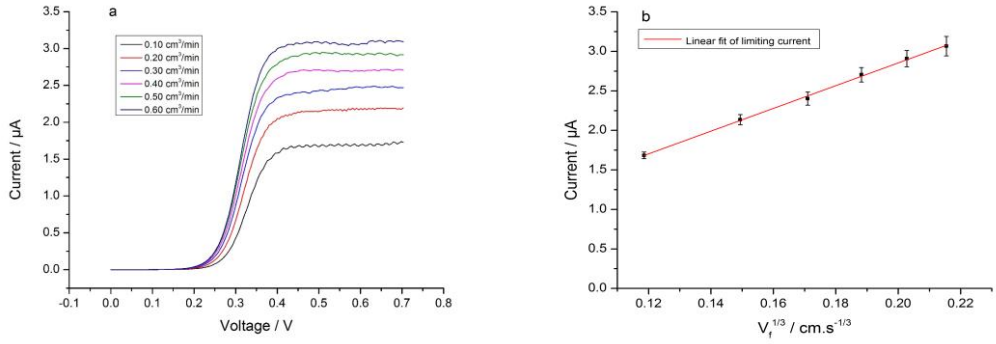

Figure 5.9 (a) LSV of FCA with various flow rates (from 0.1 to 0.6 cm^3/min) at a 500 μm gold electrode, with scan rate 14.9 mV/s; (b) linear fit of limiting current against cube root of flow rate.

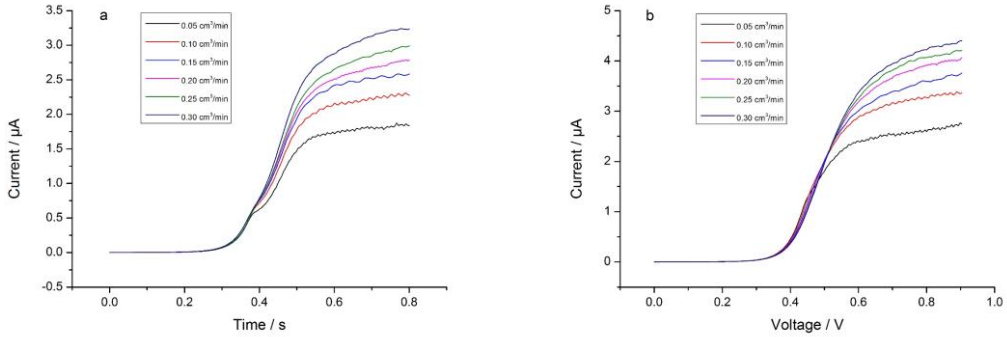

Figure 5.10 LSV of FCA under presence of L-cysteine with various flow rates (from 0.05 to 0.3 cm^3/min) at scan rate 14.9 mV/s on a 500 μm gold electrode with (a) 1 mM L-cysteine; (b) 2 mM L-cysteine.

Comparing with the pre-wave obtained with a 2 mm electrode, the current pre-waves were positioned at a more positive potential and were less apparent. The difference was caused by larger diffusional fluxes of the substrate. For the electrolyte with substrate:mediator concentration ratio of 1:1, in Figure 5.10 (b), as the flow rate rose, higher mass transport caused larger limiting current and disappearance of the pre-wave.

Electrochemical responses with substrate-mediator concentration ratios 0.5:2, 1:2, 1.5:2, and 2:2 were then investigated at fixed flow rates (0.10, 0.20, 0.30 cm^3/min). When the flow rate was 0.10 cm^3/min, as Figure 5.11 (a) shows, the introduction of substrate led to the shift towards oxidative potential and the pre-wave gradually disappeared. For the flow rate of 0.20 and 0.30 cm^3/min, similar phenomena were observed in Figure 5.11 (b) and (c).

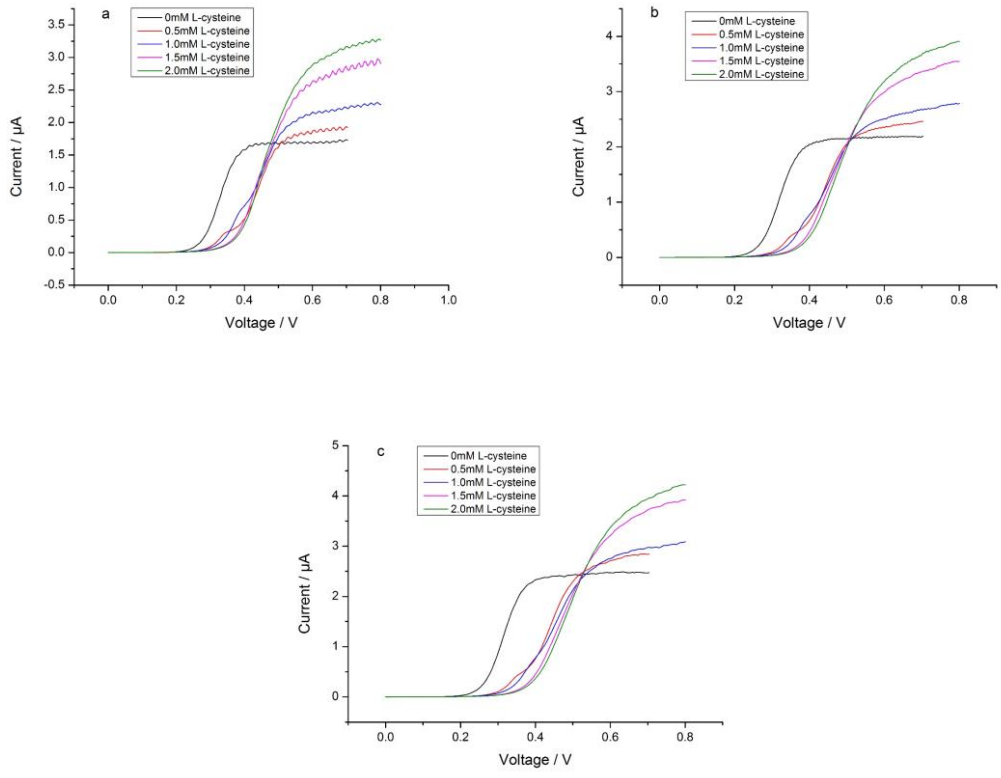

Figure 5.11 LSV of FCA with various concentrations of L-cysteine at scan rate 14.9 mV/s on a 500 μm gold electrode (a) at flow rate 0.10 cm^3/min; (b) at flow rate 0.20 cm^3/min; (c) at flow rate 0.30 cm^3/min.

Third, to understand the EC′ reaction on a microscale channel electrode, another hydrodynamic device, using 100 μm gold as working electrode, was fabricated. Figure 5.12 shows the current response of the Fc/Fc^+ couple in this device. A sigmoidal shape and limiting plateau were observed under flow rates ranging from 0.05 to 0.6 cm^3/min. The Levich relation was confirmed in Figure 5.12 (b).

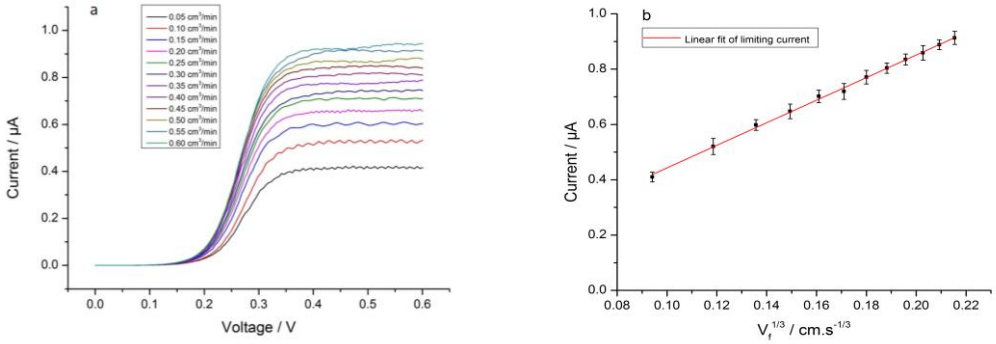

Figure 5.12 (a) LSV of FCA with various flow rates (from 0.05 to 0.6 cm^3/min) at a 100 μm gold electrode with scan rate 14.9 mV/s; (b) linear fit of limiting current.

However, when the catalytic reaction was introduced into the system, in Figure 5.13, the pre-wave was not observable for the 100 μm electrode. The difference could be explained as follows, edge effects enhanced the rate of mass transport towards the electrode surface and such higher efficiency obtained with the smaller electrode led to a stronger catalytic effect and suppressed the presence of the pre-wave.

Figure 5.14 compares the electrochemical behaviours of different L-cysteine concentrations (0, 0.5, 1.0, 1.5, 2.0 mM) at the above flow rates (i.e. 0.1, 0.2, 0.3 cm^3/min). A weak inflection was observed when 0.5 mM L-cysteine was added to FCA/FCA^+ solution, as shown in Figure 5.14 (a). The current became larger as the substrate:mediator ratio increased. Moreover, the voltammogram tended to shift to a more positive potential and the limiting value also increased as expected. Finally, when the flow rates were between 0.20 cm^3/min and 0.30 cm^3/min, similar phenomena were

observed and the inflection became less obvious with an L-cysteine concentration below 0.5 mM (Figure 5.14 (b) and (c)).

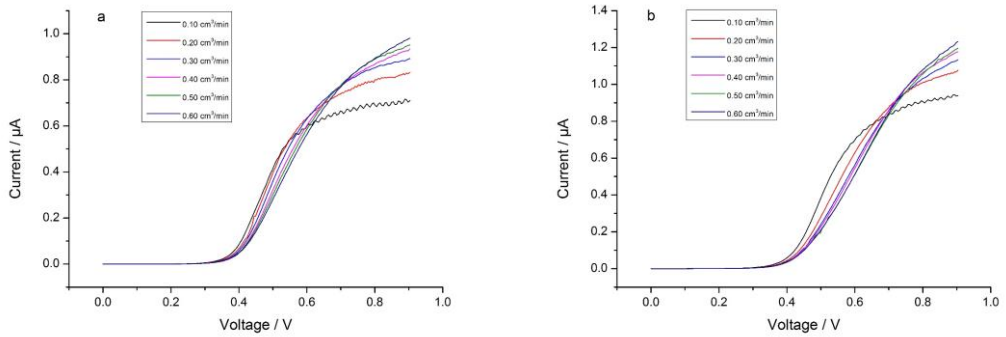

Figure 5.13 LSV of FCA in the presence of L-cysteine with various flow rates (from 0.10 to 0.60 cm^3/min) at scan rate 14.9 mV/s for a 100 µm gold electrode device with (a) 1 mM L-cysteine; (b) 2 mM L-cysteine.

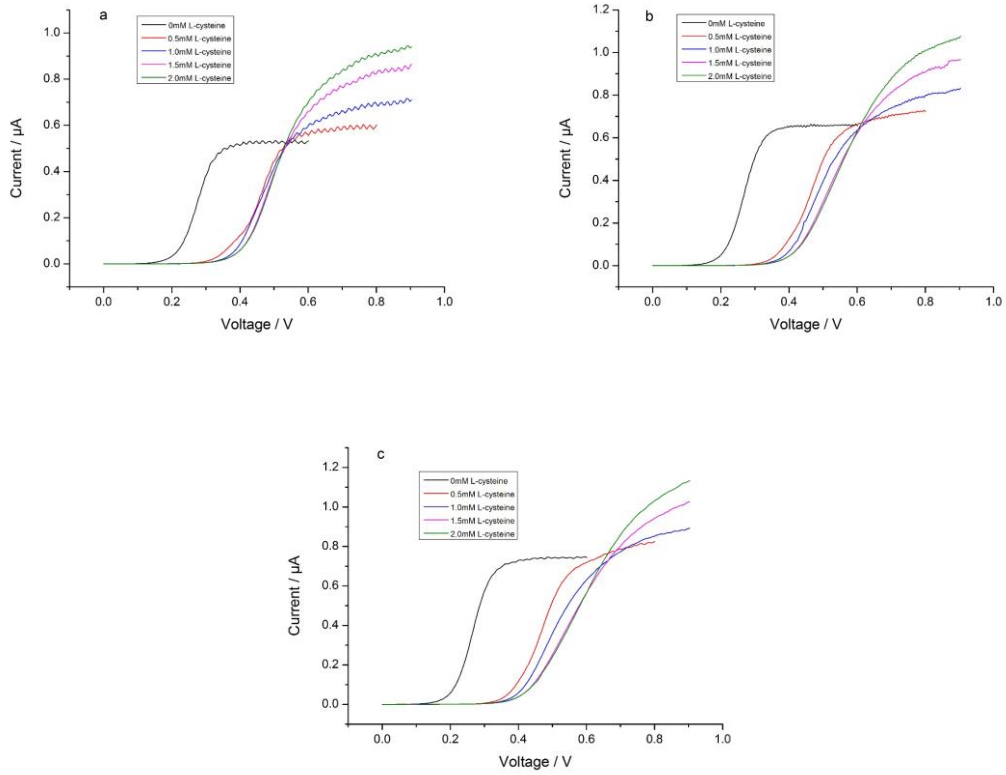

Figure 5.14 LSV of FCA with various concentrations of L-cysteine at scan rate 14.9 mV/s on a 100 µm gold electrode (a) at flow rate 0.10 cm^3/min; (b) at flow rate 0.20 cm^3/min; (c) at flow rate 0.30 cm^3/min.

5.4.3 Electrocatalytic detection under fluidic conditions by FTACV

Finally, FTACV measurements were carried out in the microfluidic system. The operating parameters for the data presented in the thesis were flow rate: 0.05–0.6 cm^3/min, frequency: 10 Hz, amplitude: 50 mV, and scan rate: 41 mV/s. Figure 5.15 shows the signal responses of the first four harmonic components at a 500 μm gold electrode. As the flow rate increased, the peak current became larger due to the decrease in the thickness of the diffusion layer. For the fundamental harmonic component, the shape of the peak was not varied by the status of the stream in the device.

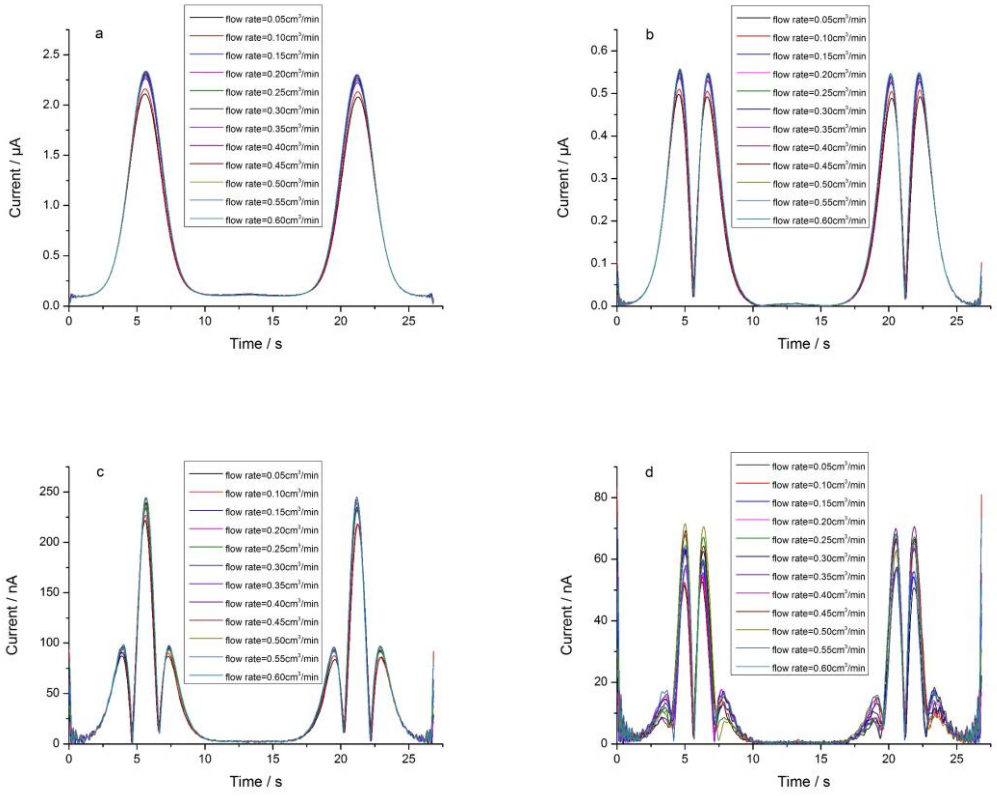

Figure 5.15 The FTACV of 1 mM ferrocene methanol with various flow rates (from 0.05 to 0.6 cm^3/min) at a 500 μm gold electrode, with scan rate 41 mV/s, frequency 10 Hz, amplitude 50 mV: (a) fundamental harmonic; (b) second harmonic; (c) third harmonic; (d) fourth harmonic.

In Figure 5.15 (a), a symmetrical peak was obtained for both forward and backward scans. In addition, the peak height of the backward scan was consistent with that of the forward scan due to the reversibility of the electrolyte. For the second harmonic component, as Figure 5.15 (b) shows, a pair of symmetrical bell-shaped peaks was obtained. The peak did not shift with the flow rate, even though the value of current increased according to the rise of flow rate. Similar phenomena were observed in the third and fourth harmonic components in Figure 5.15 (c) and (d).

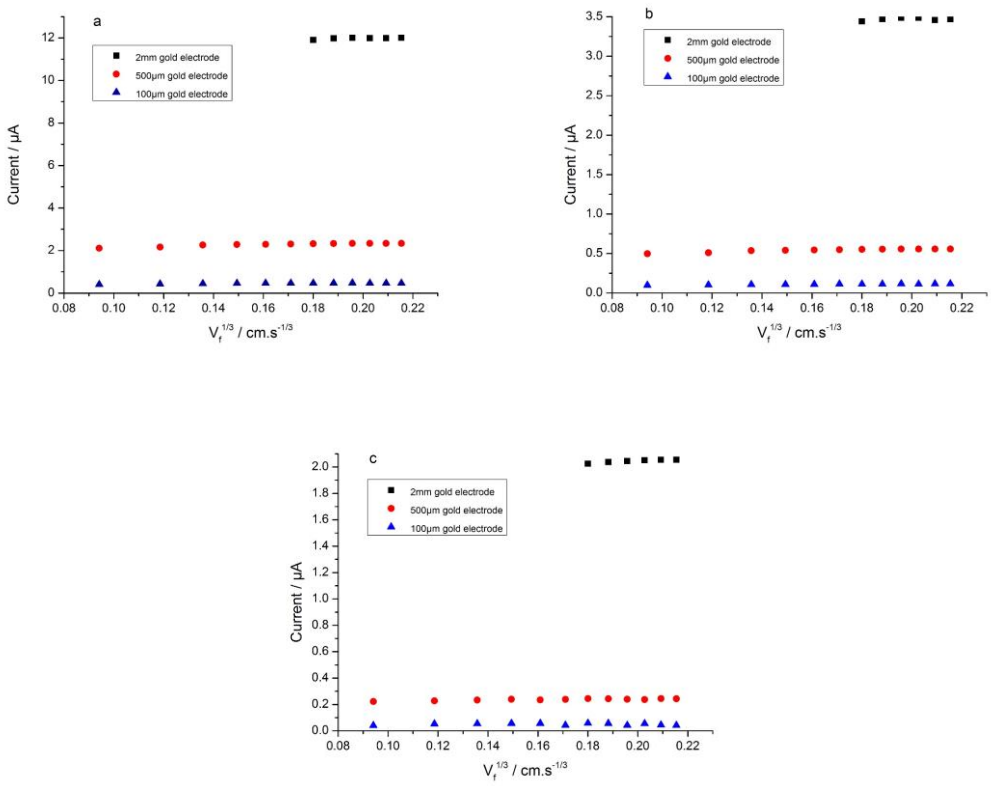

Figure 5.16 The current peak of FTACV with 1 mM ferrocene methanol with various flow rates (from 0.05 to 0.6 cm^3/min) at (a) fundamental harmonic; (b) second harmonic; (c) third harmonic.

Figure 5.16 shows the relationship of the peak value for the first three harmonic components vs the cube root of flow rate. To reach steady state, the flow rates 0.35–0.6 cm^3/min for the 2 mm electrode device (black) were chosen. The flow rates for the 500 μm (red) and 100 μm (blue) electrode devices were 0.05–0.6 cm^3/min. When the flow

in the channel was fast enough and reached the convective controlled condition, the current of the harmonic components behaved in a Levich-like manner, as expected.

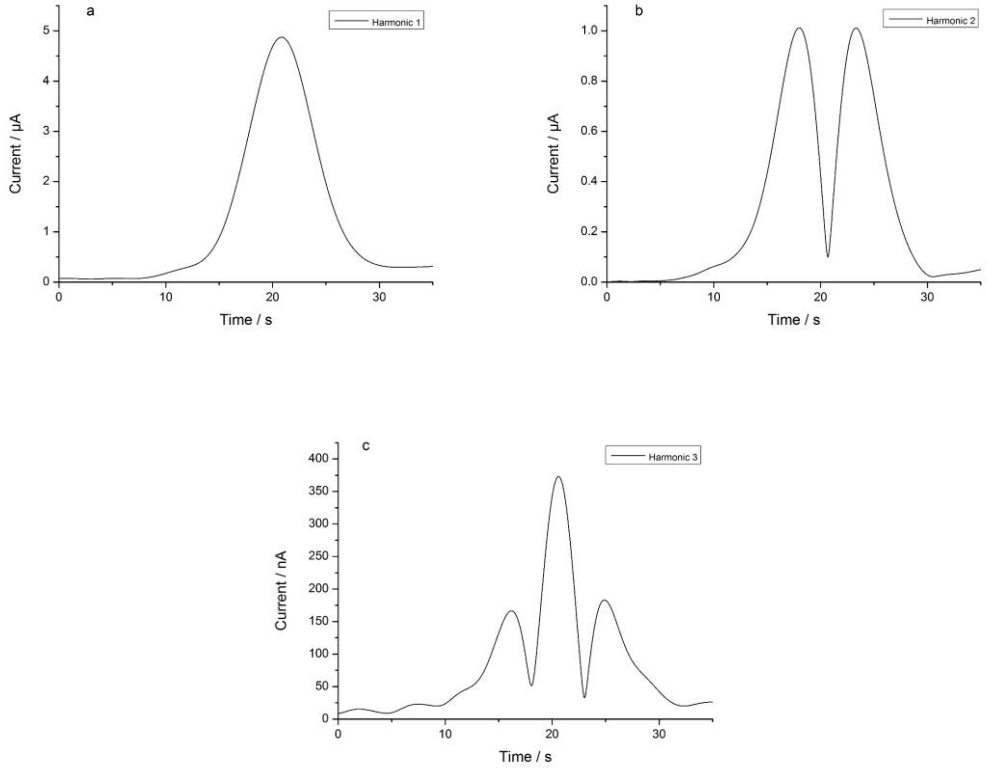

Figure 5.17 The FTACV of cysteine-FCA ratio 1:2 at scan rate 14.9 mV/s, frequency 1 Hz, amplitude 50 mV with flow rate 0.1 cm^3/min on a 2 mm gold electrode (a) first harmonic; (b) second harmonic; (c) third harmonic.

Further, FTACV measurements were carried out to investigate the influence of sulphide under hydrodynamic conditions. Figures 5.17, 5.18, and 5.19 compare the electrochemical responses of devices using different electrode sizes (2 mm, 500 μm, and 100 μm) with added sulphide. The parameters used were flow rate: 0.1 cm^3/min, frequency: 1 Hz, amplitude: 50 mV, scan rate: 14.9 mV/s. The fundamental harmonic component in Figures 5.17 (a), 5.18 (a), and 5.19 (a) showed the characteristic electrochemical response, which varied according to the geometry of the electrodes. In the case of the 2 mm wide electrode, a clear inflection was observed (Figure 5.17 (a)). As the electrode size was reduced, Figure 5.18 (a), the effect of catalytic reaction

became stronger by using the device with a 500 μm electrode and the split-wave characteristics began to merge with the main voltammetric signal. For the 100 μm device, this effect was totally merged with the current of the redox reaction in Figure 5.19 (a).

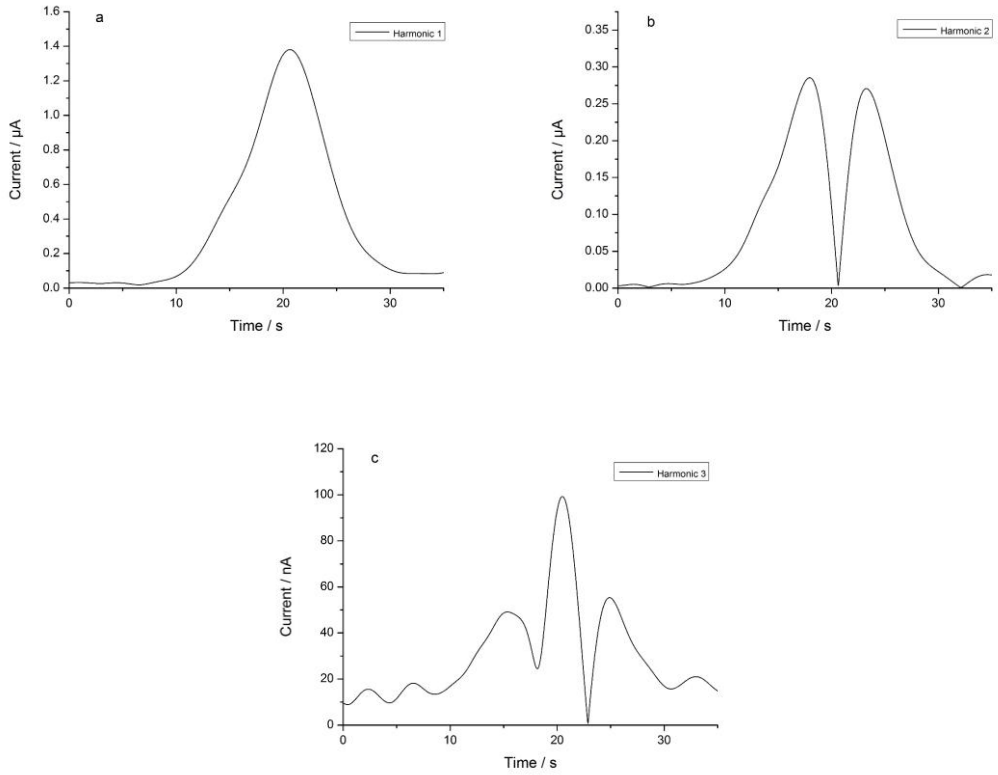

Figure 5.18 The FTACV of cysteine-FCA ratio 1:2 at scan rate 14.9 mV/s, frequency 1 Hz, amplitude 50 mV with flow rate 0.1 cm^3/min on a 500 μm gold electrode (a) first harmonic; (b) second harmonic; (c) third harmonic.

Although more complex, the split-wave feature was observed clearly in the hydrodynamic measurements and the response could be varied as a function of the volumetric flow rate. The second harmonic component was more sensitive to the faradaic signal and the effect of the catalytic reaction was mainly on the first peak. In Figure 5.18 (b), a small inflection appeared ahead of the symmetrical double peaks. Because of the current contribution of the C′ step, the peak area of the first was larger than the second. The area ratio of the first peak vs the second peak in the second harmonic component increased as the electrode size reduced. This result agreed with

the assumption that the catalytic effect was stronger on the smaller electrode. As such, the smaller-sized electrode may be more sensitive for sulphide detection.

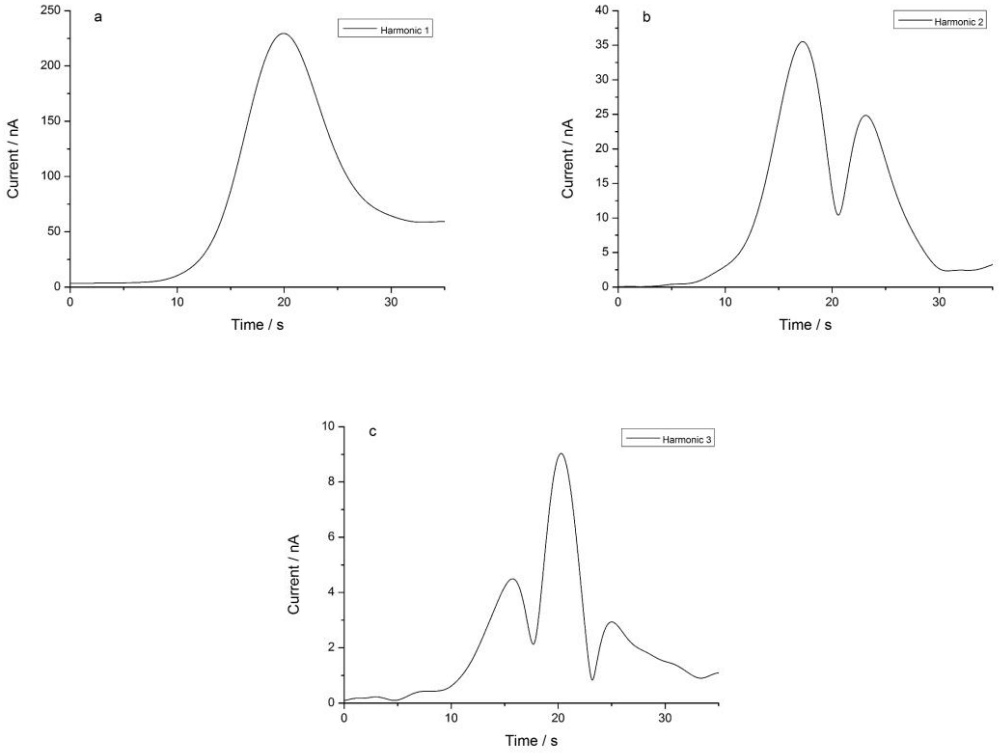

Figure 5.19 The FTACV of cysteine-FCA ratio 1:2 at scan rate 14.9 mV/s, frequency 1 Hz, amplitude 50 mV with flow rate 0.1 cm^3/min on a 100 μm gold electrode (a) first harmonic; (b) second harmonic; (c) third harmonic.

5.4.4 Simulated result of the self-catalytic reaction

To understand the reaction mechanism of electrocatalytic reaction under hydrodynamic conditions, a numerical simulation was employed to support the experimental results. Hydrodynamic simulation of the FTACV was carried out in COMSOL. Modelling the microfluidic environment has the significance and advantage to foresee the electrochemical behaviour of a complicated system that is not easily obtained by experiments and could assist in explaining the assumption obtained in the experimental parts. The parameters were as follows, diffusion coefficient for redox species: $7.6 \times 10^{-}$

^{10} m^2/s; diffusion coefficient of substrate: 6×10^{-10} m^2/s; kinetics of reversible reaction: 0.001 m/s; kinetics of catalytic reaction: 10^6 M/s; double layer capacitance: 50 μF/cm^2; scan rate: 10 mV/s; amplitude of sinusoidal signal superimposed: 50 mV; frequency: 1 Hz; electrode width: 100 μm; channel width: 670 μm; channel height: 1000 μm.

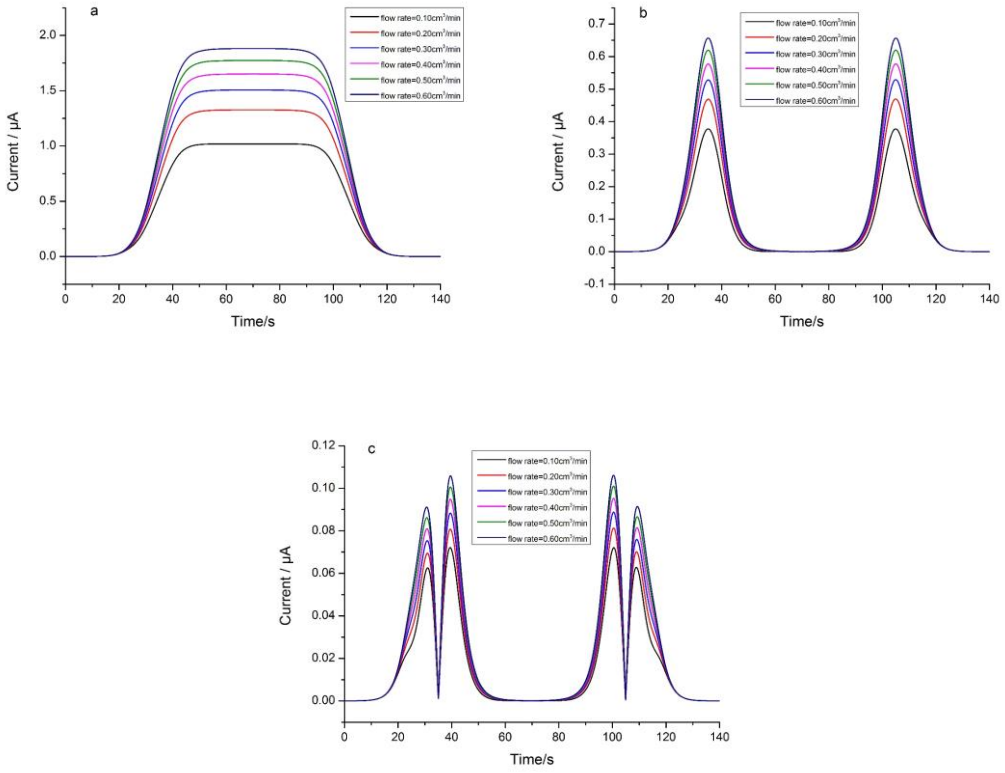

Figure 5.20 Simulated result of the electrocatalytic reaction with substrate concentration 0.3 mM by FTACV, flow rates range from 0.1 to 0.6 cm^3/min.

The current behaviour with the appearance of a tiny amount of substrate (0.3 mM) in 2 mM catalytic species at varying flow rates was simulated. Figure 5.20 (a) was the dc component decomposed from the FTACV. As the flow rate increased, the thinner diffusion layer led to a current rise. For the fundamental component, a weak inflection presented at the shoulder of the oxidative reaction at low flow rates. The inflection decayed as the stream moved faster. The second harmonic component (Figure 5.20 (b)) showed a clear pre-wave feature, which became obvious due to the high sensitivity of

the second harmonic to the faradaic component. The appearance of the pre-wave shared the current of the first peak that led to the decrease in the peak height. Further experiments are required to explore fully the predictions of the numerical models; however, it is clear that the overall trends observed are very much in line with the quantitative predictions.

5.5 Conclusion

Microengineered devices have been fabricated and employed to investigate the detection of sulphide in aqueous solution under microfluidic conditions. Electrodes, from macroscale to microscale, are used as working electrodes in dc and ac voltammetry. The pre-wave phenomena were observed for the first time under fluidic conditions. For the dc voltammetry, as the electrode size becomes smaller, the pre-wave observed under microfluidic conditions begins to merge with the main catalytic wave. This effect is also observed as the flow rate is increased in the cell.

For the FTACV, a weak inflection, related to the reaction with sulphide, is observed in the first harmonic components. For the second and higher harmonics, the effect of the chemical reaction brings enormous change at the first half wave due to the higher sensitivity of faradaic components and the property of avoiding capacitive. Electrodes with smaller size have been proved to be more sensitive in detecting sulphide. The results achieved in this chapter prove the possibility of FTACV to detect sulphide under a fluidic condition with sensitivity down to 0.5 mM. In addition, the results can be a guide for the further electrochemical investigation of the EC′ mechanism in hydrodynamic channel devices.

Reference

1. Alting, L., et al., *Micro Engineering.* CIRP Annals - Manufacturing Technology, 2003. **52**(2): p. 635-657.
2. Holmes, A.S., *Microengineering - The Next Revolution*. 2000.
3. Dittrich, P.S. and A. Manz, *Lab-on-a-chip: microfluidics in drug discovery.* Nat Rev Drug Discov, 2006. **5**(3): p. 210-218.
4. Janasek, D., J. Franzke, and A. Manz, *Scaling and the design of miniaturized chemical-analysis systems.* Nature, 2006. **442**(7101): p. 374-380.
5. Mason, B.P., et al., *Greener Approaches to Organic Synthesis Using Microreactor Technology.* Chemical Reviews, 2007. **107**(6): p. 2300-2318.
6. Zhang, Y., et al. *A high-sensitive ultra-thin MEMS capacitive pressure sensor*. in *2011 16th International Solid-State Sensors, Actuators and Microsystems Conference*. 2011.
7. Radke, S.M. and E.C. Alocilja, *A high density microelectrode array biosensor for detection of E. coli O157:H7.* Biosensors and Bioelectronics, 2005. **20**(8): p. 1662-1667.
8. Rossier, J.S., et al., *Electrochemical Detection in Polymer Microchannels.* Analytical Chemistry, 1999. **71**(19): p. 4294-4299.
9. Cecilia, D.R., et al., *Efficiency of energy conversion for devices containing a piezoelectric component.* Journal of Micromechanics and Microengineering, 2004. **14**(5): p. 717.
10. Shu, Y.C. and I.C. Lien, *Efficiency of energy conversion for a piezoelectric power harvesting system.* Journal of Micromechanics and Microengineering, 2006. **16**(11): p. 2429.
11. Oprea, A., et al., *Environmental monitoring with a multisensor platform on polyimide foil.* Sensors and Actuators B: Chemical, 2012. **171–172**: p. 190-197.
12. Namieśnik, J., *Trends in Environmental Analytics and Monitoring.* Critical Reviews in Analytical Chemistry, 2000. **30**(2-3): p. 221-269.
13. Abeysinghe, D.C., et al., *A novel MEMS pressure sensor fabricated on an optical fiber.* IEEE Photonics Technology Letters, 2001. **13**(9): p. 993-995.
14. Palasagaram, J.N. and R. Ramadoss, *MEMS-Capacitive Pressure Sensor Fabricated Using Printed-Circuit-Processing Techniques.* IEEE Sensors Journal, 2006. **6**(6): p. 1374-1375.
15. Li, M., M. Wang, and H. Li, *Optical MEMS pressure sensor based on Fabry-Perot interferometry.* Optics Express, 2006. **14**(4): p. 1497-1504.
16. Srinivasan, V., V.K. Pamula, and R.B. Fair, *An integrated digital microfluidic lab-on-a-chip for clinical diagnostics on human physiological fluids.* Lab on a Chip, 2004. **4**(4): p. 310-315.
17. Ali, S.M.U. and K.A. Tasuif Aijazi, Omer Nur and Magnus Willander, *Wireless Remote Monitoring of Glucose Using a Functionalized ZnO Nanowire Arrays Based Sensor.* Sensors, 2011. **11**(9): p. 8485-8496.

18. Ahmadi, M.M. and G.A. Jullien, *A Wireless-Implantable Microsystem for Continuous Blood Glucose Monitoring.* IEEE Transactions on Biomedical Circuits and Systems, 2009. **3**(3): p. 169-180.
19. Gardeniers, J.G.E. and A. van den Berg, *Lab-on-a-chip systems for biomedical and environmental monitoring.* Analytical and Bioanalytical Chemistry, 2004. **378**(7): p. 1700-1703.
20. Abbas, A., et al., *Multifunctional Analytical Platform on a Paper Strip: Separation, Preconcentration, and Subattomolar Detection.* Analytical Chemistry, 2013. **85**(8): p. 3977-3983.
21. A. Baniya, et al., *Lab-on-a-Chip Device for Hydrogen Sulfide Sensing in Biomedical and Environmental Applications Using Electrochemical Approach.* ASME 2015 International Technical Conference and Exhibition on Packaging and Integration of Electronic and Photonic Microsystems collocated with the ASME 2015 13th International Conference on Nanochannels, Microchannels, and Minichannels, 2015. **3**.
22. A. Baniya, S.T., E. Borquist, D. Bailey, D. Wood, J. Glawe, C. Kevil and L. Weiss, *Hydrogen Sulfide Sensing Using Lab-on-a-Chip Device for Biomedical and Environmental Use.* ASME 2015 International Mechanical Engineering Congress and Exposition, 2015. **3**.
23. Ng, J.M.K., et al., *Components for integrated poly(dimethylsiloxane) microfluidic systems.* Electrophoresis, 2002. **23**(20): p. 3461-3473.
24. McDonald, J.C., et al., *Fabrication of microfluidic systems in poly(dimethylsiloxane).* ELECTROPHORESIS, 2000. **21**(1): p. 27-40.
25. Duffy, D.C., et al., *Rapid Prototyping of Microfluidic Systems in Poly(dimethylsiloxane).* Analytical Chemistry, 1998. **70**(23): p. 4974-4984.
26. Trojanowicz, M., *Recent developments in electrochemical flow detections—A review: Part I. Flow analysis and capillary electrophoresis.* Analytica Chimica Acta, 2009. **653**(1): p. 36-58.
27. Matthews, S.M., et al., *Attributes of Direct Current Aperiodic and Alternating Current Harmonic Components Derived From Large Amplitude Fourier Transformed Voltammetry Under Microfluidic Control in a Channel Electrode.* Analytical Chemistry, 2012. **84**(15): p. 6686-6692.
28. Sansuk, S., et al., *Ultrasensitive Detection of Dopamine Using a Carbon Nanotube Network Microfluidic Flow Electrode.* Analytical Chemistry, 2013. **85**(1): p. 163-169.
29. Illa, X., et al., *A cyclo olefin polymer microfluidic chip with integrated gold microelectrodes for aqueous and non-aqueous electrochemistry.* Lab on a Chip, 2010. **10**(10): p. 1254-1261.
30. Chen, I.J. and I.M. White, *High-sensitivity electrochemical enzyme-linked assay on a microfluidic interdigitated microelectrode.* Biosensors and Bioelectronics, 2011. **26**(11): p. 4375-4381.

Chapter 6 Conclusion and future plan

6.1 Conclusion

The work in this thesis has investigated the detection of sulphide in aqueous solution using an electrocatalytic (EC′) reaction. The novel FTACV measurements have been used for the first time to observe split-wave voltammetry characteristics in higher harmonic components.

Chapter 3 detailed the electrochemical performance of the reaction of L-cysteine and catalytic species on macroelectrodes under stagnant conditions using dc cyclic voltammetry and FTACV. Parameters including substrate concentration, CV scan rate, frequency of superimposed AC signal, and size of electrode were explored. In the dc CV, the presence of pre-waves, caused by the catalytic reaction with L-cysteine, was dependent on the scan rate and sulphide concentration. FTACV, as a novel electrochemical method, was used for the first time to characterise the pre-wave phenomena. Linear correlation of peak height against L-cysteine concentration proves the potential of FTACV in detecting sulphide. Also, the enhancement of signal-to-noise ratio at higher harmonic components allows FTACV to be more sensitive to detect the sulphide. Numerical simulations supported the discussion of the experimental observations.

Chapter 4 reports the reaction of sulphide and catalytic species characteristics at microscale electrodes. Electrochemical performance varied when using glassy fibre and gold as working electrodes, split waves were obtained in both dc and ac approaches. In the dc CV, the enhanced mass transport led to a loss of split peak behaviour and a clear split wave. The FTACV, however, presented advantages in describing the peak

potential $E_{1/2}$ and the split-wave behaviour, which were hard to determine at steady state via the dc voltammetric techniques. In addition, the pre-wave phenomena were first time achieved, and varied dependent on the frequency and sulphide concentrations. FTACV proved itself as a powerful technique in the potential determination and with high sensitivity to the chemical processes, which can be potentially used in chemical detection.

Chapter 5 described the design, development and application of a microfluidic electrochemical sensor for sulphide detection. The split-wave phenomena were observed for the first time on hydrodynamic electrodes both for dc and FTACV. The potential and current height were found to vary as a function of solution velocity and electrode dimension. The results were useful to show how the EC′ mechanism behaves according to the variation of flow rate and sulphide concentration. In addition, the determination of the pre-wave in dc voltammetry and the current behaviour in the harmonic components of FTACV proved the possibility of using electrochemical sensors for sulphide detection under fluidic conditions, which may reduce the complication of current sulphide detection in oil field wellbore applications. Numerical simulations supported the experimental interpretation of the acquired data.

6.2 Future plan

According to the discussion and conclusions of Chapters 3 and 4, the split-wave behaviour of the EC′ mechanism is achieved for the first time by large-amplitude ac voltammetry both in experiments and numerical simulations. To take advantage of ac voltammetry's strength in quantitative analysis of electrochemical mechanisms, a sophisticated numerical analysis model should be developed to fit the experimental results. This numerical model should be able to (a) separate the faradaic and non-

faradaic components; (b) be ready for the capacitance determination on dc and first harmonic; (c) be sensitive to the uncompensated resistance in the second harmonic.

A further research interest will be focused on the split-wave presence in the hydrodynamic condition. This thesis discovers split-wave behaviour in the well-defined three-gold-electrode devices, other electrodes should be developed to encourage an enhanced and stronger signal response. To avoid the instability and potential shift induced by the pseudo-reference gold electrode, standard reference electrodes are highly recommended. In addition, carbon electrodes with theoretically higher surface area and well-defined electrochemical performance will be applied in the next step of the research in dc analysis. The design of the three-electrode system with a standard reference electrode, glassy carbon working electrode, and gold or platinum screen-printed counter electrode is shown in Figure 6.1.

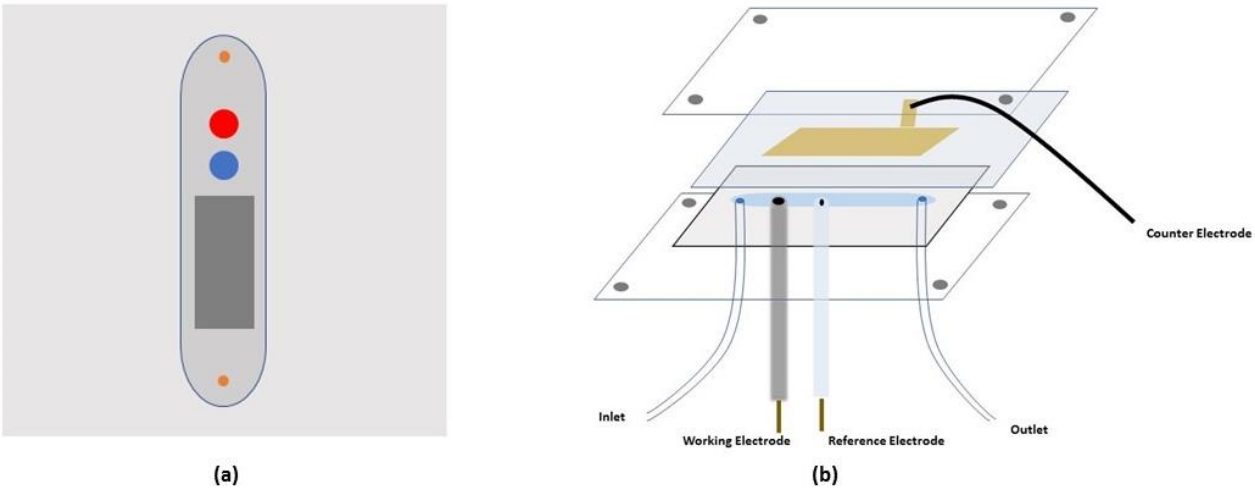

Figure 6.1 Schematic of the hydrodynamic three-electrode system, (a) top view of the channel with red as the working electrode, blue as reference electrode, grey as counter electrode; (b) side view of the fabricated device.

For large-amplitude ac voltammetry, it should be noted that the complexity of the EC′ electrochemical response to the ac input signal and the complicated flux behaviour

require a better understanding in both theoretical and experimental considerations. The study of the EC′ mechanism in the hydrodynamic electrode will be continued with different parameters: (1) flow rate, (2) geometry of the hydrodynamic devices (working electrode material, channel height), (3) substrate concentration. In Figure 6.2, the theoretical simulated results according to the changing substrate concentration and the

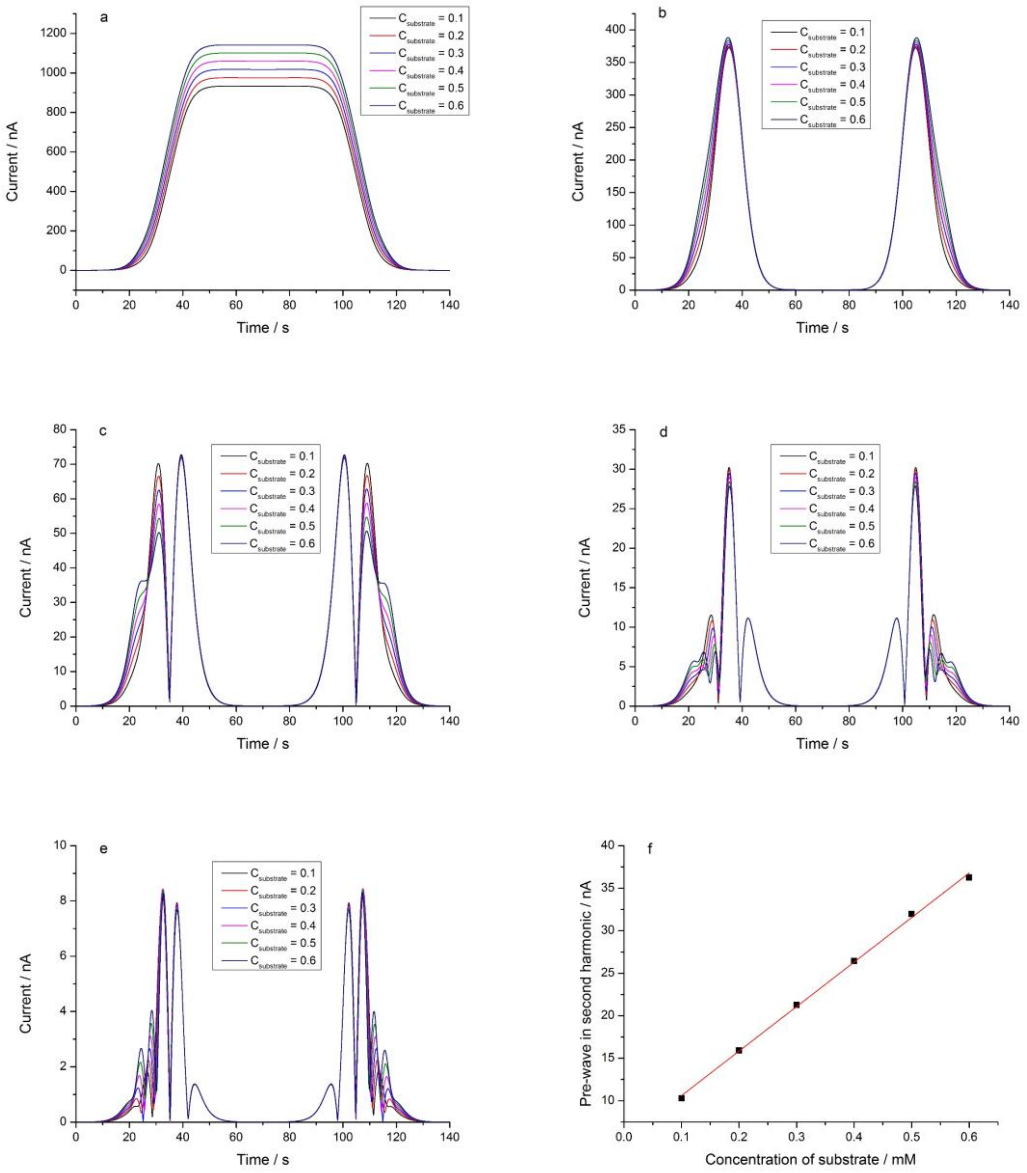

Figure 6.2 Simulated results of DC, first, second, third, and fourth harmonics with different concentrations of substrate (0.1–0.6 mM). The linear fit of the pre-wave in the second harmonic against substrate concentration.

flow rate of 0.1 cm^3/min are chosen that are high enough to achieve steady-state current but slow enough not to lose the current behaviour of the pre-wave. The current plateau rises as substrate concentration increases but the pre-wave cannot be observed in the dc components. For the fundamental component, weak pre-shoulders induce the waves to be fattened as the substrate concentration increases. For the second harmonic in Figure 6.2 (c), clear pre-peaks form before the first main peaks and the peaks become more independent at higher substrate concentration. For the simulated result, the second peak is ideally not varied by the appearance of the substrate. Without consideration of adsorption of substrate on the electrode, the height of the pre-wave in the second harmonic has a linear correlation with the concentration of substrate, as Figure 6.2 (f) depicts (R = 0.999). This is an interesting phenomenon that in principle can be applied to detect the amount of sulphide in the solution.

Appendix

In the appendix, the protocols of the microfabrication (including positive and negative fabrication) are detailed. Theories of the numerical models used to support the experimental measurements are discussed.

A.1 Protocol of microfabrication

A.1.1 Coating of photoresists

Thickness (2.5μm)		
Spin speed (rpm)	Acceleration	Duration (s)
4000	0	60

Table A.1 Protocol of positive photoresist coating

Spin speed 1 (rpm)	Acceleration	Duration (s)	Spin speed 2 (rpm)	Acceleration	Duration (s)
100 μm					
500	9	10	3000	4	30
140 μm					
500	9	10	2000	4	30
200 μm					
500	9	10	1000	4	30

Table A.2 Protocol of negative photoresist coating.

A.1.2 Pre-baking

Soft baking temperature (℃)	Time (min)
115	1

Table A.3 Pre-baking of positive photoresist.

Soft baking 1 temperature (℃)	Time (min)	Soft baking 2 temperature (℃)	Time (min)
100 μm			
65	5	95	20
140 μm			
65	5	95	35
200 μm			
65	12	95	60

Table A.4 Pre-baking of negative photoresist.

A.1.3 Post-baking

Post baking 1 temperature (℃)	Time (min)	Post baking 2 temperature (℃)	Time (min)
100 μm			
65	1	95	10
140 μm			
65	1	95	15
200 μm			
65	1	95	15

Table A.5 Post-baking of negative photoresist.

A.1.4 Development

Film thickness (μm)	Development time (min)
100	5-6
140	8-9
200	20-25

Table A.6 Development time of negative photoresist.

A.2 Theory of numerical simulations

Numerical simulation has been widely employed to detail electrochemical processes as it can separate the complications in reaction into a series of solved procedures [1]. To give a theoretical support for the experimental results, the numerical approach has to be fixed specifically, based on the original model developed by Viet Nyuyen, to characterize heterogeneous charge transfer on an electrode surface coupled with a homogeneous chemical reaction. The modelling of the EC′ mechanism was developed for three different cases: (1) a large planar electrode in stagnant solution, (2) a microelectrode in stagnant solution and (3) a microelectrode located in a microfluidic channel. In the latter case, it was assumed that the convection rate was sufficient to remove any axial diffusion effects from the current response, which is a good approximation for the flow rate and cell conditions used experimentally. The linear fit of the current peak vs substrate concentration provides theoretical support for the possibility of FTACV in sulphide detection.

A.2.1 Chemical kinetics of electrocatalytic mechanism

The electrocatalytic process detailed in section 3.4 was modeled using the COMSOL package. For the case of a large planar electrode in a solution of high electrolyte ionic strength the following governing equations were solved:

$$\frac{\partial c_R}{\partial t} = D_R \frac{\partial^2 c_R}{\partial x^2} + k_1 c_O c_Z - k_{-1} c_R c_P \quad \text{(A.1)}$$

$$\frac{\partial c_O}{\partial t} = D_O \frac{\partial^2 c_O}{\partial x^2} - k_1 c_O c_Z + k_{-1} c_R c_P \quad \text{(A.2)}$$

$$\frac{\partial c_Z}{\partial t} = D_Z \frac{\partial^2 c_Z}{\partial x^2} - k_1 c_O c_Z + k_{-1} c_R c_P \quad \text{(A.3)}$$

$$\frac{\partial c_P}{\partial t} = D_P \frac{\partial^2 c_P}{\partial x^2} + k_1 c_O c_Z - k_{-1} c_R c_P \quad \text{(A.4)}$$

where k_1 and k_{-1} are defined as second-order rate constant of catalytic reaction with units $M^{-1}s^{-1}$.

At the start of reaction, the system was assumed to be composed only by R and Z that the initial concentration are C_R^* and C_z^*, the relationship can be explained:

$$\left.\begin{matrix} t = 0, x \geq 0 \\ t > 0, x \to \infty \end{matrix}\right\} C_R = C_R^*, C_O = 0, C_Z = C_Z^*, C_P = 0 \quad \text{(A.5)}$$

The following boundary conditions were employed for solution of the governing equations:

$$\begin{cases} D_R\left(\frac{\partial C_R}{\partial x}\right)_{X=0} = k_{red} C_R(0,t) - k_{ox} C_O(0,t) \\ D_O\left(\frac{\partial C_O}{\partial x}\right)_{X=0} = -D_R\left(\frac{\partial C_R}{\partial x}\right)_{X=0} \\ \left(\frac{\partial C_Z}{\partial x}\right)_{X=0} = 0 \\ \left(\frac{\partial C_Y}{\partial x}\right)_{X=0} = 0 \end{cases} \quad \text{(A. 6)}$$

As parameters, such as concentration of bulk solution, electrode size and diffusion coefficient, affect the solution obtained from above equations. Dimensionless forms of variables were employed to demonstrate parameters as multiples with same dimensionality. The dimensionless form of equation is explained as follows:

$$\mathrm{X} = \frac{X}{\epsilon} \tag{A.7}$$

$$\mathrm{T} = \frac{D_R t}{\epsilon^2} \tag{A.8}$$

$$\theta = \frac{F(E-E_f^0)}{RT} \tag{A.9}$$

$$K_{2nd} = k\frac{C_R^* \epsilon^2}{D_R} \tag{A.10}$$

$$d_j = \frac{D_j}{D_R} \tag{A.11}$$

$$C_j = \frac{C_j}{C_R^*} \tag{A.12}$$

$$\frac{\partial C_R}{\partial \mathrm{T}} = d_R \frac{\partial^2 C_R}{\partial X^2} + K_{2nd} C_O C_Z \tag{A.13}$$

$$\frac{\partial C_O}{\partial \mathrm{T}} = d_O \frac{\partial^2 C_O}{\partial X^2} - K_{2nd} C_O C_Z \tag{A.14}$$

$$\frac{\partial C_Z}{\partial \mathrm{T}} = d_Z \frac{\partial^2 C_Z}{\partial X^2} - K_{2nd} C_O C_Z \tag{A.15}$$

$$\frac{\partial C_P}{\partial \mathrm{T}} = d_P \frac{\partial^2 C_P}{\partial X^2} + K_{2nd} C_O C_Z \tag{A.16}$$

The K_{2nd} is determined as dimensionless form of the second-order rate constant.

A.2.2 Two-dimensional diffusion on micro electrode

For microelectrode calculations the thickness of diffusion layer is not negligible in comparison with the size of electrode. In this case, modelling of micro-scale electrode is more complex mathematically than that of the macro-scale.

As shown in Figure A.1, the grey part is the electro-active micro-disc and the blanket is inactive supporting surface, where r is the distance from circle centre, z is the perpendicular distance from the electrode surface and φ is the angle. For the micro electrode, the concentration change against time caused by diffusion can be transformed in cylindrical polar version:

$$\frac{\partial C}{\partial t} = D\left(\frac{\partial^2 C}{\partial r^2} + \frac{1}{r}\frac{\partial c}{\partial r} + \frac{1}{r^2}\frac{\partial^2 c}{\partial \varphi^2} + \frac{\partial^2 c}{\partial z^2}\right) \quad \text{(A.17)}$$

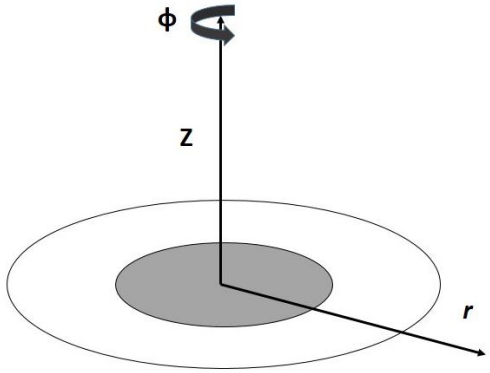

Figure A.1 Schematic of micro-electrode with cylindrical polar coordinate (r, z, φ).

Theoretically, for the symmetrical disc model, the $\frac{\partial c}{\partial \varphi} = \frac{\partial^2 c}{\partial \varphi^2} = 0$. In this case, the equation A.18 is simplified:

$$\frac{\partial C}{\partial t} = D\left(\frac{\partial^2 C}{\partial r^2} + \frac{1}{r}\frac{\partial c}{\partial r} + \frac{\partial^2 c}{\partial z^2}\right) \quad \text{(A.18)}$$

A.2.3 Convection-diffusion on channel electrode

For channel electrodes, assuming measurements are under laminar flow condition and the cell width which is largely relative to the height the fluid velocity can be predicted:

$$v_x = v_c[1 - \frac{(h-y)^2}{h^2}] \quad \text{(A.19)}$$

where the v_x is the solution velocity on *x* axis, however the v_y and v_z are 0; v_c is the solution velocity at the center of the channel; h is the half height of the channel and y is distance from the electrode on y axis as Figure A.2 shows.

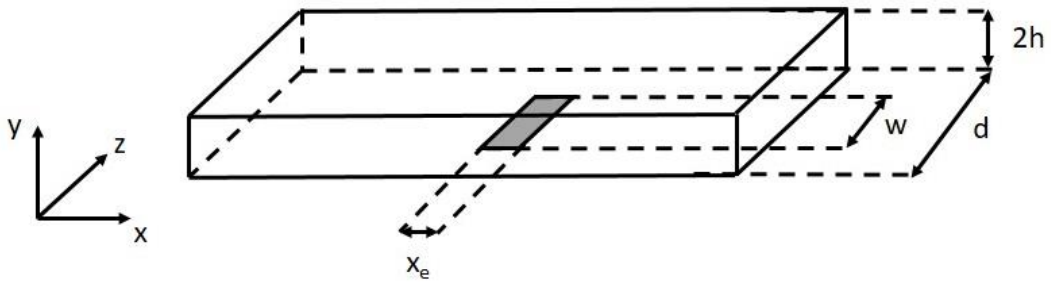

Figure A.2 Schematic figure of channel electrode.

From the approximation, the mass balance equation of materials can be simplified[2]:

$$\frac{\partial c}{\partial t} = D\frac{\partial^2 c}{\partial y^2} - v_x\frac{\partial c}{\partial x} \quad \text{(A.20)}$$

The boundary conditions of reversible reaction can be predicted by

when $\left.\begin{matrix} t = 0, 0 \le x \le x_e, 0 \le y \le 2h \\ t > 0, x < 0 \end{matrix}\right\}$:

$$C_R = C_R^*, C_O = 0 \quad \text{(A.21)}$$

when $t > 0, 0 \le x \le x_e, y = 2h$:

$$(\frac{\partial c_R}{\partial y})_{y=2h} = 0 \quad \text{(A.22)}$$

$$(\frac{\partial c_O}{\partial y})_{y=2h} = 0 \quad \text{(A.23)}$$

when $t > 0, 0 \le x \le x_e, y = 0$:

$$D_R(\frac{\partial c_R}{\partial y})_{y=0} = k_{ox}c_R(0,t) - k_{red}c_O(0,t) \quad \text{(A.24)}$$

$$D_O(\frac{\partial c_O}{\partial y})_{y=0} = -D_R(\frac{\partial c_R}{\partial y})_{y=0} \quad \text{(A.25)}$$

The parameters can be transformed to dimensionless variables:

$$X = \frac{x}{x_e} \quad \text{(A.26)}$$

$$Y = \frac{y}{x_e} \quad \text{(A.27)}$$

$$H = \frac{h}{x_e} \quad \text{(A.28)}$$

$$T = \frac{D_A t}{{x_e}^2} \quad \text{(A.29)}$$

The boundary condition and convection-diffusion equation can be defined in dimensionless terms:

$$\frac{\partial C_R}{\partial T} = \frac{\partial^2 C_R}{\partial Y^2} - \frac{3}{2} Pe[1 - \frac{(H-Y)^2}{H^2}] \frac{\partial C_R}{\partial X} \quad \text{(A.30)}$$

$$\frac{\partial C_O}{\partial T} = d_R \frac{\partial^2 C_O}{\partial Y^2} - \frac{3}{2} Pe[1 - \frac{(H-Y)^2}{H^2}] \frac{\partial C_O}{\partial X} \quad \text{(A.31)}$$

where Pe is Pelect number, defined as Pe= $\frac{v_m x_e}{D_R}$, that represents the convection-diffusion influence of mass transport.

when $\left.\begin{matrix} T = 0, 0 \le X \le 1, 0 \le Y \le \frac{2h}{x_e} \\ T > 0, X < 0 \end{matrix}\right\}$:

$C_R = 1$, $C_O = 0$

when $T > 0, 0 \le X \le 1, Y = \frac{2h}{x_e}$:

$$(\frac{\partial C_R}{\partial Y})_{Y=\frac{2h}{x_e}} = 0 \quad \text{(A.32)}$$

$$(\frac{\partial C_O}{\partial Y})_{Y=\frac{2h}{x_e}} = 0 \quad \text{(A.33)}$$

when $T > 0, 0 \le X \le 1, Y = 0$:

$$(\frac{\partial C_R}{\partial Y})_{Y=0} = K_{ox}C_R(0,t) - K_{red}C_O(0,t) \quad \text{(A.34)}$$

$$d_O(\frac{\partial C_O}{\partial Y})_{Y=0} = -(\frac{\partial C_R}{\partial Y})_{Y=0} \quad \text{(A.35)}$$

Reference

1. Andrieux, C.P., et al., *Homogeneous redox catalysis of electrochemical reactions.* Journal of Electroanalytical Chemistry and Interfacial Electrochemistry, 1980. **113**(1): p. 19-40.
2. Compton, R.G., E. Laborda, and K.R. Ward, *Understanding Voltammetry: simulation of electrode processes*. 2014: Imperial College Press.